HIGHER-ORDER-MODE-DAMPED CAVITIES WITH GROOVED BEAM PIPE STRUCTURES FOR HIGH-LUMINOSITY ELECTRON-POSITRON COLLIDERS

KAGEYAMA Tatsuya

KEK

High Energy Accelerator Research Organization

1-1 Oho, Tsukuba, Ibaraki 305-0801 Japan

July 2002

ABSTRACT

Higher-Order-Mode (HOM) damped accelerating cavity structures play a significant role in high-luminosity electron-positron colliders such as the B-meson factories of KEKB and PEP-II operated with beam currents over 1 A. The coupled-bunch beam instabilities driven by long-lived higher order modes trapped in cavity structures should be suppressed first in order to raise the stored current limit. Various types of HOM-damped cavity structures have been proposed so far to boost the collider performance toward the luminosity frontier. This paper describes a series of studies on a HOM damping scheme with grooved beam pipe structures, from its original concept started with breaking the cylindrical symmetry of "single mode cavity" well known as the oldest HOM damping scheme in 1980's, through computer-aided analysis on its RF properties followed by benchmark experiments, finally to its application to the normal-conducting RF cavity system developed and successfully operated for KEKB. The essence of the grooved beam pipe scheme is to selectively lower the cutoff frequency of the TE11 mode propagating through the circular beam pipe below the lowest TM110-like dipole mode of the accelerating cavity by grooving the inner wall of the beam pipe. Moreover, this scheme could be more suitably applied to super-conducting (SC) cavities because waveguide apertures or ports dedicated to HOM damping are not allowed usually in the SC accelerating cell to avoid quenching under high accelerating gradients.

ACKNOWLEDGEMENTS

This study was initiated when the author stumbled across a grooved structure, and has been accomplished through the KEK B-factory project.

My cordial gratitude must first go to Professor Eiji Ezura, who introduced this thesis to the graduate university for advanced studies, for his continuous encouragement and support.

I would also like to gratefully acknowledge Professor Yoshishige Yamazaki for his continuous encouragement and guidance throughout my years at the accelerator laboratory of KEK.

My special appreciation goes to Professor Koji Takata who once gave me a lecture on Weiland's single-mode cavity. I would not have thought of the grooved beam pipe structure without his clear explanation.

I would like to extend my thanks to the KEKB accelerator staff led by Professor Shin-ichi Kurokawa and Professor Katsunobu Oide for their support to give me an opportunity to apply the idea of the grooved beam pipe to the ARES cavity system, and to all the members of the KEKB RF group for their help indispensable for the success. Especially, I would like to thank my colleague Yasunao Takeuchi for his excellent work in the development of the HOM loads.

Last, I wish to thank my parents for their support, and my wife for her understanding and assistance.

TABLE OF CONTENTS

Chapter 1.
INTRODUCTION

The *B* factories such as KEKB [1,2] in Japan and PEP-II [3] in the US are high-luminosity electron-positron colliders focused on the study of *B* meson decays in quest for the origin of CP violation, a small deviation in symmetry between matter and anti-matter, related to the formation of our universe. The collider performance is usually expressed in luminosity, a measure of the rate of electron-positron collisions. Currently, the *B* factories producing a huge sample of *B* meson pairs in electron-positron collisions are indispensable to the precise study on CP violation.

Figure 1.1 shows a schematic layout of the KEKB accelerator complex, a double-ring electron-positron collider with unequal beam energies, consisting of an 8-GeV electron ring (high-energy ring, HER) and a 3.5-GeV positron ring (low-energy ring, LER). The collision with the unequal beam energies is required to boost the center of mass of the produced *B* meson pair with respect to the laboratory frame, so as to ease the measurement of their decay processes. The design luminosity of KEKB is 10^{34} $cm^{-2}s^{-1}$, more than 10 times of the highest luminosity achieved before the advent of the *B* factories. In circular colliders, high luminosities can be achieved with high-current multi-bunch beams. Needless to say, the beams should be focused at the interaction point as small as possible. The design beam currents of KEKB are 1.1 A for the HER and 2.6 A for the LER. The beam of each ring is distributed among about 5000 bunches with a spacing of 0.6 m (currently 1200 bunches with a spacing of 2.4 m) along the circumference of 3016 m.

Higher-Order-Mode (HOM) damped accelerating cavity structures play a significant role in high-current multi-bunch beam operation to achieve high luminosities. The coupled-bunch beam instabilities driven by long-lived higher order modes trapped in cavity structures should be suppressed first in order to raise the stored current limit. The mechanism of the coupled-bunch instability is schematically shown in Fig. 1.2, that is a kind of Minkowski diagram often used in the theory of special relativity. In the diagram, the horizontal axis represents the one-dimensional space along the

circumference of the accelerator while the vertical axis corresponds to time. The space is finite but cyclic from $-C/2$ to $C/2$, where C is the circumference of the accelerator, and a conventional RF cavity is placed at the origin of the horizontal axis. In Fig. 1.2, a single bunch circulating with the speed of light is represented by solid lines inclined at 45 degrees with respect to the horizontal axis. The bunch induces HOM resonant fields in the RF cavity when passing through it. The bunch traveling on the cavity axis induces monopole modes while the off-axis bunch induces dipole modes in addition to the monopole modes. As shown with a sinusoidal curve along the vertical axis in Fig. 1.2, some of HOMs are trapped in the cavity and survived for long time with the fields strong enough to significantly act back on the bunch at the next turn. The resonant buildup of the interaction between the circulating bunch and the induced HOM fields may result in the beam instability in the worst case. The monopole modes are responsible for the longitudinal coupled-bunch instabilities while the dipole modes for the transverse coupled-bunch instabilities. The storable current is severely limited if the instability growth rate is greater than the natural damping of the bunch motion.

Figure 1.3 shows a Minkowski diagram for the case where a HOM-damped cavity is placed at the origin instead of the conventional cavity. The beam-induced HOM fields are quickly damped compared with the time interval to the next turn, so as to avoid the resonant buildup of the HOM fields acting back on the bunch. The concept of HOM-damped cavities is that the beam-induced HOM power needs to be quickly extracted out of the cavity and dissipated in external RF absorbers or loads while the accelerating mode should be kept inside with a minimal reduction in the shunt impedance, a measure of the conversion efficiency of RF power to the accelerating voltage.

Figure 1.4 is a Minkowski diagram showing the coupled-bunch instability when the accelerator is operated with multiple bunches (the number of bunches = 4). Usually, the cyclic interaction of the circulating bunches with the induced fields in the RF cavity is analyzed in the frequency domain rather than in the time domain. The theory of coupled-bunch instabilities has been mathematically formulated with use of the concept of impedance relating an action and the response. In chapter 4, the concept of coupling impedance is fully used in computer-aided design of a HOM damped structure for

KEKB. Currently, many textbooks are available on the theory of coupled-bunch instabilities in storage rings.

Various types of HOM-damped cavity structures have been proposed, and some of them have been fabricated, tested and operated so far to boost the collider performance toward the luminosity frontier. HOM-damped cavities can be classified in three categories as follows:

1) HOM damping with use of waveguides

2) HOM damping with use of a coaxial or radial line structure

3) HOM damping with use of beam pipes

The only feature common to these three categories is that the accelerating structure is a single cell cavity. Usually, multi-cell cavity structures are not used in ring colliders exploring not the energy frontier but the luminosity frontier, to avoid trapped modes in the coupled-cell structures and mechanical and thermal difficulties due to the complicated structures.

Figure 1.5 shows some HOM-damped cavities [4-7] belonging to the first category. According to their waveguide configurations, they are further classified into the threefold symmetric structure around the azimuth and the mirror symmetric structure with respect to the horizontal and vertical planes. The configuration with three waveguides [8] equally spaced around the azimuth is minimal to damp both of the horizontally and vertically polarized dipole modes. The width of the rectangular waveguide is adjusted to locate the cutoff frequency of the dominant TE10 mode between the accelerating mode and the lowest HOM, so as to allow all the HOMs to propagate away while retaining the accelerating mode in the cavity.

Figure 1.6 shows some HOM-damped cavities [9-12] belonging to the second category. In the case of a single cell cavity loaded with a coaxial line, the monopole and dipole HOMs are extracted in the TEM and TE11 modes, respectively. Since the TEM

mode does not have cutoff, the coaxial line needs a notch filter to block the accelerating mode. In design of HOM damped cavities with large coaxial line structures, it should be noted that the large inner conductor supported like a cantilever may deteriorates the thermal structural stability of the cavity in case of continuous-wave (CW) high-power operation.

Figure 1.7 shows some HOM-damped cavities [13-18] belonging to the third category. The origin of these cavities is "single-mode cavity" as illustrated in Fig. 1.8, which is the oldest HOM damped structure proposed by Weiland [13] in 1980's. By means of the computer codes TBCI [19] and URMEL [20], he has shown that a circular beam pipe itself with a large inside diameter could play a significant role as a waveguide for coupling out the unwanted HOMs from the cavity. The TM monopole HOMs couple to the TM01 waves propagating through the circular beam pipe, and the dipole HOMs couple to the TE11 waves. It should be noted here that the TM and TE dipole modes are mixed with each other due to the presence of the beam aperture as illustrated in Fig. 1.9. Therefore, the TM11n-like HOMs can couple to the TE11 waves. By enlarging the beam aperture together with optimization of the cavity cell shape, Weiland succeeded to couple out all the monopole HOMs through the beam pipes. However, two dipole modes (TM110-like and TE110-like modes) remained trapped below the TE11 cutoff frequency. That is because the magnetic field is dominant around the beam hole for these dipole modes, whose resonant frequencies shift lower when enlarging the beam hole. On the other hand, the electric field is dominant around the beam hole for the TM monopole modes, whose resonant frequencies shift higher when enlarging the beam hole. Anyway, he has demonstrated a quasi "single mode cavity", from which all the monopole HOMs are removed. He concluded that further optimization is needed to remove the lowest deflecting mode (TM110-like) in order to realize a perfect "single mode cavity".

A series of studies on HOM damping with "grooved beam pipe" [16, 17] started with breaking the cylindrical symmetry of "single mode cavity". The concept of "grooved beam pipe" is to selectively lower the cutoff frequency of the TE11 mode below the lowest TM110-like dipole mode by grooving the inner wall of the beam pipe.

Figure 1.7 also shows the evolution of HOM damping with use of beam pipes, diagrammatically with arrows. Additionally, the "grooved beam pipe" method could be more suitably applied to super-conducting (SC) cavities. That is because HOM waveguide apertures or ports are not allowed usually in the SC accelerating cell to avoid quenching under high accelerating gradients. Actually, the "grooved beam pipe" method has been applied to a single-cell SC cavity developed to upgrade Cornell Electron Storage Ring (CESR) for B-meson studies at Cornell University, although they call it "fluted beam pipe" [18].

The contents of the thesis are as follows:

In chapter 2, the idea of "grooved beam pipe" is introduced in order to damp the lowest dipole HOM by selectively lowering the cutoff frequency of the TE11 mode propagating in the original circular beam pipe. Next, the HOM damping properties of a simple pillbox cavity with grooved beam pipes at both ends are analyzed with use of a three-dimensional (3D) electromagnetic simulation code. The analysis procedure is based on Slater's "tuning curve method" for waveguide-loaded cavities. Also, the effect of the grooved beam pipe on the accelerating mode is investigated. That is because HOM damping is usually accompanied with some degradation in the Q value of the accelerating mode. The latter part of Chapter 2 describes the experiments with a 20%-scale model cavity, as the benchmark for further R&D, and compares those results with the 3D simulation results.

Chapter 3 describes the overall design of the normal conducting (NC) RF cavity system developed for KEKB. In addition to the HOM-related instability problems mentioned before, the operation of NC cavities under heavy beam loading conditions would give rise to another serious problem. That is the longitudinal coupled instabilities driven by the accelerating mode itself, whose resonant frequency is usually detuned toward the lower side from the RF frequency in order to compensate for the reactive component of the beam-induced cavity voltage. When this detuning becomes comparable to the beam revolution frequency or larger, violent longitudinal coupled-bunch instabilities would be unavoidable. Needless to say, we are not allowed to damp

the accelerating mode. In order to solve this problem, a three-cavity system operated in the $\pi/2$ mode has been developed for KEKB, in which an accelerating cavity is resonantly coupled with an energy storage cavity via a coupling cavity between. The storage cavity is used in order to reduce the frequency detuning by increasing the ratio of the electromagnetic stored energy of the accelerating mode to the beam loading. Moreover, the coupling cavity is equipped with a parasitic mode damper against the 0 and π modes emerging at both side of the $\pi/2$ mode. This coupled cavity system was later named ARES, which is the acronym for Accelerator Resonantly coupled with Energy Storage.

Chapter 4 describes the application of the grooved beam pipe method to the ARES cavity system. Needless to say, the accelerating cavity itself of the ARES system must be a HOM-damped cavity. Furthermore, the adopted HOM-damped structure needs to be structurally compatible with a boundary condition inherent in the ARES cavity system, i.e. two coupling apertures at both sides of the accelerating cavity: one toward the coupling cavity, and the other toward a half-cell coupling cavity for the $\pi/2$ mode termination keeping the accelerating field symmetrical with respect to the vertical mid plane including the beam axis. The grooved beam pipe scheme has been successfully applied to meet this boundary condition. Together with detailed studies on the HOM damping properties, the optimization of the grooved beam pipe structure is also discussed in relation to the fundamental mode heating of the SiC tiles due to the mirror symmetry breaking caused by insertion of a movable tuning plunger into the accelerating cavity.

In chapter 5, two beam-based experiments on the HOM-damped structure of the ARES cavity system are described. One is HOM spectrum measurement of the conceptual demonstrator ARES96, which was carried out in the TRISTAN AR before the cavity production for KEKB project. The other is HOM power measurement of some ARES cavities actually operated for the LER of KEKB to support the high-current beam over 1000 mA.

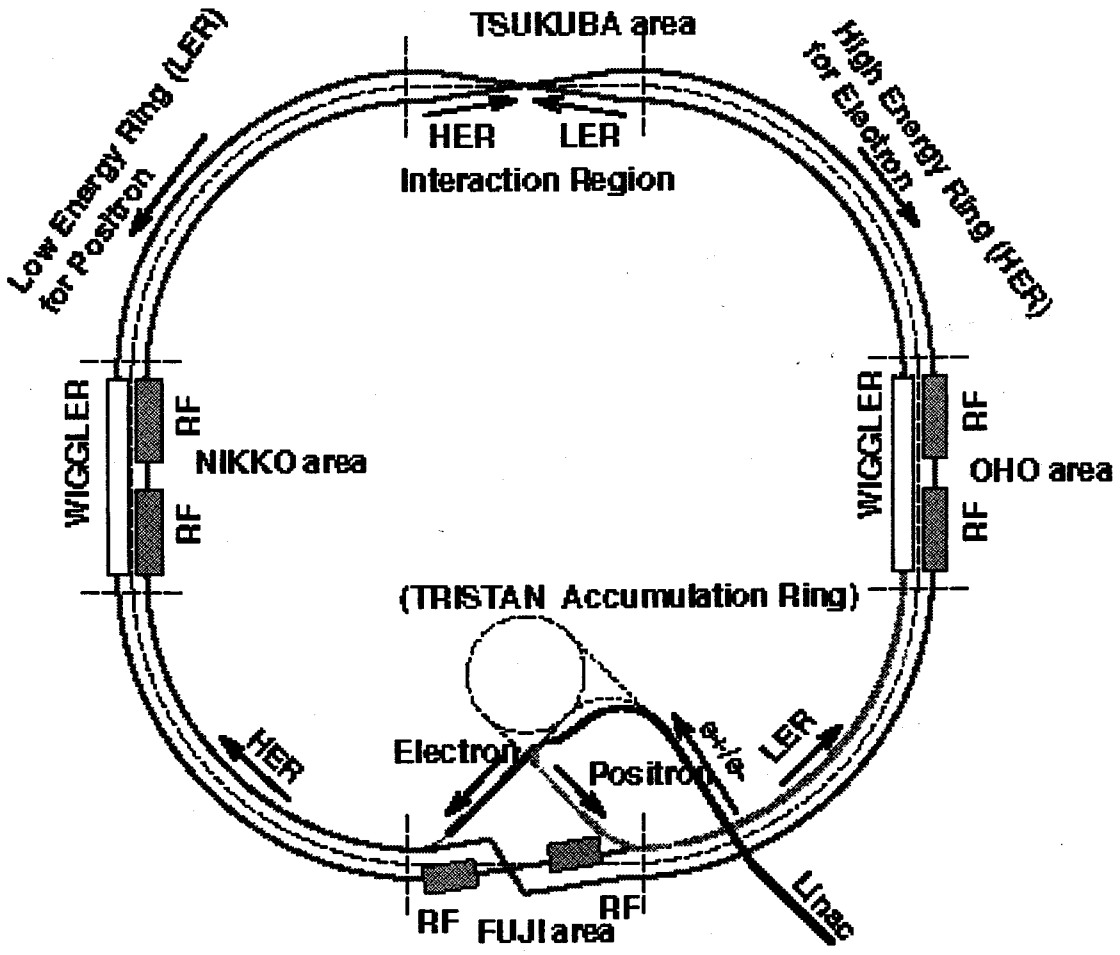

HER e^- beam (8 GeV, 1.1 A) × LER e^+ beam (3.5 GeV, 2.6 A) → $L = 1 \times 10^{34}$ $cm^{-2}s^{-1}$

Figure 1.1. KEKB Collider

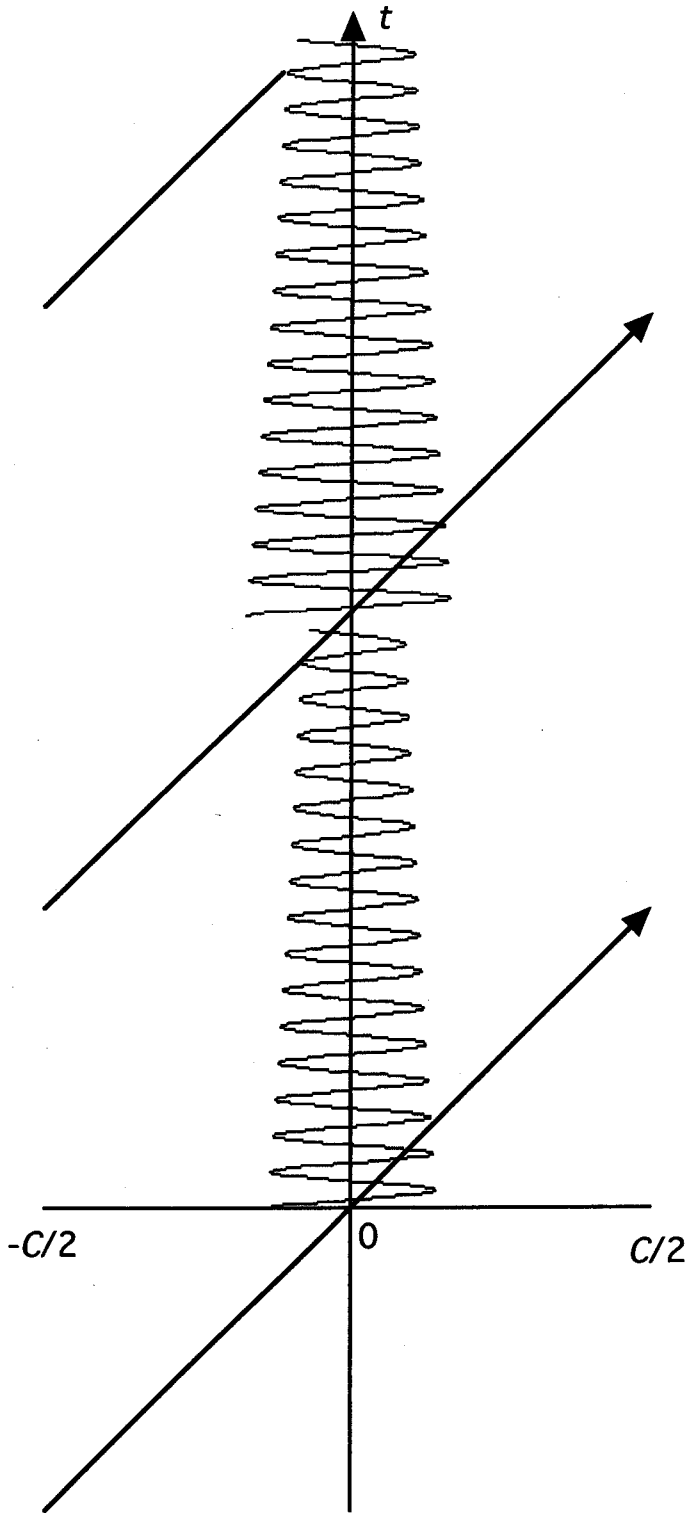

Figure 1.2. Minkowski diagram showing resonant buildup of beam-induced HOM field driving coupled-bunch instability.

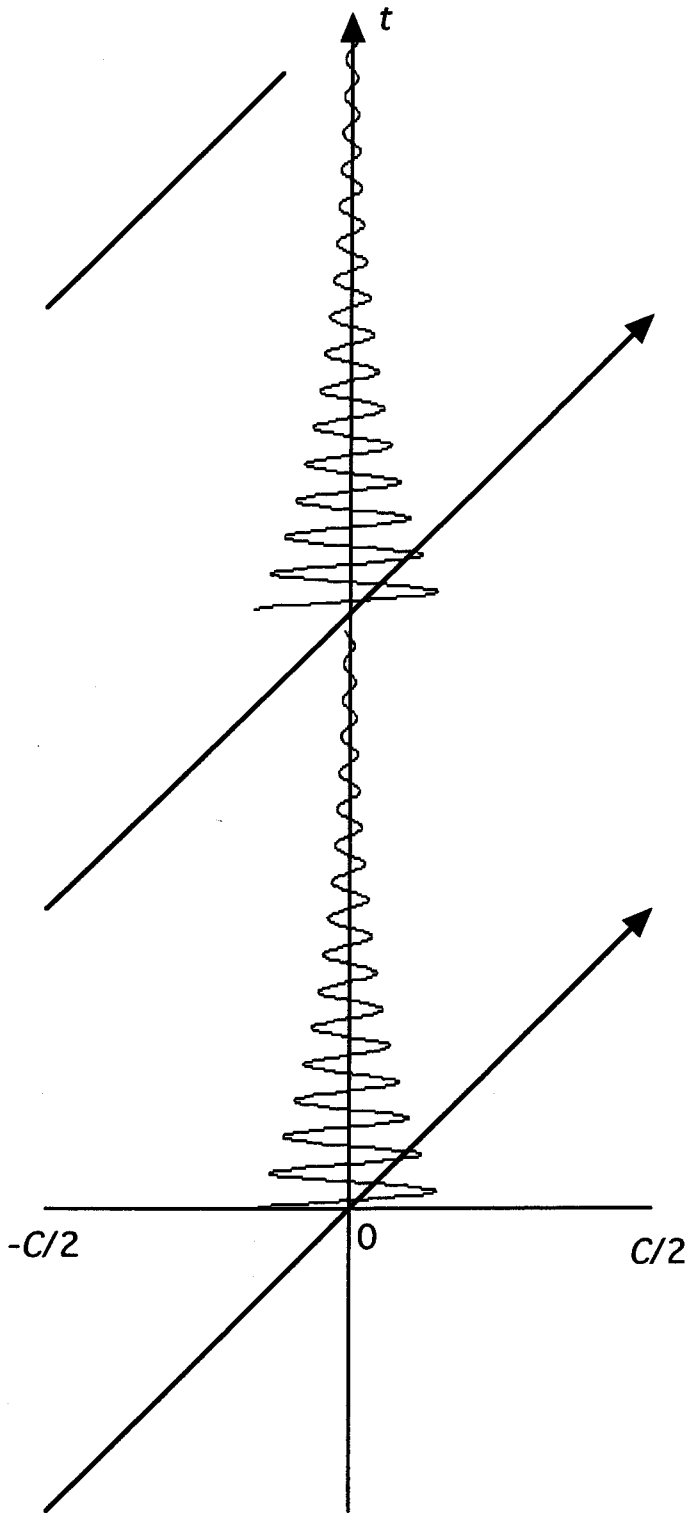

Figure 1.3. Minkowski diagram showing suppression of resonant buildup of beam-induced field with a HOM-damped cavity.

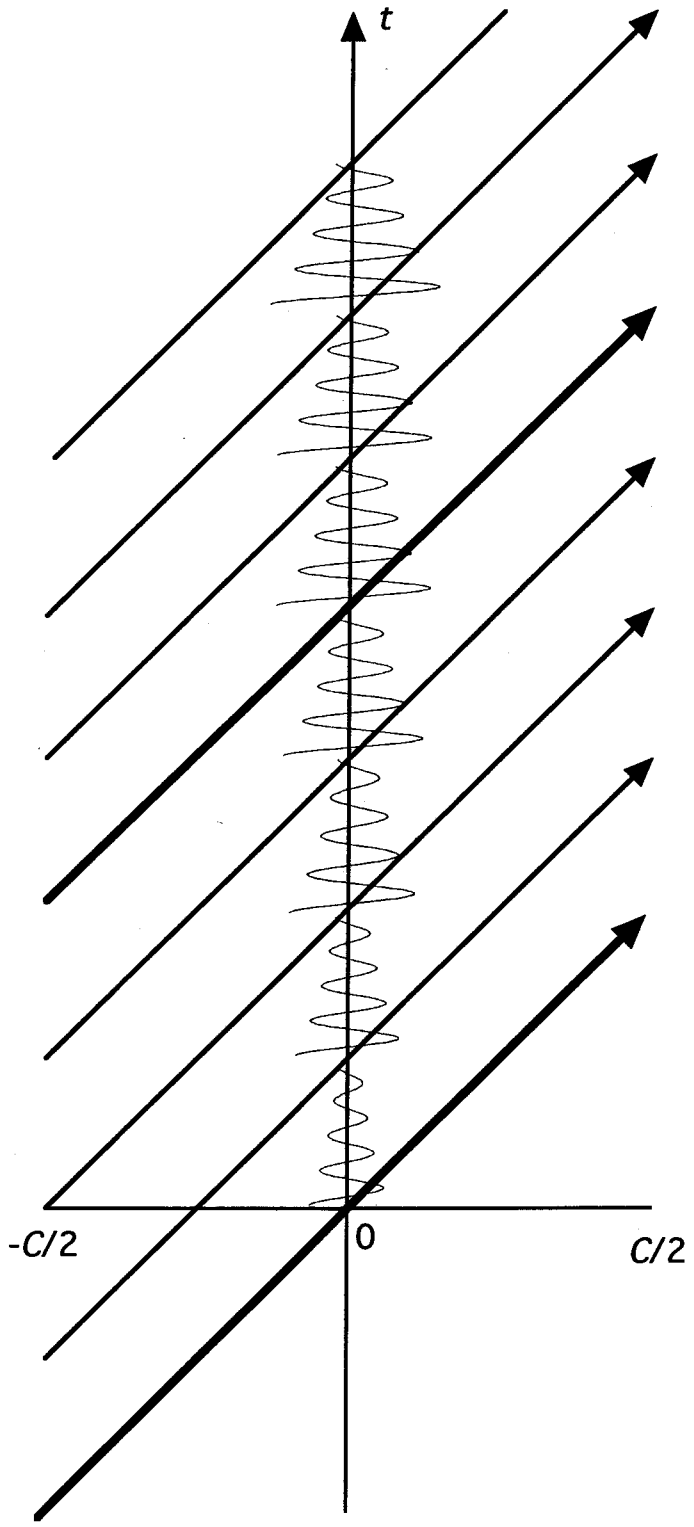

Figure 1.4. Minkowski diagram showing coupled-bunch instabilities when four bunches circulating in the ring.

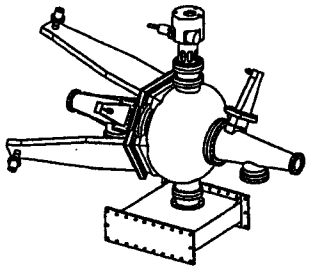

The DAFNE Cavity [4]

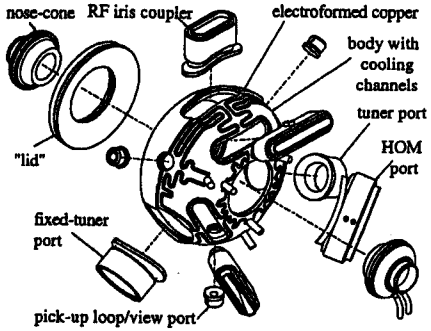

The PEP-II Cavity [5]

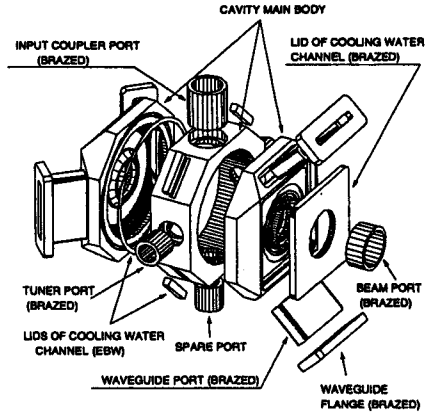

The ATF Cavity [6]

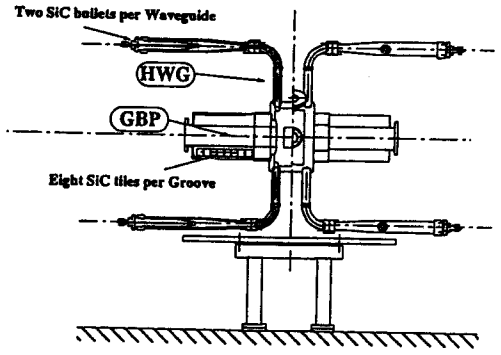

The KEKB ARES Cavity (ARES96) [7]

Fig. 1.5. HOM Damping with Waveguides.

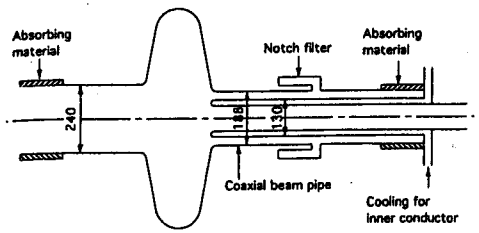

Superconducting Crab Cavity [9]

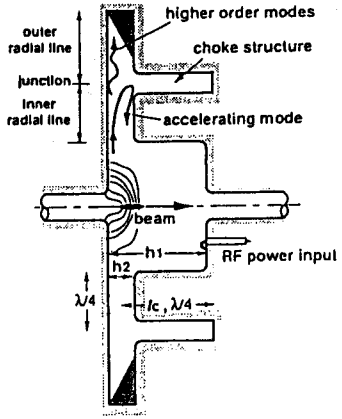

Choke Mode Cavity [10]

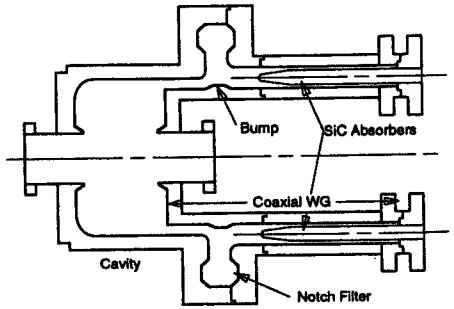

The KEKB Cavity Prototype [11]

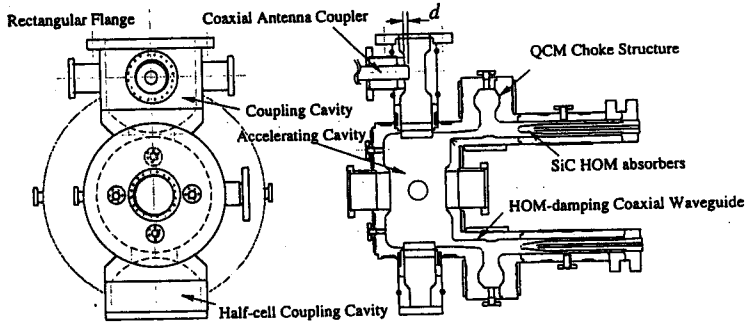

The KEKB ARES Cavity (ARES95) [12]

Figure 1.6. HOM Damping with a Coaxial or Radial Line Strucuture.

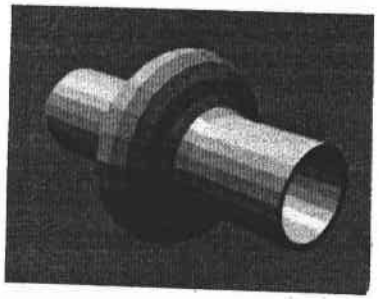

Single Mode Cavity [13]

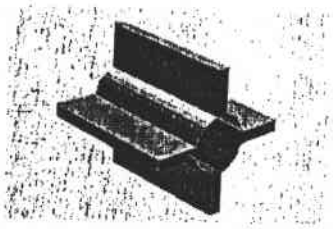

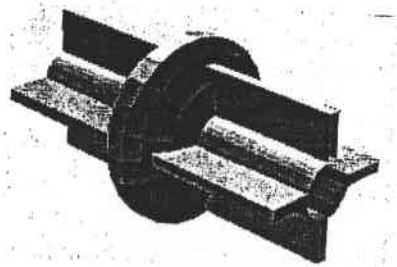

HOM-Damped Cavity with Grooved Beam Pipes [16, 17]

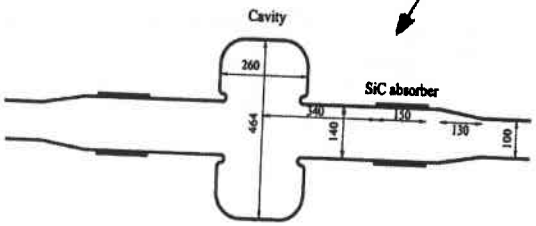

Cavity with SiC Beam Ducts [14]

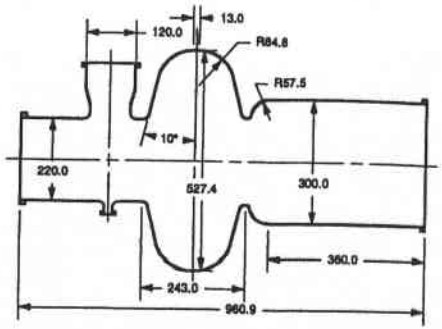

The KEKB Superconducting Cavity [15]

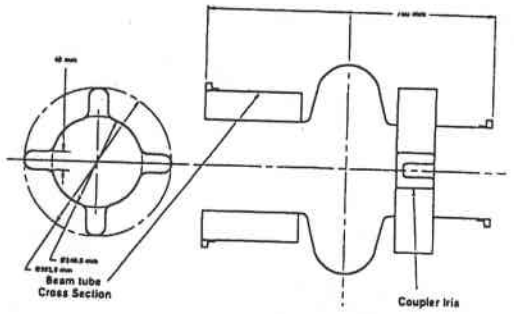

The CESR Superconducting Cavity [18]

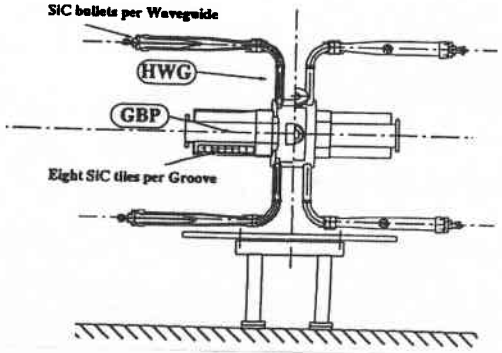

The KEKB ARES Cavity (ARES96) [7]

Figure 1.7. HOM Damping with Beam Pipes.

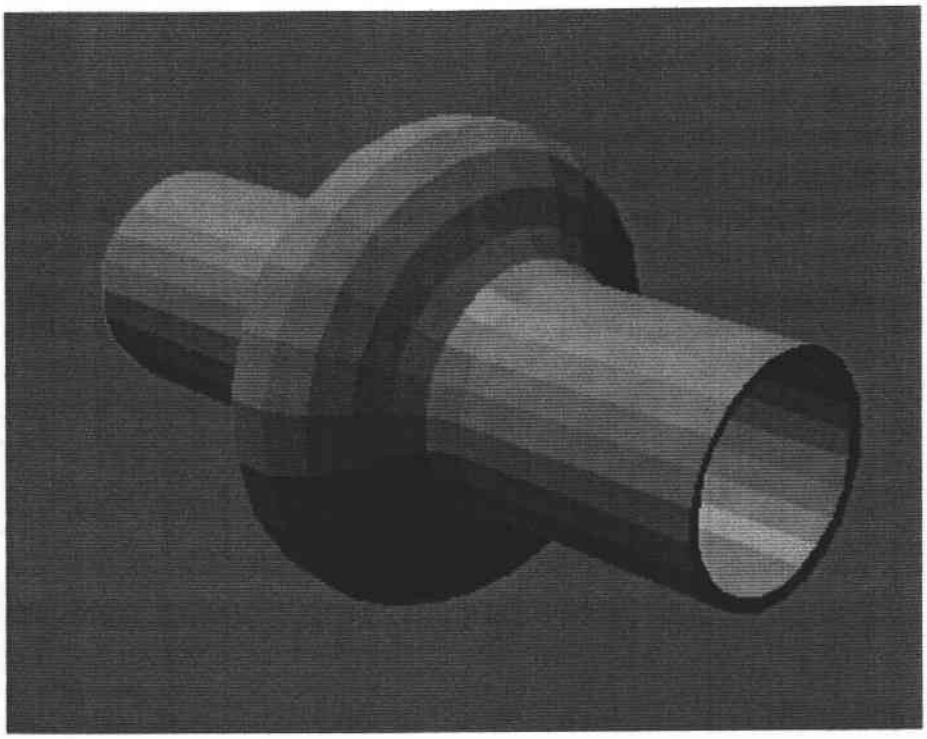

Fig. 1.8. "Single Mode Cavity" Conceptual Design

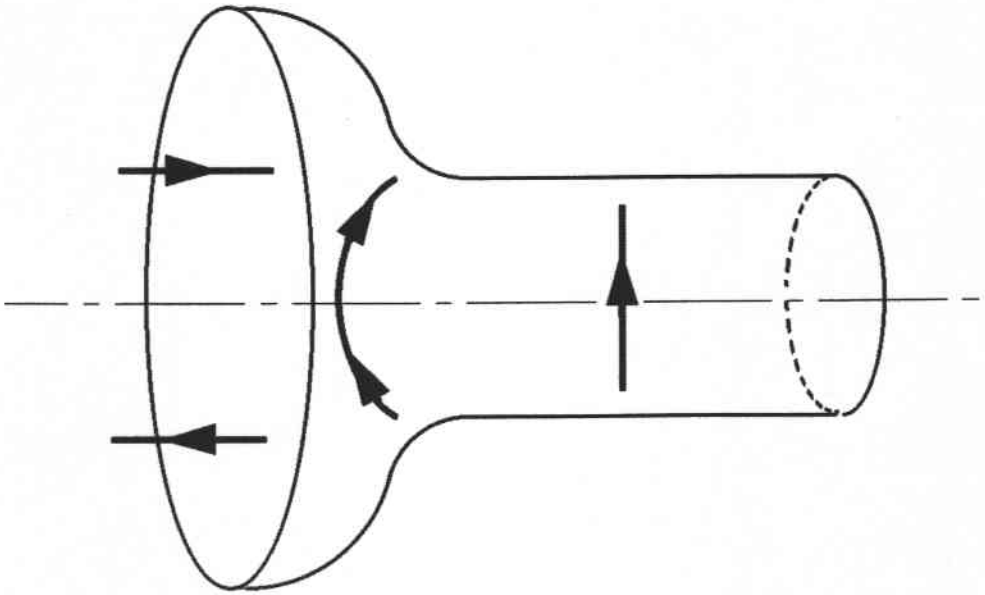

Fig. 1.9. TM11-TE11 Mode Mixing

Chapter 2.
HOM DAMPING WITH GROOVED BEAM PIPE

2.1. Grooved Beam Pipe

As mentioned in the introduction of "single-mode cavity", the TM monopole HOMs of the RF accelerating cavity couple to the TM01 mode propagating through the circular beam pipe, and the dipole HOMs couple to the TE11 mode. In the case of a circular waveguide of radius a, the cutoff frequency of the TM01 mode is given by

$$f_c = \frac{cx_{01}}{2\pi a}, \tag{2.1}$$

where c is the speed of light and $x_{01} = 2.405$ is the first root of the equation $J_0(x) = 0$, while the cutoff frequency of the TE11 mode is given by

$$f_c = \frac{cx'_{11}}{2\pi a}, \tag{2.2}$$

where $x'_{11} = 1.841$ is the first root of the equation $J'_0(x) = 0$. The electric and magnetic field profiles of the TM01 and TE11 modes are shown at the top and middle in Fig. 2.1, respectively.

The bottom in Figure 2.1 shows the field profiles of the dominant TE10 mode propagating in a rectangular waveguide. In the case of a rectangular cross section of width a and height b, the cutoff frequency of the TE10 mode is given by

$$f_c = \frac{c}{2a}. \tag{2.3}$$

Thus, the cutoff frequency of the dominant TE10 mode of a rectangular waveguide is determined by its width only.

Comparing the field profiles of the TE11 mode in a circular waveguide with those of the TE10 mode in a rectangular waveguide, we can conclude that both modes are topologically the same. Further topological investigation leads us to another important fact that the cutoff frequency of the TE11 mode in a circular waveguide is sensitive to the width measured in the radial direction perpendicular to the polarization of the electric field, and finally to the idea of "grooved beam pipe" to selectively lower the TE11 cutoff by grooving the inner wall of the beam pipe.

Let us start with a circular beam pipe with four grooves [16, 17] at every 90 degrees in azimuth around the beam axis as shown in Fig. 2.2. A beam pipe structure with fourfold symmetry is natural in case of damping horizontally polarized dipole modes and vertically polarized ones together. However, the threefold symmetry is actually minimal for dealing with both polarizations as mentioned in the previous chapter. Needless to say, the twofold symmetry is enough in case of damping dipole modes polarized in one direction.

Figure 2.3 shows the dependence of the TE11 cutoff frequency on the groove depth for a beam pipe with fourfold symmetry, where the inside diameter of the circular part is 10 cm and the groove width is 2 cm. Changing the groove depth from 0 cm to 11 cm, the cutoff frequency of the TE11 mode was calculated with MAFIA [21], which is a popular 3D electromagnetic simulation code widely used in accelerator design. Figure 2.4 shows the 3D mesh geometry implemented to MAFA, where a quarter part of the whole structure is enough owing to the fourfold symmetry. As the groove becomes deeper, the cutoff frequency of the TE11 mode becomes lower as expected from a topological analogy with the TE10 mode propagating in a rectangular waveguide. Assuming a pillbox-type cavity with the accelerating mode (TM010) at 500 MHz, the groove should be deeper than 7 cm to extract the RF power of the TM110 mode at 790 MHz through the beam pipe. Moreover, the TM110 mode could be more heavily damped with a deeper groove depth giving a larger group velocity to the TE11 mode propagating at the frequency of 790 MHz.

Figure 2.5 shows the electric and magnetic field plots from MAFIA for the TE11 mode with vertical polarization when the groove depth is 11 cm. The electric field

density is high around the entrance of the horizontal groove while almost no electromagnetic fields inside the vertical groove. According to these field plots, RF absorbers of dielectric materials should be placed inside the grooves if possible. This absorber arrangement enables effective energy dissipation of the TE11 mode along the beam pipe and also suppression of heating of the absorbers by the bunched beam accompanied with TEM-like electromagnetic fields. Focusing on the latter heating problem only, the groove width should be narrower than $\sim\pi\sigma_z$, where σ_z is the bunch length assuming a Gaussian shape.

2.2. HOM Damping Properties

In this section, we will confine ourselves to damping the TM110-like mode with the grooved beam pipe scheme. In the case of damping the monopole HOM (TM011) with the lowest frequency together, the inside diameter of the circular pipe should be increased like "single mode cavity" because the cutoff frequency of the TM01 mode is not affected so much by grooving the inner wall of the beam pipe.

Figure 2.6 shows a pillbox-type cavity loaded with grooved beam pipes with the same cross section at both end plates, adopted as a simple model for fundamental studies on the HOM damping properties. The inside diameter of the cavity is set to 46 cm so as to locate the TM010 and TM110 modes at 500 MHz and at 790 MHz, respectively. That is just for convenience to people involved in KEKB. The inside diameter of 10 cm and the groove width of 2cm are the same as in the previous section. The groove depth is set to 11 cm so as to lower the cutoff frequency of the TE11 mode to 570 MHz, far below the TM110 mode, but 70 MHz above the accelerating mode.

Figure 2.7 shows a schematic drawing of the coupling aperture between the pillbox cell and the grooved beam pipe. The four radial slots around the circular beam bore function like inductive shutters for adjusting the coupling between the cavity and the beam pipe. The slot width is equal to the groove width. The slot length, indicated by SL, can be changed from 0 cm to 11 cm. When SL = 0 cm, the coupling aperture becomes the circular bore with a diameter of 10 cm. When SL = 11 cm, the shape of the coupling

aperture becomes the same as the cross section of the beam pipe.

Next, we investigate the external Q value of the TM110 mode of the cavity coupled to the grooved beam pipes, which extend infinitely in both directions. The external Q value gives a measure of mode damping by extracting the RF power from a cavity. The external Q value can be calculated using a theory developed by Slater [22], based on the tuning curve for a resonant cavity coupled with a waveguide terminated with a movable short-circuiting plunger as shown in Fig. 2.8. The terminated waveguide functions as a tunable resonator. Here, we assume that the cavity has a resonance at f_a in the frequency range of our concern. Then, the frequency f of this coupled-resonator system is determined from the plunger position d by the following equation:

$$d = \frac{\lambda_g}{2\pi} tan^{-1} \frac{\frac{1}{Q_{ext}}}{\frac{f}{f_a} - \frac{f_a}{f}} + \frac{1}{2} n\lambda_g, \quad n = \text{integer}, \tag{2.4}$$

where Q_{ext} is the external Q value of the cavity resonance and λ_g the guide wavelength corresponding to the frequency f. Figure 2.9 shows a typical tuning curve response. The plunger position d is the distance measured from a fiducial surface, referred to as "detuned short surface", where the RF wave toward the cavity is reflected when the cavity resonance is detuned from the RF frequency. When $f = f_a$, Eq. (2.4) becomes

$$d = \left(\frac{1}{4} + \frac{n}{2}\right)\lambda_g, \quad n = \text{integer}. \tag{2.5}$$

This equation means that the waveguide resonator has an electrical length of $(1/4 + n/2)$ times of the guide wavelength corresponding to the resonant frequency f_a. At the intersections of the tuning curves and a family of straight lines represented by Eq. (2.5), the tuning curve response becomes stationary with respect to the plunger position d, indicating that the waveguide resonator is detuned from the cavity resonance. Further, differentiating Eq. (2.4) with respect to λ_g at the stationary points, we obtain:

$$\frac{dd}{d\lambda_g} = \frac{2n+1}{4} + \frac{Q_{ext}}{\pi}\frac{v_g}{v_p}, \quad n = \text{integer}, \tag{2.6}$$

where v_g and v_p are the group and phase velocities of the guided wave, respectively. According to Eq. (2.6), the external Q value can be calculated from the differential coefficient of the tuning curve at every stationary point. Slater's tuning curve method is very useful and widely used in design of waveguide-loaded cavity structures, and recently in design of HOM-damped cavity structures. Examples are found in Refs. [23, 24].

For each case of different coupling apertures SL = 0, 3, 5, 7, 9 and 11 cm, the tuning curve was obtained with the eigenmode solver of MAFIA. Figure 2.10 shows the three-dimensional geometry implemented to MAFIA, where one eighth part of the whole structure under investigation is enough owing to its symmetry. The resonant frequencies were calculated changing the length of the grooved beam pipe. The boundary condition at the end of the beam pipe was set to "electric short" corresponding to the head of the movable short-circuiting plunger.

Figure 2.11 shows the tuning curve responses obtained for SL = 0, 3, 5 and 9 cm. On the horizontal axis, the resonant frequency is expressed in terms of the guide wavelength λ_g of the TE11 mode propagating in the grooved beam pipe. On the vertical axis, the position of the short-circuiting plane d is measured from the center of the cavity instead of the reference position "detuned short surface". The dashed lines in Fig. 2.11 represent the tuning curves when the cavity and the beam pipe are isolated from each other. The vertical dashed line corresponds to the TM110 resonance in the cavity independent of the plunger position d, and the slant dashed lines with slopes $n/2$ (n=1,2, and 3) correspond to the standing-wave modes TE11n in the beam pipe, respectively. As the slot length SL increases, two tuning curves repel each other further at every intersection of the dashed lines, which means the coupling between the cavity and the beam pipe becomes stronger.

For each slot length SL, the external Q value of the TM110 mode was obtained in

two different ways: the first directly from the differential coefficients $dd/d\lambda_g$ at the stationary points, using Eq. (2.6); the second by fitting the tuning curves with a modified form of Eq. (2.4):

$$d - d_0 = \frac{\lambda_g}{2\pi} tan^{-1} \frac{\frac{1}{Q_{ext}}}{\frac{f}{f_a} - \frac{f_a}{f}} + \left(\frac{n}{2} + k\right)\lambda_g, \; n = \text{integer}, \tag{2.7}$$

with four free parameters f_a, Q_{ext}, d_0, and k, where the frequency dependence of the position of "detuned short surface" is taken into account up to the first order of λ_g as:

$$d_0 + k\lambda_g \; . \tag{2.8}$$

The original equation (2.4) by Slater assumes that the position of "detuned short surface" is independent of the frequency. This assumption is valid when the coupling between the cavity and waveguide is weak, in other words, when the coupling aperture size is small enough compared with the guide wavelength of the propagating mode. However, the frequency dependence of the reference position is no more negligible when the coupling aperture size becomes comparable with the wavelength.

The external Q values calculated directly from $dd/d\lambda_g$ are plotted as a function of *SL* in Fig. 2.12, together with those obtained by curve fitting with Eq. (2.7). Table 2.1 summarizes the simulation results, where the resonant frequency of the TM110 mode was also obtained by fitting the tuning curve for each case. There is fair agreement between the two methods. It can be seen that the external Q value rapidly decreases from ~1900 to ~12 as *SL* increases from 0 cm to 7 cm, indicating that the grooved beam pipe scheme is very effective to damping the TM110 mode heavily. On the other hand, the external Q value remains almost constant in the range of SL larger than 7 cm. That is probably because the lower limit of the external Q value is determined by the group velocity of the TE11 mode propagating through the grooved beam pipe.

Table 2.1: External Q values for SL = 0, 3, 5, 7, 9, and 11 cm obtained directly from $dd/d\lambda_g$ and from fitting the tuning curves, together with resonant frequencies also obtained from fitting.

SL (cm)	Q_{ext} from $dd/d\lambda_g$	Q_{ext} from curve fitting	f_a (MHz) from curve fitting
0	1870	1900	789.5
3	163	171	782.4
5	32.7	35.9	775.4
7	12.1	12.5	780.4
9	10.9	9.96	798.4
11	12.2	10.8	801.8

2.3. Effect on the Fundamental Mode

Usually, heavy HOM damping is accompanied with some degradation in the Q value of the fundamental TM010 mode because the HOM waveguide apertures disturb the wall surface currents. Therefore, the effect of the grooved beam pipes on the fundamental mode needs to be investigated. Table 2.2 summarizes the RF properties of the fundamental mode calculated with MAFIA for each case of the slot length SL = 3, 5 and 7 cm, together with those for the cavity equipped with circular beam pipes of the same inside diameter of 10 cm. According to Table 2.2, we can conclude that the performance degradation of the fundamental mode due to the grooved beam pipes is negligibly small. This result can be explained as follows. First, the wall surface currents of the TM010 mode do not cross the radial slots around the beam bore. Second, the fourfold symmetry do not allow the TM010 mode to couple with the TE11 dipole mode propagating in the beam pipe.

Table 2.2. RF properties of the accelerating mode

CBP = Circular Beam Pipe, GBP = Grooved Beam Pipe, R = shunt impedance

Type	SL (cm)	f (MHz)	R/Q (Ω)	Q	R (MΩ)
CBP	-	502.7	187	42600	7.97
GBP	3	503.1	186	42700	7.93
GBP	5	503.2	186	42800	7.95
GBP	7	503.2	186	42900	7.98

2.4. Experiments with Model Cavity

Motivation

Two experiments with a model cavity were carried out in order to verify the results of the computer-aided studies on a pillbox cavity loaded with grooved beam pipes. Another important purpose of these experiments was to offer a benchmark to Slater's tuning curve theory. The first experiment was carried out, exactly following Slater's recipe, to measure indirectly the external Q value of the TM110 mode in the model cavity, where a half-cell pillbox cavity is coupled with a grooved beam pipe terminated with a movable short-circuiting plunger. The second experiment was performed to measure directly the loaded Q value of the TM110 mode by terminating the grooved beam pipe with an RF absorber instead of the short-circuiting plunger. When the damping due to the RF power outgoing through the grooved beam pipe is dominant, the loaded Q value Q_L becomes nearly equal to the external Q value Q_{ext} as represented by

$$\frac{1}{Q_L} = \frac{1}{Q_{ext}} + \frac{1}{Q_0},$$

where Q_0 is the unloaded Q value due to the wall losses inside the cavity.

Model Cavity

Figure 2.13 is a drawing of the model cavity made of aluminum, which is exactly 20% scale of a half part of the structure investigated in the section 2.3, split with respect to the middle plane perpendicular to the beam axis. Electrically shorting at the middle plane of the cavity forbids the TM011 and TE111-like modes, which exist in the vicinity of the TM110-like mode of our great concern. Usually, forbidding unwanted modes with appropriate boundary conditions is very effective to make experiments or measurements simple and clear. At the coupling aperture to the grooved beam pipe, the model cavity has a slot length of 1 cm, which corresponds to the full-scale case of SL = 5 cm. From the end of the grooved beam pipe, a movable short-circuiting aluminum plunger is to be inserted. The plunger has almost the same cross section as the grooved beam pipe, and was precisely machined so as to fit tightly and also slide smoothly inside the pipe.

Experiment with a Movable Short-Circuiting Plunger

Figure 2.14 is a photo of the measurement set-up. The model cavity stood with its beam axis in the vertical direction so that the short-circuiting plunger could slide more smoothly inside the grooved beam pipe compared with a set-up in the horizontal direction, reducing the error due to the electrical contact condition depending on the plunger position. Following Slater's recipe, the measurement was carried out by changing the position of the shorting plunger by 2- or 4-mm step within an accuracy of 0.01 mm. At each step, the resonant frequencies of the waveguide-loaded cavity were measured with a network analyzer HP8510 (Agilent Technologies Inc.). The temperature of the cavity body was kept as constant as possible during a stroke of the plunger.

Figure 2.15 shows a set of tuning curves obtained from the measurements. The resonant frequencies, expressed in terms of the guide wavelength of the TE11 mode in the grooved beam pipe, are plotted as a function of the plunger head position, measured from the end plate at the left side in Fig. 2.13. Using Eq. (2.5), the external Q value was calculated from the differential coefficient of $dd/d\lambda_g$ at each of the two stationary points in Fig. 2.15, where the grooved beam pipe is detuned from the TM110 resonance

of the cavity. The results are summarized in Table 2.3, where both experimental values agree well with the predicted value of 32.7 for the case of $SL = 5$ cm in Table 2.1.

Table 2.3.

stationary point	$dd/d\lambda_g$	Q_{ext}	f_a (GHz)
$\lambda_g/4$	4.94	32.8	3.857
$3\lambda_g/4$	5.41	32.6	3.857

Experiment with an RF Absorber

Figure 2.16 is a photo of the measurement set-up with an RF absorber inserted from the end of the grooved beam pipe. The RF absorber is made of silicon carbide (SiC) ceramic material (Cerasic-B, Toshiba Ceramics Inc.), sintered into a bullet shape as shown in Fig. 2.17. The resonant frequency and loaded Q value of the TM110 mode were directly measured. The results are listed in Table 2.4, showing fair agreement with those obtained from Slater's tuning curve method.

Table 2.4.

resonant frequency (GHz)	loaded Q value
3.849	32.3

In this experiment, the performance of the SiC load, expressed in terms of VSWR (Voltage Standing Wave Ratio), significantly determine the systematic errors. In order to estimate the VSWR, the complex permittivity $\varepsilon' - j\varepsilon''$ of the SiC material was measured at 3.8 and 3.9 GHz near the TM110 resonance, with use of a dielectric probe kit (HP 85070B, Agilent Technologies Inc.) attached to the network analyzer. The results are listed in Table 2.5, expressed in terms of the real part of the relative permittivity $\varepsilon_r \equiv \varepsilon'/\varepsilon_0$ and the loss tangent $tan\delta \equiv \varepsilon''/\varepsilon'$. With these dielectric constants, the return loss of the SiC load was calculated with use of the computer program High-Frequency

Structure Simulator (HFSS, Agilent Technologies Inc.). Figure 2.18 shows the three-dimensional geometry implemented into HFSS, where the bullet-shape SiC load is inserted from the free space into the grooved beam pipe. Figure 2.19 shows the simulation results, where the return loss of the SiC load is plotted as a function of frequency. According to this graph, the VSWR of the SiC load was estimated lower than 1.1 in the frequency range of our concern, and satisfactory for the purpose of this experiment.

Table 2.5. Dielectric constants of the SiC material.

frequency (GHz)	$\varepsilon_r \equiv \varepsilon'/\varepsilon_0$	$tan\delta \equiv \varepsilon''/\varepsilon'$
3.8	14.9	0.586
3.9	14.8	0.579

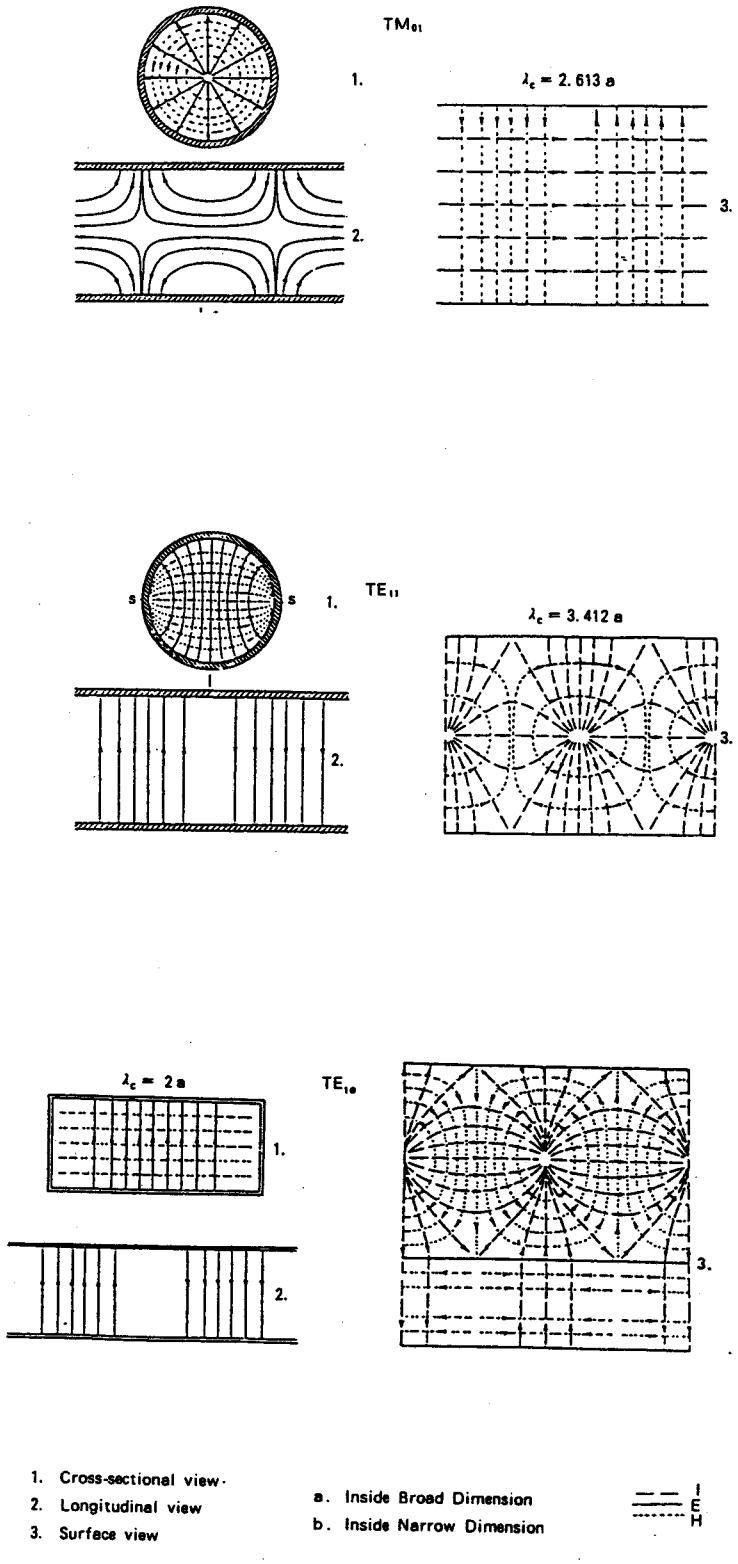

Fig. 2.1. The electric and magnetic field profiles are shown for the TM01 and TE11 modes for a circular waveguide, together with those for the TE10 mode for a rectangular waveguide (from Waveguide Handbook, MIT Rad. Lab. Sieies, vol. 10).

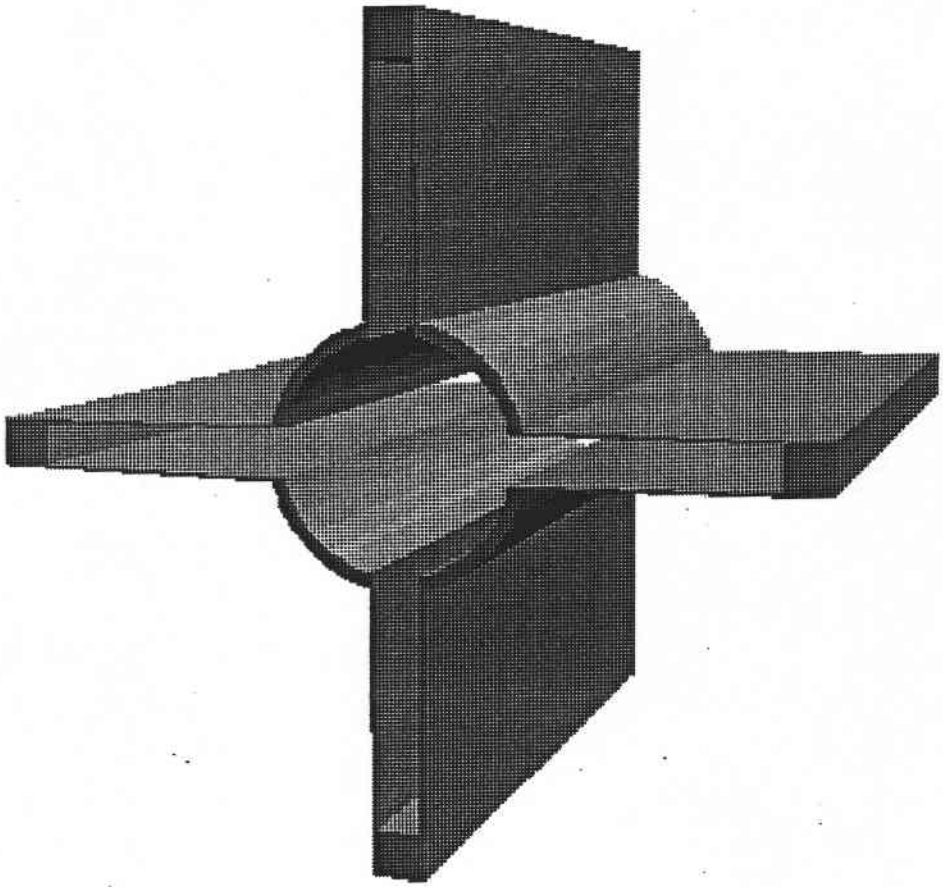

Fig. 2.2. Grooved beam pipe with fourfold symmetry.

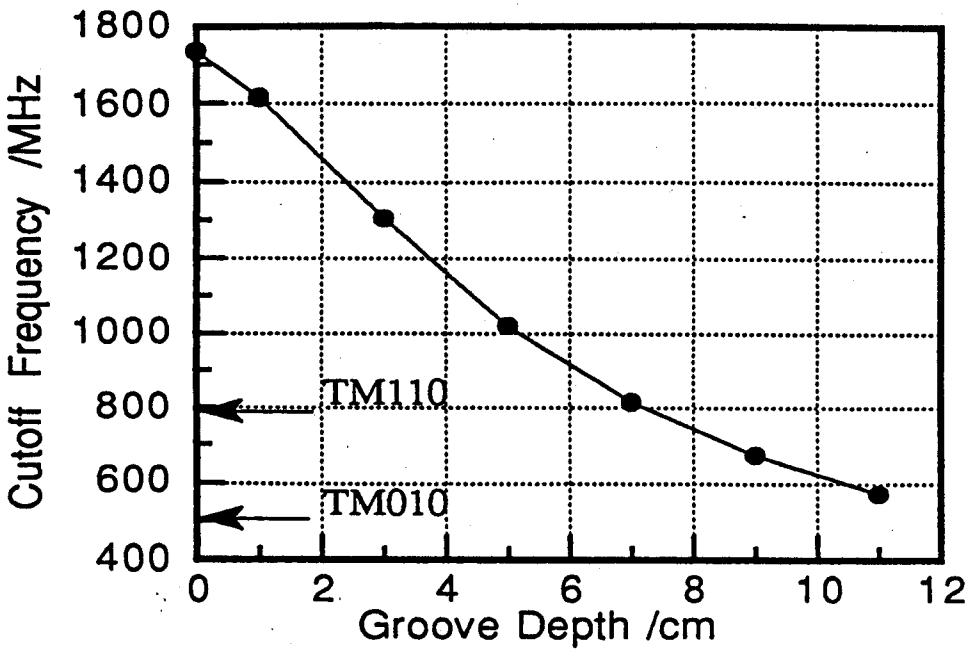

Fig. 2.3. The dependence of the TE11 cutoff frequency on the groove depth, computed with MAFIA.

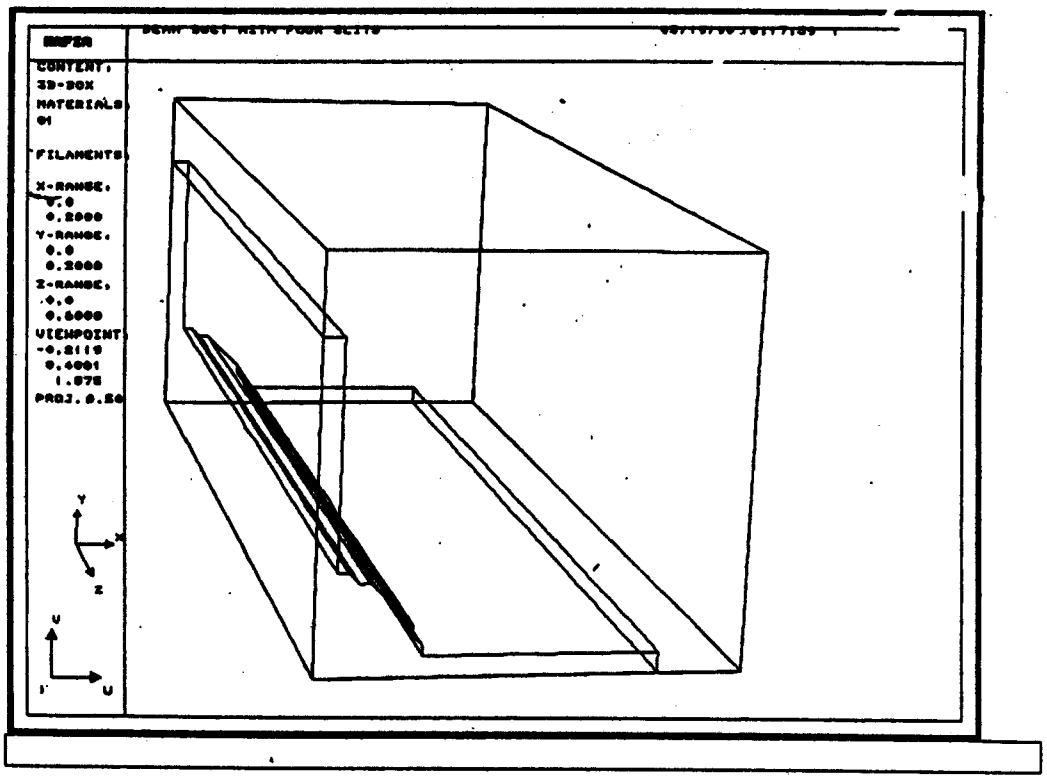

Fig. 2.4. The geometry implemented to MAFIA to compute the TE11 cutoff frequency of the grooved beam pipe.

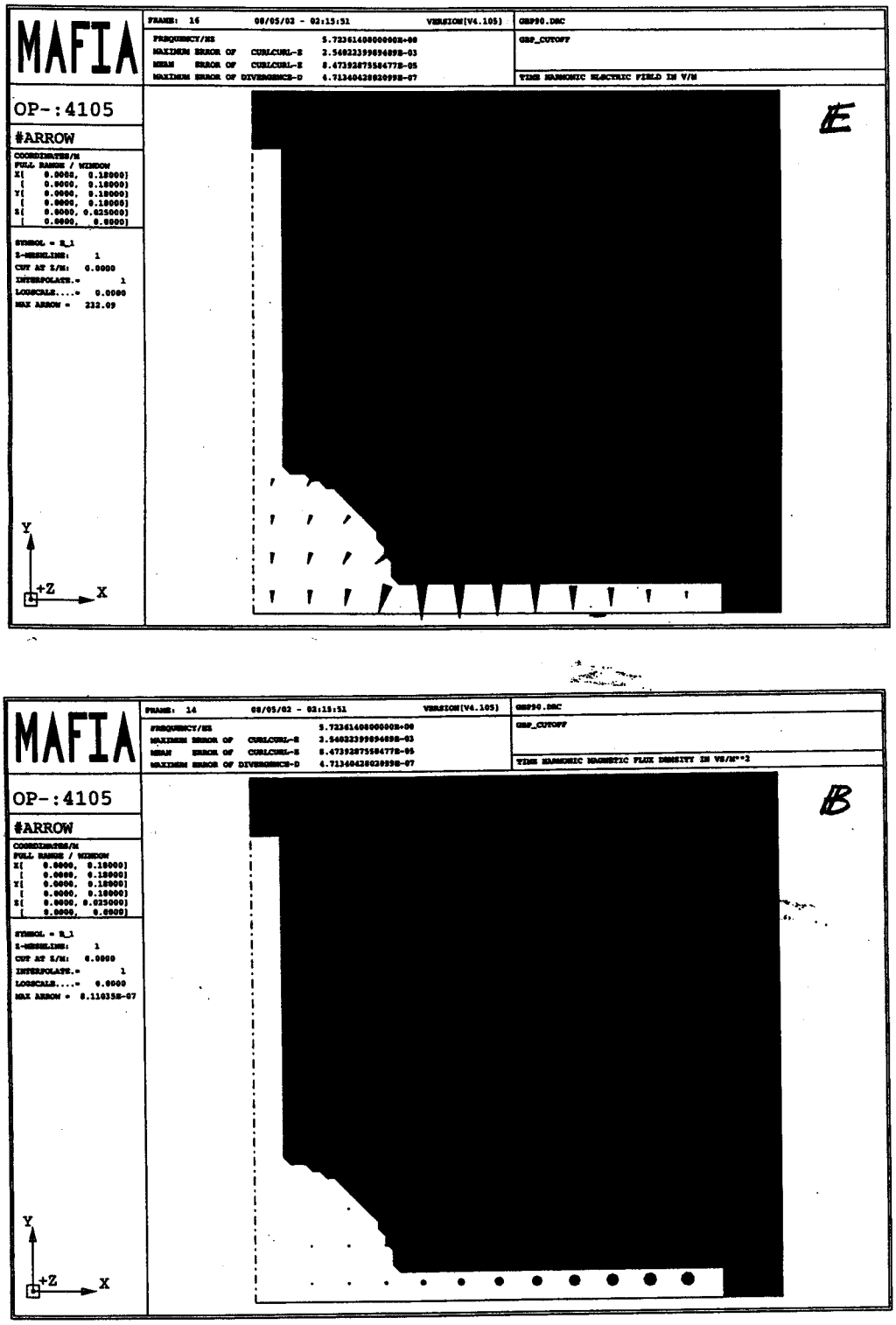

Fig. 2.5. The electric and magnetic field patterns, obtained with MAFIA, for the TE11 mode propagating in the grooved beam pipe.

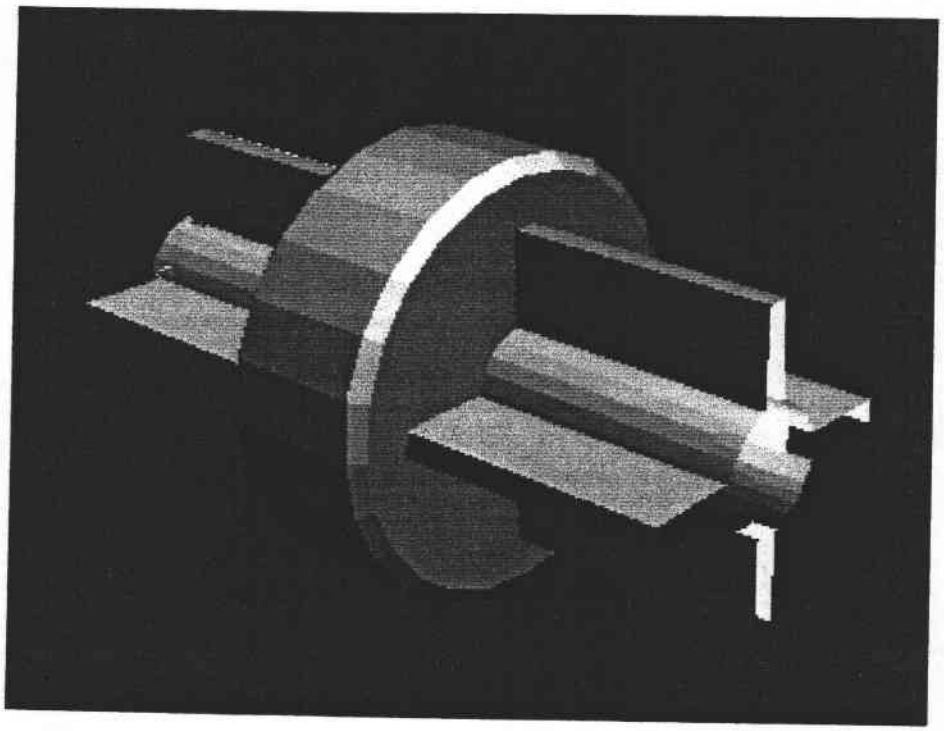

Fig. 2.6. Pillbox cavity loaded with grooved beam pipes at both ends.

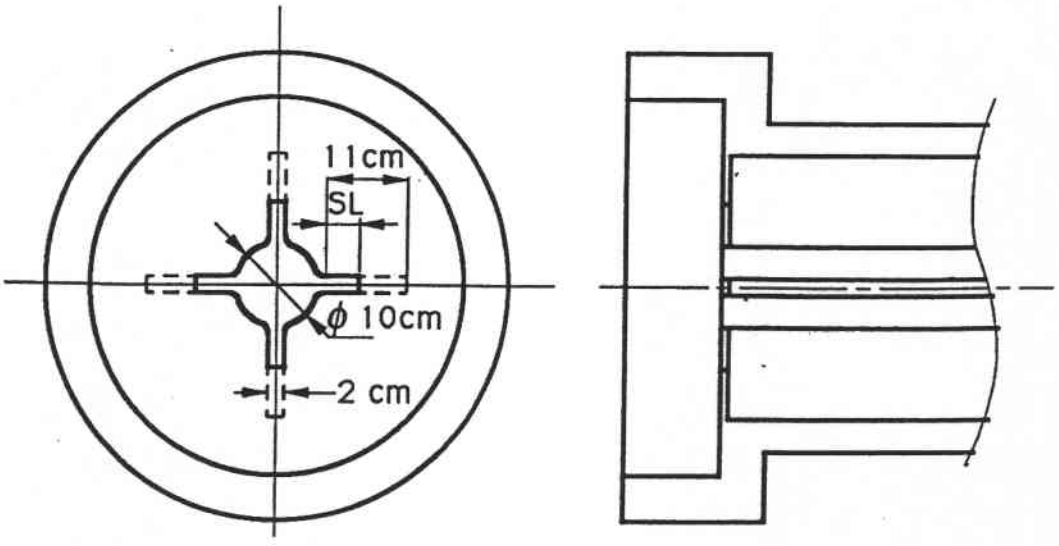

Fig. 2.7. A schematic drawing of the coupling aperture to the grooved beam pipe.

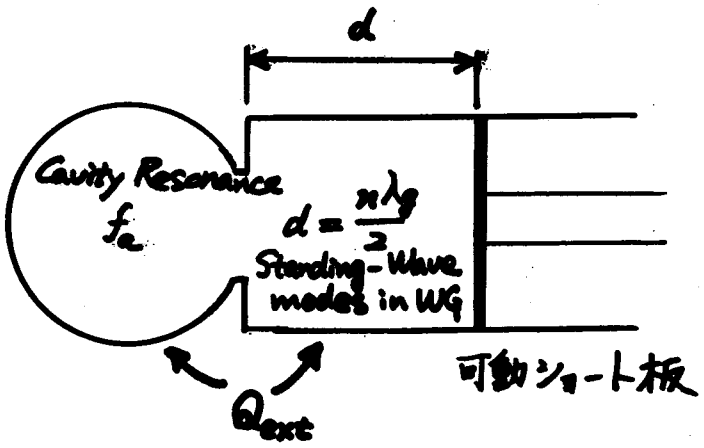

Fig. 2.8. Slater's tuning curve theory deals with a cavity coupled with a waveguide terminated with a movable short-circuiting plane.

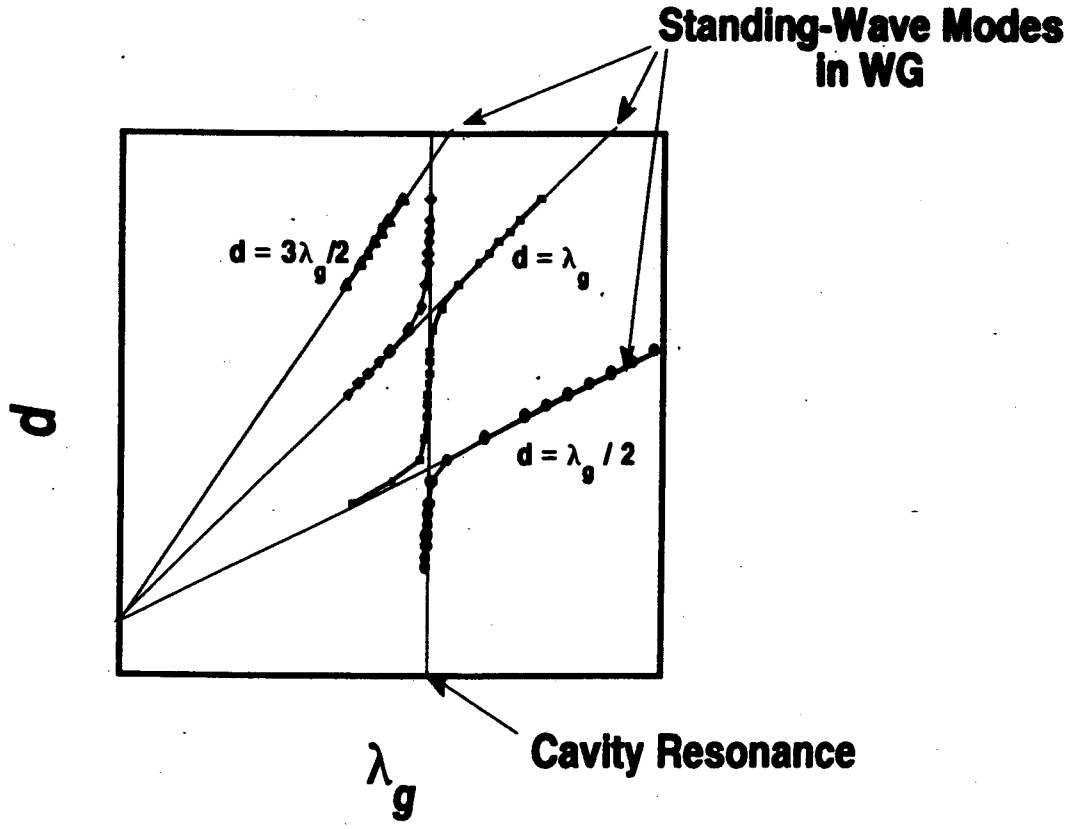

Fig. 2.9. An example of tuning curve response.

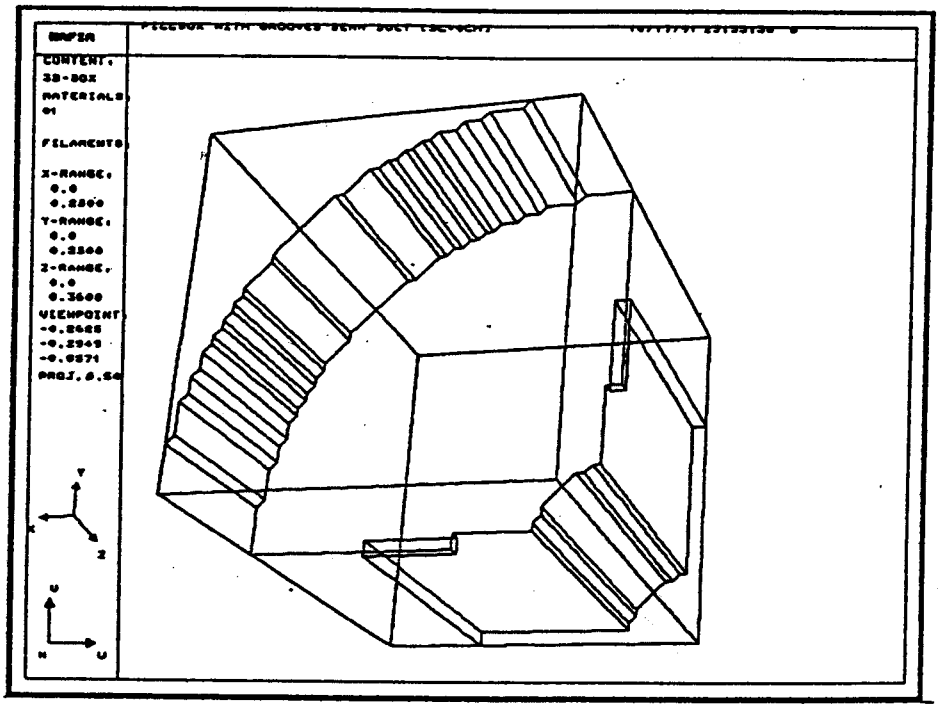

Fig. 2.10. The 3D geometry implemented to MAFIA to compute the tuning curve for the pillbox cavity loaded with the grooved beam pipe.

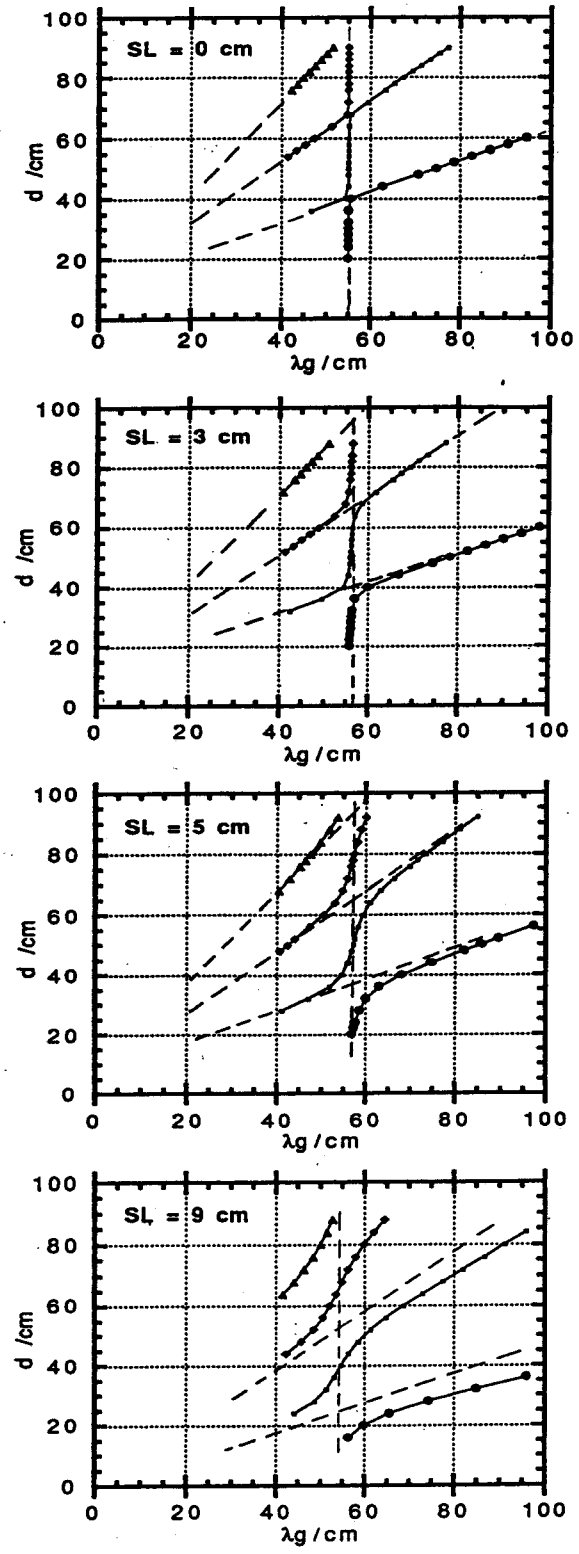

Fig. 2.11. Tuning curve responses obtained with MAFIA for the slit lengths SL = 0, 3, 5 and 9 cm.

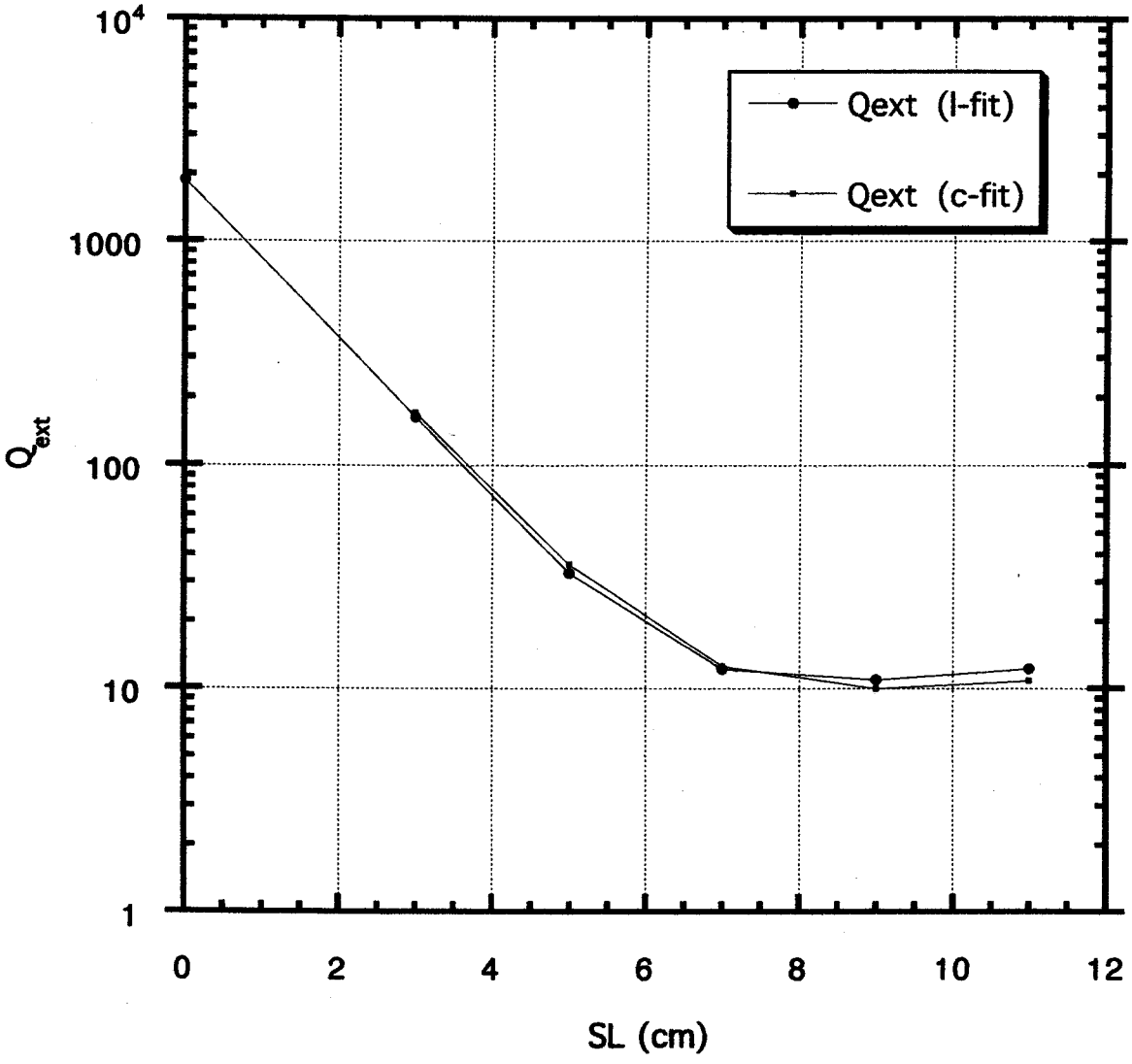

Fig. 2.12. The external Q values obtained with MAFIA are plotted as a function of the slit length SL.

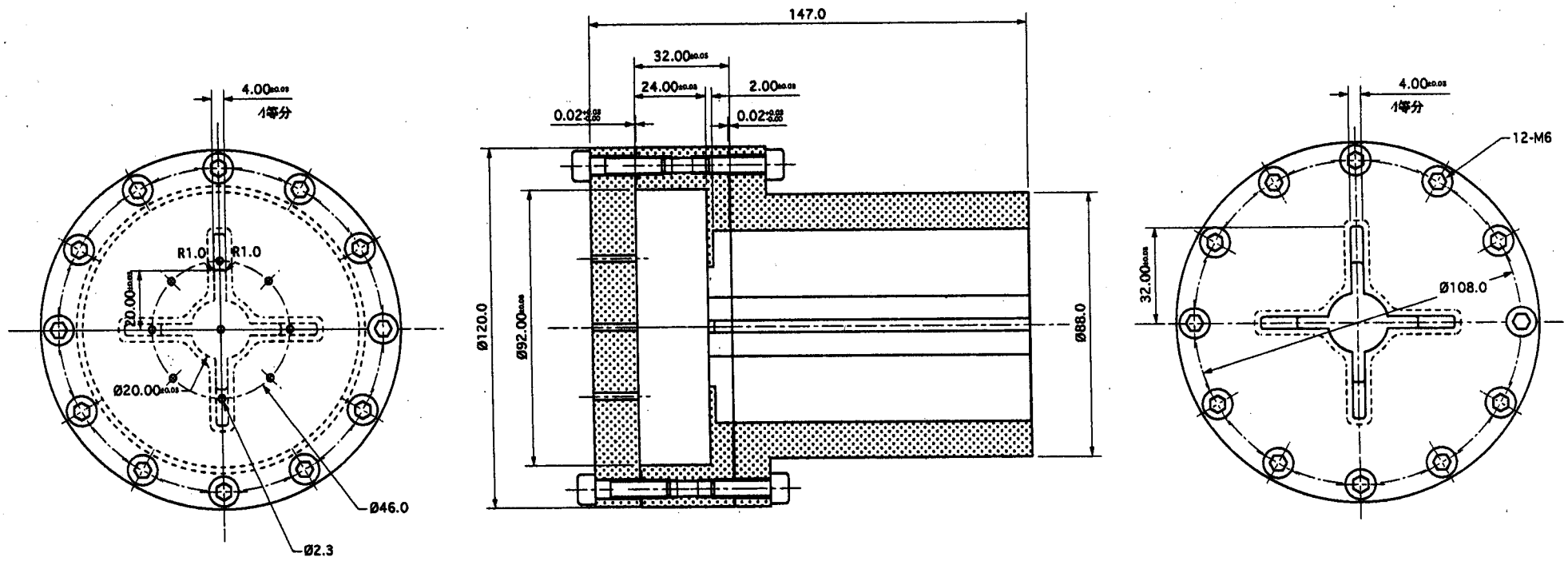

Fig. 2.13. A schematic drawing of the 20%-scale model cavity.

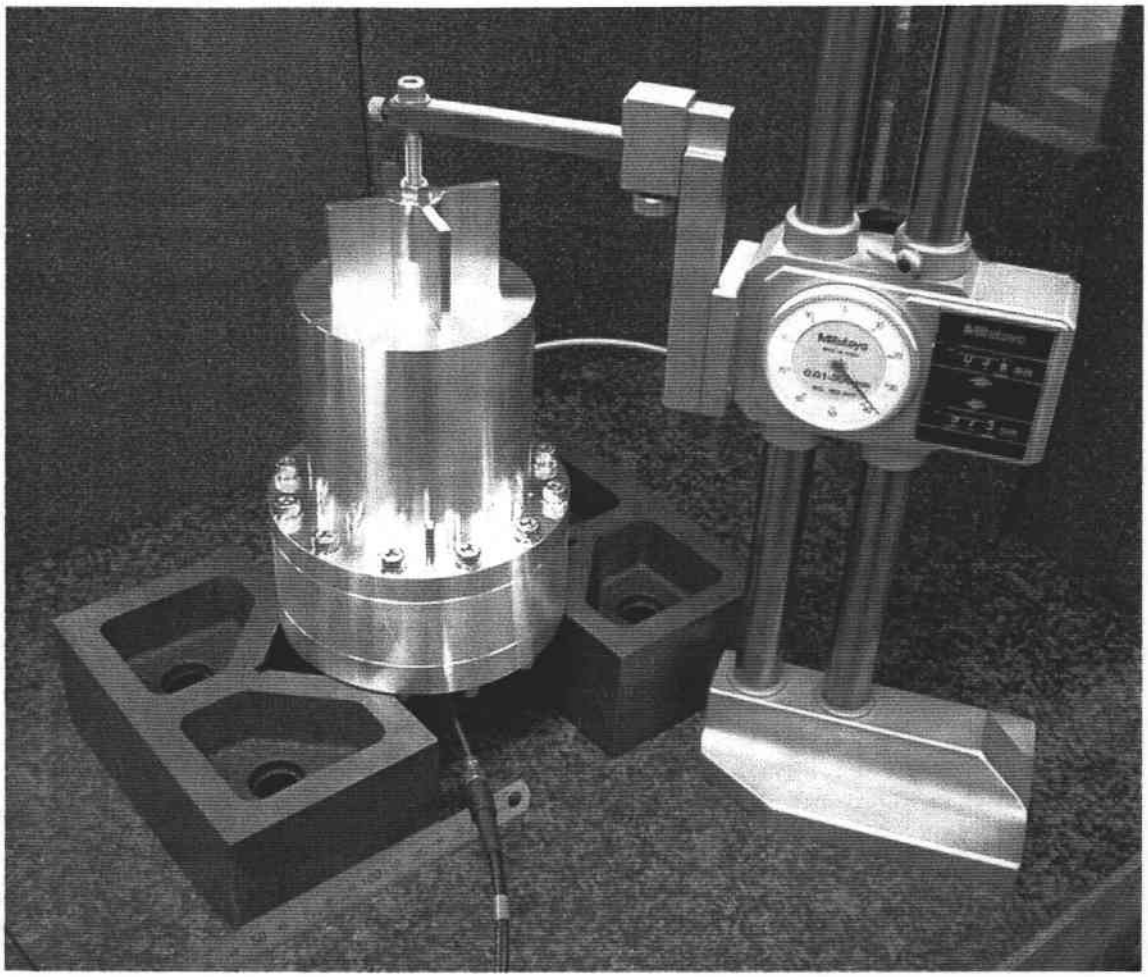

Fig. 2.14. Experimental set-up for cold model measurements based on Slater's tuning curve method.

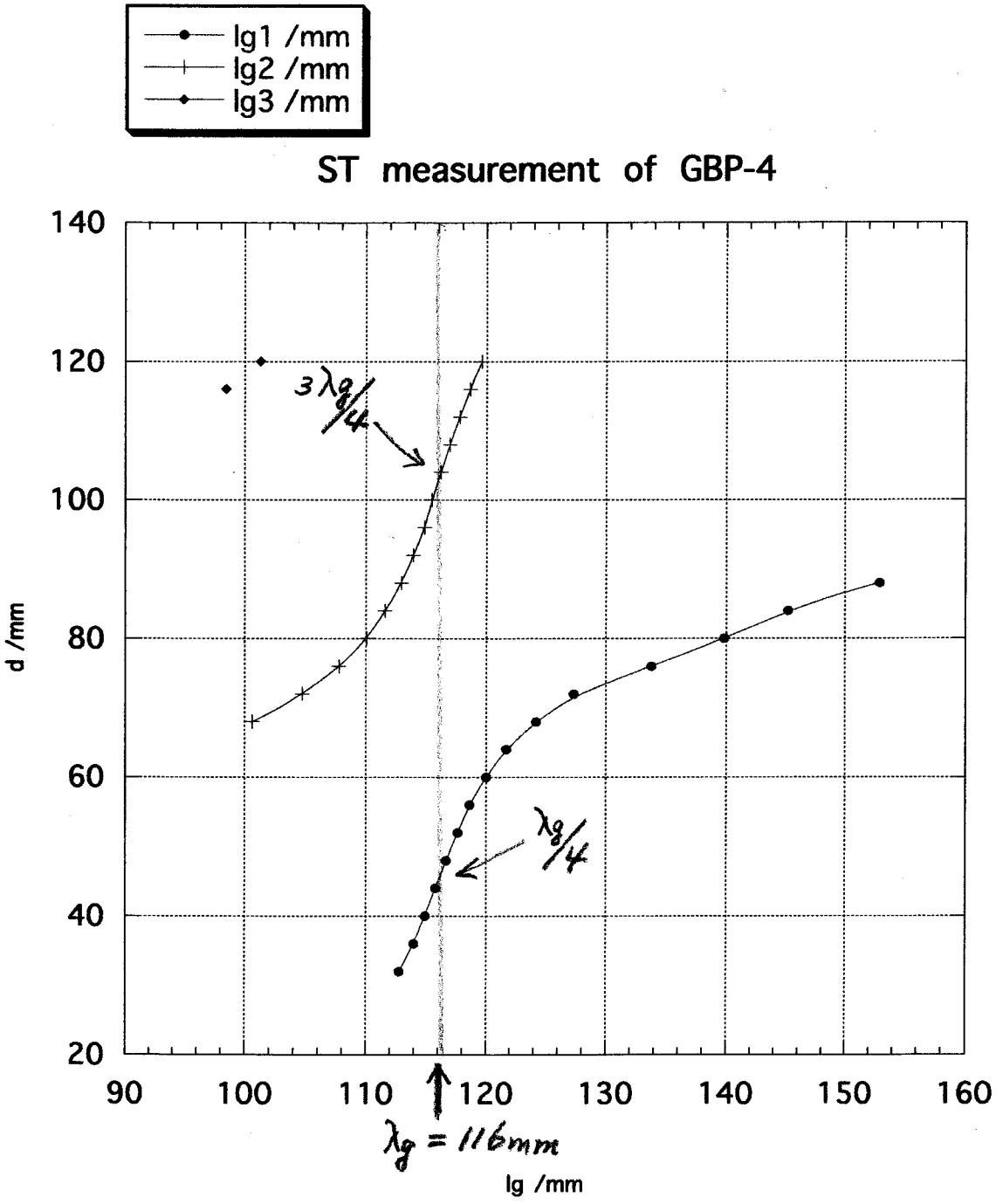

Fig. 2.15. Tuning curve response obtained from measurements for the model cavity.

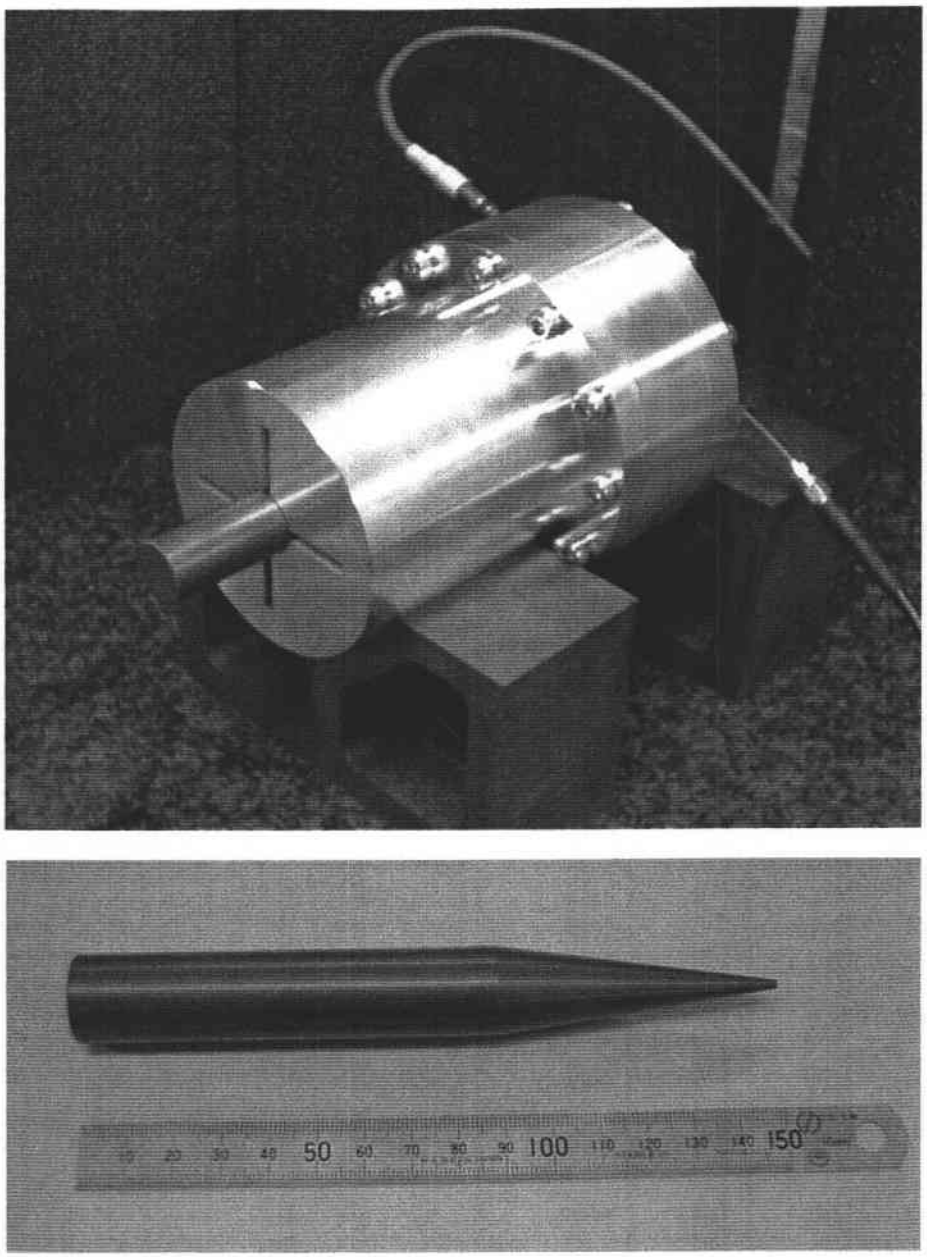

Fig. 2.16. Experimental set-up for cold model measurements with SiC load.

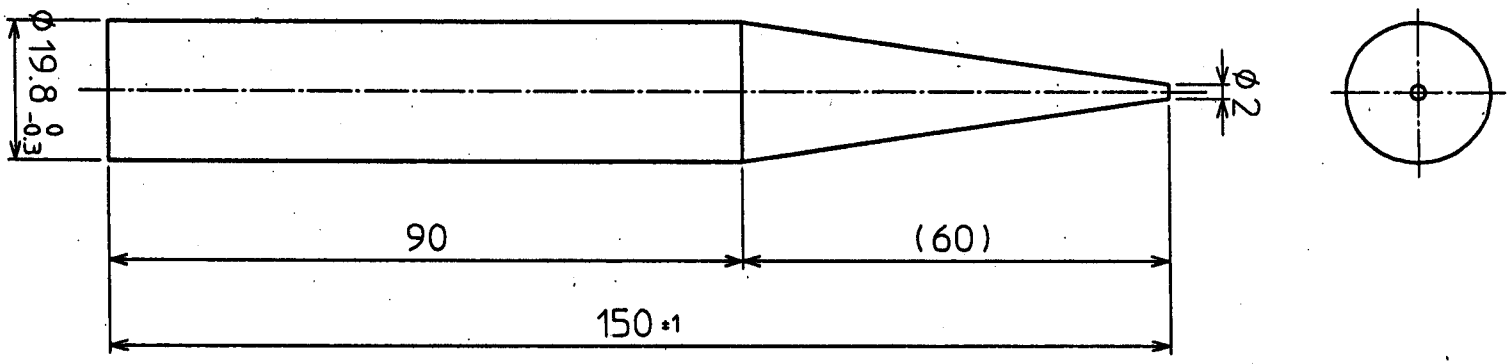

Fig. 2.17. A schematic drawing of a bullet-shape SiC load used to terminate the grooved beam pipe.

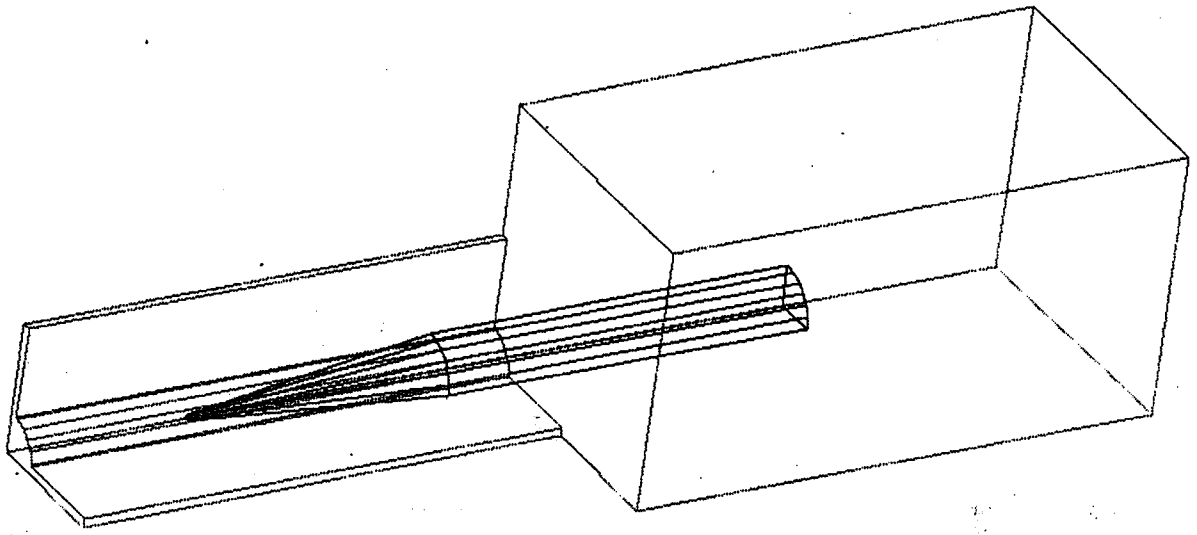

Fig. 2.18. A three-dimensional geometry for HFSS to simulate the performance of the bullet-shape SiC load inserted from the end of the grooved beam pipe.

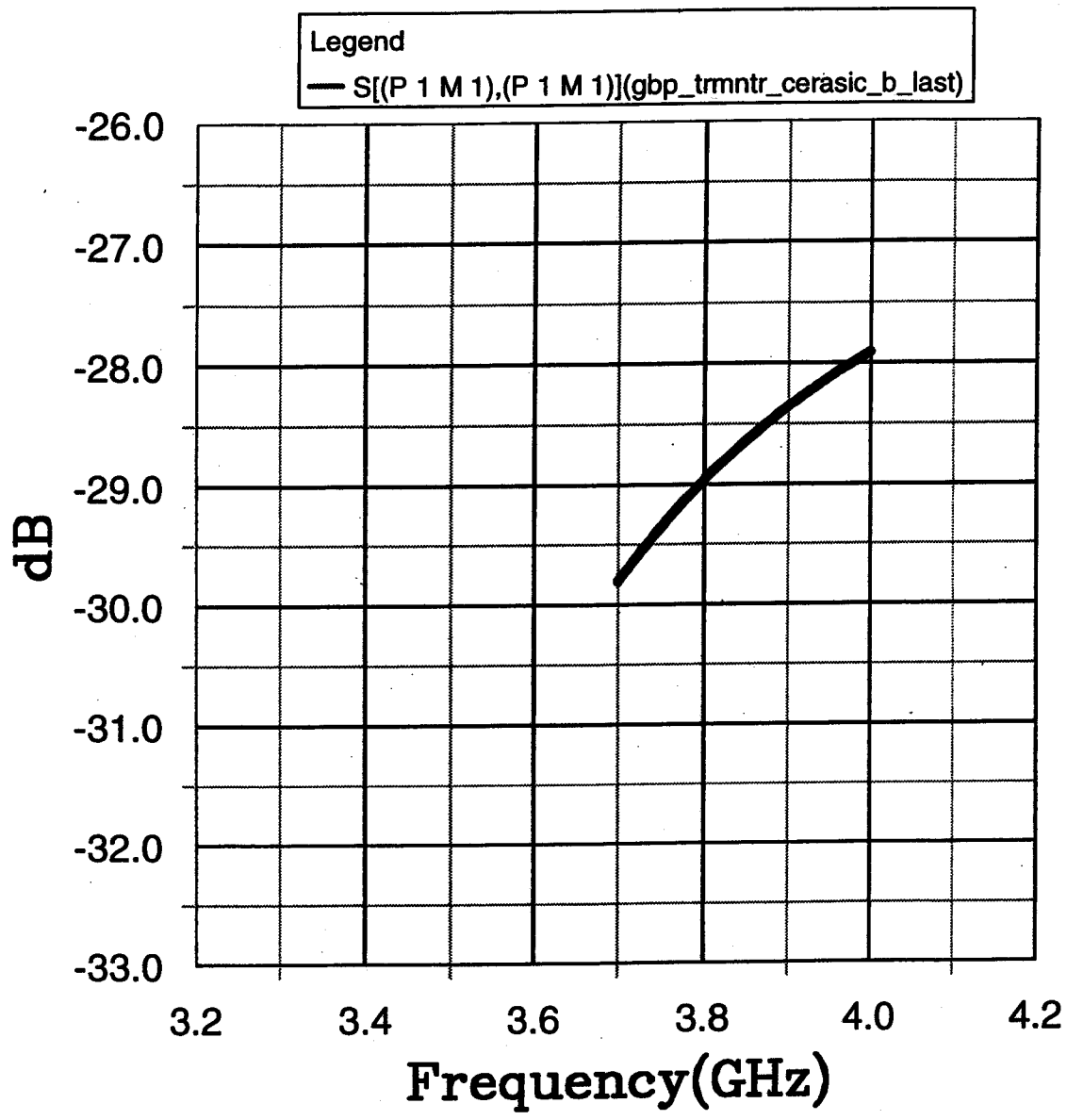

Fig. 2.19. The return loss of the bullet-shape SiC load obtained with HFSS, plotted as a function of frequency.

Chapter 3.
ARES CAVTY SYSTEM

3.1. Overview

Coupled-Bunch Instability due to the Accelerating Mode

The operation of conventional normal conducting cavities under heavy beam loading conditions would give rise to another serious instability problem other than the HOM-driven instabilities. That is the longitudinal coupled bunch instability due to the accelerating mode itself, which is usually optimized to have a large coupling impedance to the beam. Needless to say, we are not allowed to damp the accelerating mode.

In storage rings, the resonant frequency of the accelerating mode is usually detuned toward the lower side from the RF frequency in order to compensate for the reactive component of the beam loading and minimize the input RF power. Without this detuning, a large amount of RF power is reflected from the cavity. The amount of detuning frequency for optimum operation is given by

$$\Delta f = -\frac{I\sin\phi_s}{2V_c} \times \frac{R}{Q_0} \times f_{RF} = -\frac{P_b \tan\phi_s}{4\pi U}, \qquad (3.1)$$

where I is the beam current, ϕ_s the synchronous phase, V_c the voltage per cavity, R the shunt impedance, Q_0 the unloaded Q value, f_{RF} the RF frequency, P_b the beam power and U the stored energy. That is basically similar to forced oscillation mechanics with two external driving forces out of phase. In the case of a cavity with beam loading, the first driving force is the RF power from the generator (klystron) and the second is the beam-induced power.

If a high beam current is stored in a large storage ring like KEKB, the detuning frequency required for a conventional normal conducting cavity becomes comparable to, or even exceed the beam revolution frequency f_{rev}. Then, the coupling impedance of the accelerating mode at the upper synchrotron sidebands of the revolution harmonic

frequencies f becomes significantly high, where f is given by

$$f = f_{rev}(h + m + \nu_s), \quad m = -1,-2,\ldots \quad , \tag{3.2}$$

where h is the harmonic number, m the mode number of the coupled-bunch oscillation, ν_s the synchrotron tune. For example, loaded with the design beam current of 2.6 A in the KEKB LER, the detuning frequency of a normal conducting cavity with R/Q = ~200 Ω and V_c = 0.4 ~ 0.6 MV would be -200 ~ -300 kHz, about 2 to 3 times the revolution frequency f_{rev} = 99.4 kHz. In this situation, several modes of the longitudinal coupled-bunch instability would be strongly excited with a growth time on the order of 100 μs, much faster than the radiation damping time of 20 ms.

Increasing Stored Energy over Beam Loading

The simplest way to avoid this kind of instability is to decrease the detuning frequency. In the workshop on the KEKB accelerator design, held in July 1991, Funakoshi [25] first pointed out that a cavity structure with a smaller R/Q is preferable and should be extensively studied. According to Eq. (3.1), that is equivalent to increasing the ratio of the stored energy to the beam loading.

In order to reduce R/Q by an order of magnitude, Shintake [26] proposed two schemes with use of a cylindrical energy storage cavity operated in the high-Q TE015 mode. One scheme is a two-cavity system in which an accelerating cavity is directly coupled with a storage cavity like the LEP normal conducting accelerating structure with a spherical storage cavity [27]. The other is a more complicated one in which two accelerating cavities are coupled with two storage cavities via a four-port 3-dB coupler like the SLED hybrid system [28]. However, either scheme is inconclusive to present no clear solution even to the following fundamental problems with coupled-cavity system operated under heavy beam loading conditions:

- The first problem is how to do well both in adjusting the ratio between the electromagnetic energy in the storage cavity and that in the accelerating cavity, and

in keeping this energy ratio stably in amplitude and phase under heavy beam loading conditions.

- The second problem is how to cure the beam instability due to the parasitic mode(s) inevitably brought by the coupled cavity scheme. Needless to say, the cure should not reduce the impedance of the accelerating mode. However, this selective cure may not be easy because the accelerating mode can be a parasitic mode and vice versa when the viewpoint is changed.

Thus, how to couple the accelerating cavity to an energy storage cavity under heavy beam loading conditions is a matter of great significance, which needs to be solved first in the conceptual design, even from scratch.

Three-Cavity System ARES operated in the π/2 Mode

The first feasible conceptual design satisfying the fundamental requirements stated above is a three-cavity system proposed by Yamazaki and Kageyama [29]. That is a coupled cavity system operated in the π/2 mode, in which an accelerating cavity is resonantly coupled with a cylindrical TE015-mode storage cavity via a coupling cavity between, as illustrated in Fig. 2.1. Additionally, the coupling cavity is equipped with a parasitic mode damper against the 0 and π modes, which emerge at both sides of the π/2 accelerating mode. This coupled cavity system was later named ARES, which is the acronym for Accelerator Resonantly coupled with Energy Storage. The resonant coupling in the π/2-mode enables the following key design features of the ARES cavity system:

- The stored energy ratio $U_a : U_s$, where U_a is the stored energy in the accelerating cavity and U_s in the storage cavity, can be easily adjusted by changing the coupling factor ratio $k_a : k_s$, where k_a is the coupling factor between the accelerating and coupling cavities, and k_s between the storage and coupling cavities.

- The π/2 mode is stable against tuning errors and heavy beam loading conditions. In the ARES cavity system, only the accelerating cavity with beam loading needs to be detuned for optimum operation. When detuning the accelerating cavity by Δf_a, the amount of detuning frequency $\Delta f_{\pi/2}$ for the π/2 accelerating mode can be reduced as

$$\Delta f_{\pi/2} = \frac{U_a \Delta f_a}{U_a + U_s} . \tag{3.3}$$

- The parasitic 0 and π modes can be selectively damped with an antenna-type coupler to the coupling cavity.

- Furthermore, the damped 0 and π modes are located nearly symmetrically with respect to the π/2 mode. Therefore, these impedance contributions to beam instabilities can be counterbalanced.

- The coupling cavity functions as a filter to isolate the storage cavity from the HOMs of the accelerating cavity.

Development History of ARES

The first conceptual design [29] presented with an equivalent lumped circuit model was followed by a computer-aided design study [30] with use of the three-dimensional electromagnetic code MAFIA. The dimensions of the cylindrical TE015-mode storage cavity were carefully optimized to avoid the reduction in the Q value of the TE015 mode caused by opening an aperture to the coupling cavity. The presence of a coupling aperture, which breaks the cylindrical symmetry, may mix low-Q parasitic modes into the TE015 mode and deteriorate its high Q value. Later, a more realistic design using a TE013-mode storage cavity with a reduced length was adopted [31]. That was just a compromise with the available space in the KEKB tunnel.

Needless to say, the accelerating cavity itself of the ARES cavity system is required to be a HOM-damped structure. Two conceptual demonstrators with different HOM-damped structures were developed: the first prototype ARES95 [32] with a quadrupole counter mixing (QCM) choke structure [12], (see Fig. 3.2); and the second prototype ARES96 [7] with four rectangular HOM waveguides at the upper and lower sides of the accelerating cell and with two grooved beam pipes (see Fig. 3.3). Both prototypes were demonstrated through a series of high-power tests and high-current beam experiments carried out in the TRISTAN accumulation ring (AR) in 1996 [7, 33, 34].

Finally, ARES96 was chosen as the production prototype for KEKB. Major reasons are as follows:

- ARES96 has shown better performance in thermal structural stability during high-power operation. Actually, ARES96 was successfully operated beyond 250% of the design wall power dissipation of 150 kW while ARES95 could not be operated above 120% due to abnormal vacuum pressure rise. That could be caused by thermal deformation of the coaxial structure with an inner conductor supported like a cantilever.

- The mirror symmetry of ARES96 with respect to the beam direction allows better HOM damping performance especially above the beam pipe cutoff. That is because both beam pipes can be used to extract the HOM power.

- Confining the accelerating mode by the waveguide cutoff may be safer than choking it during long-term high-current operation with bunch patterns having a gap of vacant buckets for beam abort. Bunch patterns with a gap strongly excite the parasitic 0 and π modes at both sides of the $\pi/2$ accelerating mode.

3.2. Fundamental RF Characteristics

Figure 3.3 shows a schematic drawing of the ARES cavity system developed and

currently operated for KEKB. Its design is based on a conceptual demonstrator named ARES96 [7].

After successfully demonstrated in the TRISTAN accumulation ring (AR), a series of stringent high-power tests of ARES96 were further continued in the accelerator tunnel, with sufficient shields against x rays from the cavity operated with high gradients, in order to verify the long-term reliability as a production prototype. Major RF parameters related to the fundamental mode are listed in Table 3.1, together with records achieved in those high power tests. The ratio of the electromagnetic energy stored in the energy storage cavity to that in the accelerating cavity was set at $U_s : U_a$ = 9 : 1. According to Eq. (3.3), the amount of detuning frequency for the $\pi/2$ accelerating mode is reduced by a factor of 10. The design cavity voltage is 0.5 MV, generated with a wall power dissipation of 150 kW in total, 60 kW in the accelerating cavity and 90 kW in the storage cavity.

Table 3.1. Major RF parameters of the ARES cavity system and the high-power test records achieved with the conceptual demonstrator ARES96 in TRISTAN AR.

f_{RF}	=	508.887 MHz
$U_a : U_s$	=	1 : 9
R/Q	=	15 Ω
Q	=	1.1×10^5 †

P_c = 150 kW per ARES Cavity generating

V_c = 0.5 MV (KEKB Design)

High-Power Performance (ARES96)

Maximum continuous: P_c = 380 kW

Maximum for 20 minutes: P_c = 450 kW

†: in high-power operation with P_c = 150 kW

Storage Cavity and Input Coupler

The energy storage cavity operated in the TE013 mode is a large cylindrical steel structure with an inside diameter of 1070.4 mm and an axial length of 1191.1 mm. Major parts are a steel cylinder and two steel end plates, whose inner wall surfaces are electroplated with copper in a dedicated copper-pyrophosphate bath. After electroplating, the two end plates and the cylindrical part are assembled and sealed with TIG welding along the circumference of each joint, where a good electric contact is also obtained by stress due to welding shrinkage. With those fabrication techniques, sufficient RF properties were obtained together with excellent mechanical properties of steel. In the case of ARES96's storage cavity, it has been shown that the Q value of 168000 can be achieved for the TE013 mode, which is 86.6% of the theoretical value of 194000 in the case where a cylindrical symmetric cavity structure without a coupling hole for the $\pi/2$-mode operation or accessory ports is assumed together with the electric conductivity of International Annealed Copper Standard $\sigma(100\%\ \mathrm{IACS}) = 5.79\times10^{7}\ (\Omega\cdot\mathrm{m})^{-1}$. Additionally, fundamental studies, stated below in detail, on the cavity fabrication techniques have shown that the reduction in the Q value is mainly due to surface imperfections of the electroplated copper and the effect of the $\pi/2$-mode coupling hole is less than 1%.

The performance of the electroplated copper was investigated in advance using a full-scale model cavity fabricated for low-power and vacuum tests. As shown in Fig. 3.4, the model cavity has two pumping ports with screen grids and two circular ports at the cylindrical side of the middle level, but does not have a coupling aperture for the $\pi/2$-mode operation. The Q values of major modes were measured and compared with the theoretical values calculated with MAFIA, assuming the electric conductivity of $\sigma(100\%\ \mathrm{IACS})$. Figure 3.5 shows the measured-to-theoretical ratios plotted as a function of frequency. The ratio decreases monotonically from 92.9% for the TM010 mode at 210 MHz, to 86.8% for the TE013 mode at 510 MHz. This monotonic behavior can be explained simply by the relation between the thickness of the surface imperfection layer and the skin depth, where the former is constant but the latter scales as $f^{-1/2}$, from ~5 μm at 200 MHz to ~3 μm at 500 MHz. Moreover, it should be noted

that this monotonic behavior, over the TM010 mode with radial and longitudinal wall currents and a family of TE01n modes with circular wall currents only, indicates a good electric contact obtained at the joint of the end plate and the cylindrical part. Additionally, a slight enhancement observed for the TE012 mode is due to its magnetic field pattern with a node at the middle level with the two circular ports. In case of the TE011 or TE013 modes, the wall currents are disturbed by the circular port apertures.

Let us return to details of the storage cavity shown in Fig. 3.3. Each of the upper and lower end plates has a mode-shifting groove, with a radial gap of 70.0 mm and a depth of 40.5 mm, at the outermost circumference in order to resolve the degeneracy of the TE013 and TM113 modes. For thermal detuning compensation, a movable tuning plunger with a diameter of 200 mm and a travel of 60 mm is installed in the central port of the upper end plate. On the other hand, at the lower end plate, a fixed tuner is installed to adjust the origin of the fundamental mode frequency without the movable tuner.

For the $\pi/2$-mode resonant operation with the accelerating cavity via the coupling cavity, a rectangular aperture, with 120 mm in width and 180 mm in height, is opened at the cylindrical side of the middle level. The coupling cavity is bolted to the storage cavity at the rectangular flange joint there, where thin stainless-steel sleeves are to be TIG welded for vacuum seal at a final phase in commissioning. In the case of high-power testing above the ground or operation in early commissioning periods, a viton (fluorocarbon elastomer) gasket is temporarily used instead. That is because the storage and accelerating cavities need to be separately moved into the KEKB tunnel for installation. Other accessory ports at the cylindrical side of the storage cavity are as follows: four pumping ports, with screen grids against intense RF fields, used for a turbo molecular pump, two ion pumps, and a manifold for vacuum gauges; and three drive ports at the middle level, actually one of which is equipped with an input coupler.

The RF power driving the ARES cavity system is fed through an input coupler attached to the storage cavity. Two types of input couplers with different coaxial window matching structures were developed [35]: the over- and under-cut type and the choke type, shown in Fig. 3.6. The RF power is guided from the rectangular waveguide

(WR1500), transformed at a doorknob transition with a capacitive iris at the entrance, through a coaxial matching structure with a coaxial ceramic disk window of 99.5% pure alumina, further tapered down to a coaxial line (WX77D), finally to a coupling loop at the end. The coupling factor is set to 2.7 for the anticipated operation in KEKB, and can be adjusted from 0 to 4 by rotating the loop if necessary. Both types were successfully tested up to 950 kW at a dedicated test stand with a 1-MW dummy load, far above the design power capability 400 kW. Out of the three drive ports of the storage cavity, the port facing the rectangular coupling aperture toward the accelerating cavity is never used in the regular operation, so as to protect the window ceramic from the direct path of ions produced by the beam in the accelerating cavity.

Coupling Cavity equipped with Parasitic Mode Damper

The function of the coupling cavity is a keystone if the ARES cavity system is compared to a stone arch. The coupling cavity is made of machined OFC (Oxygen Free Copper) parts brazed in a vacuum furnace, and integrated into the accelerating cavity structure at one side in the final brazing, together with a half-cell coupling cavity for the $\pi/2$-mode termination at the other side as shown in Fig. 3.3. Each coupling cavity is coupled to the accelerating cavity through a rectangular aperture with a width of 120 mm and a height of 160 mm. This aperture size was determined, in relation with the coupling aperture of the storage cavity, so as to give the design ratio of the stored energies $U_s : U_a = 9 : 1$. The half-cell coupling cavity exactly counterbalances the coupling cavity for the $\pi/2$ accelerating mode, to restore the mirror symmetry of the accelerating field with respect to the mid vertical plane.

The coupling cavity is equipped with a parasitic mode coupler [36], which is an antenna-type coupler as shown in Fig. 3.7, in order to damp the 0 and π modes. Both modes can be damped down to about two times Q_c, where Q_c is the loaded Q value of the coupling cavity and almost equal to the external Q value to the coupler. The external Q value can be adjusted from 30 to 100 by changing the antenna insertion. The extracted RF power is guided through a coaxial line (WX120D) followed by a matching section with a coaxial ceramic disk window of 99.5% pure alumina, through a cross

stub support where the direction is changed downward to the exit. The window matching structure is similar to that of the over- and under-cut type for the input coupler. The coaxial line is further extended downward from the exit, tapered down (WX120D-WX77D), and matched to the flange of a dummy load at the end. The dummy load is a water-cooled type with a power capability of 40 kW.

Figure 3.8 shows the damped 0 and π modes measured in ARES96 with $Q_c = 55$, together with the central sharp peak of the $\pi/2$ mode. The 0 and π modes are well damped down to $Q_L \approx 100$, and also located almost symmetrically with respect to the $\pi/2$ mode by adjusting the insertion of an additional tuning plunger with a diameter of 90 mm from the upper port of the coupling cavity. This graph allows us to conclude that the fundamental RF characteristics of the ARES cavity system have been successfully demonstrated in the low-power test.

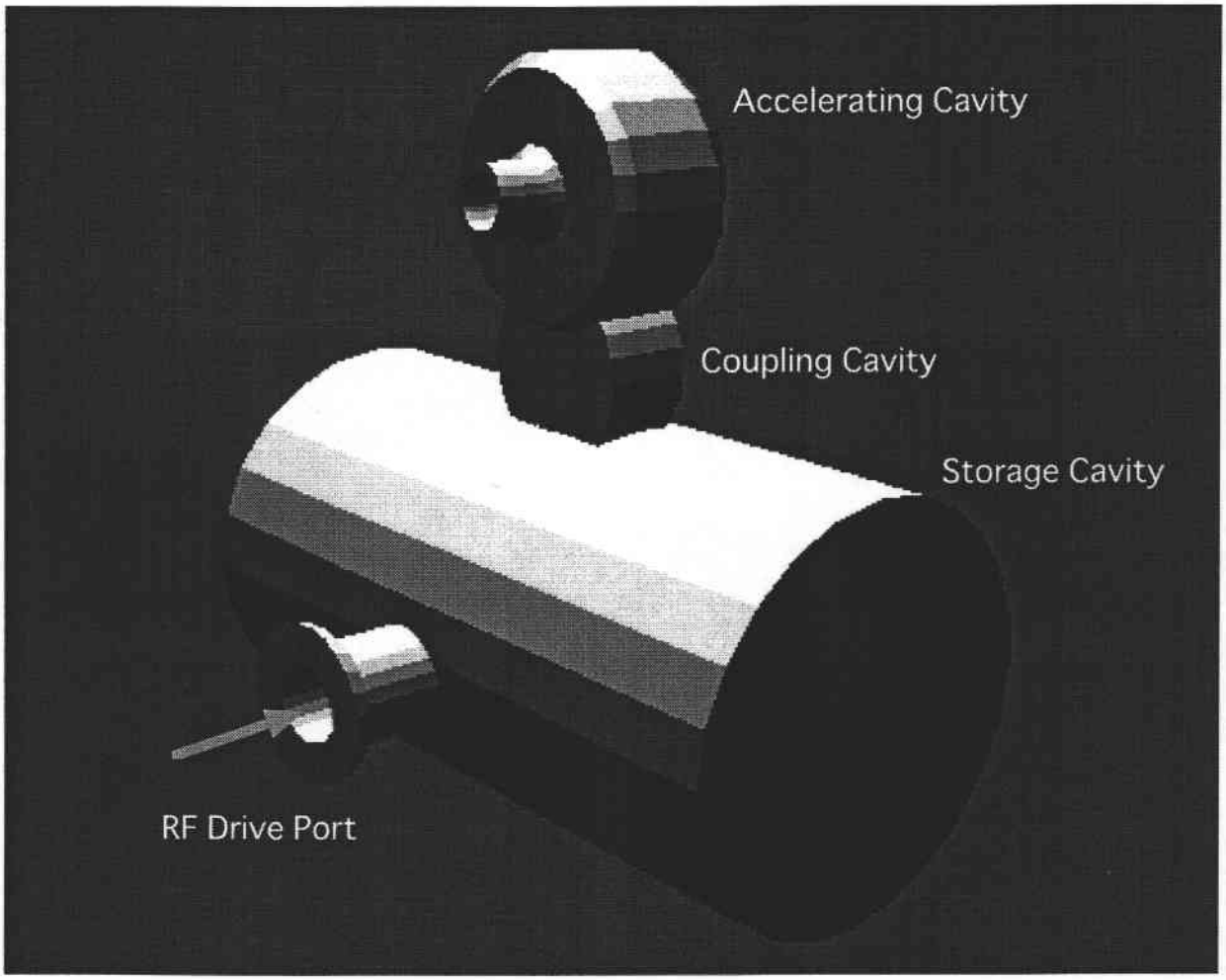

Fig. 3.1. Three-Cavity System ARES.

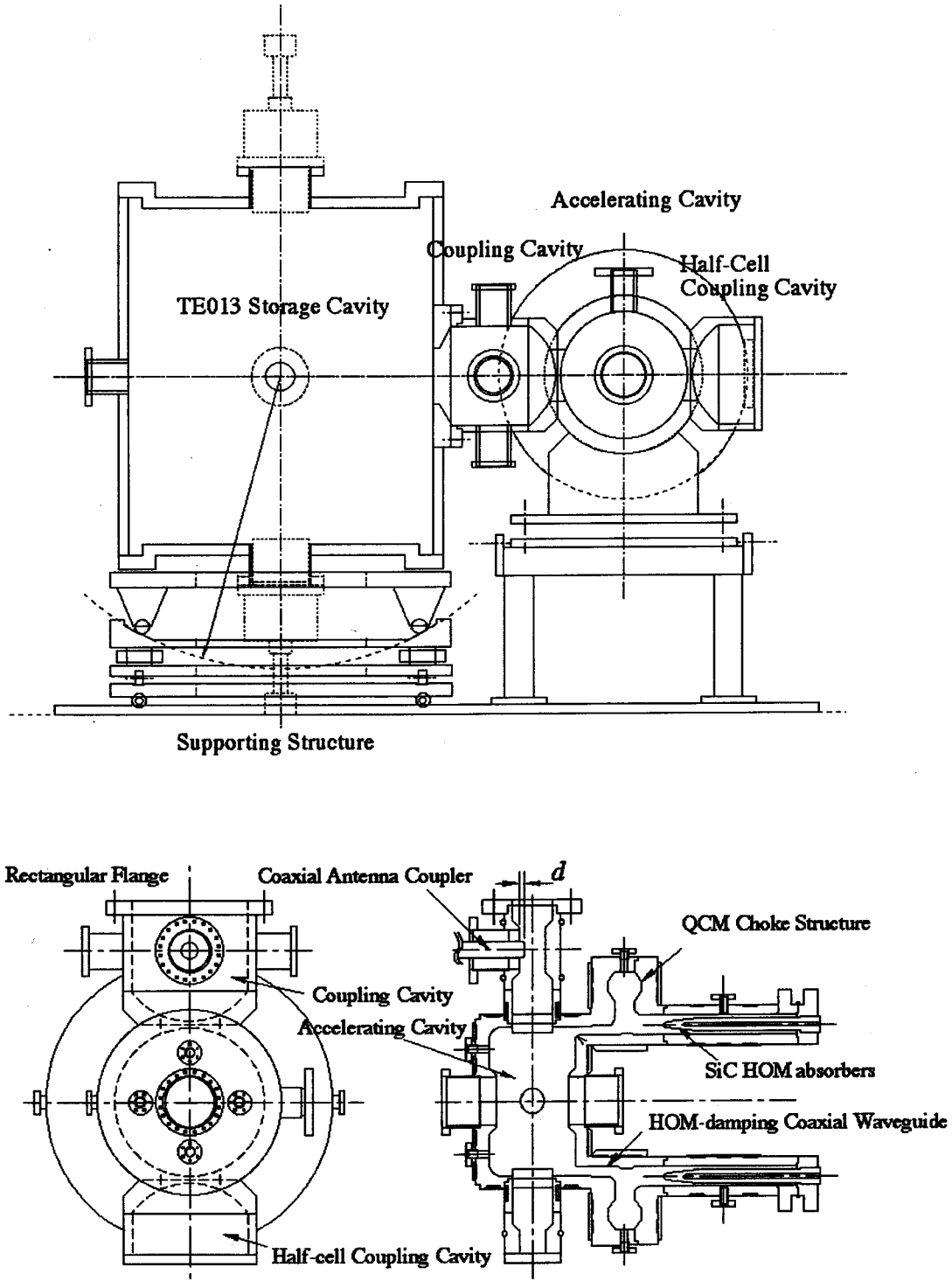

Fig. 3.2. ARES95 with a Quadrupole Counter Mixing (QCM) Structure.

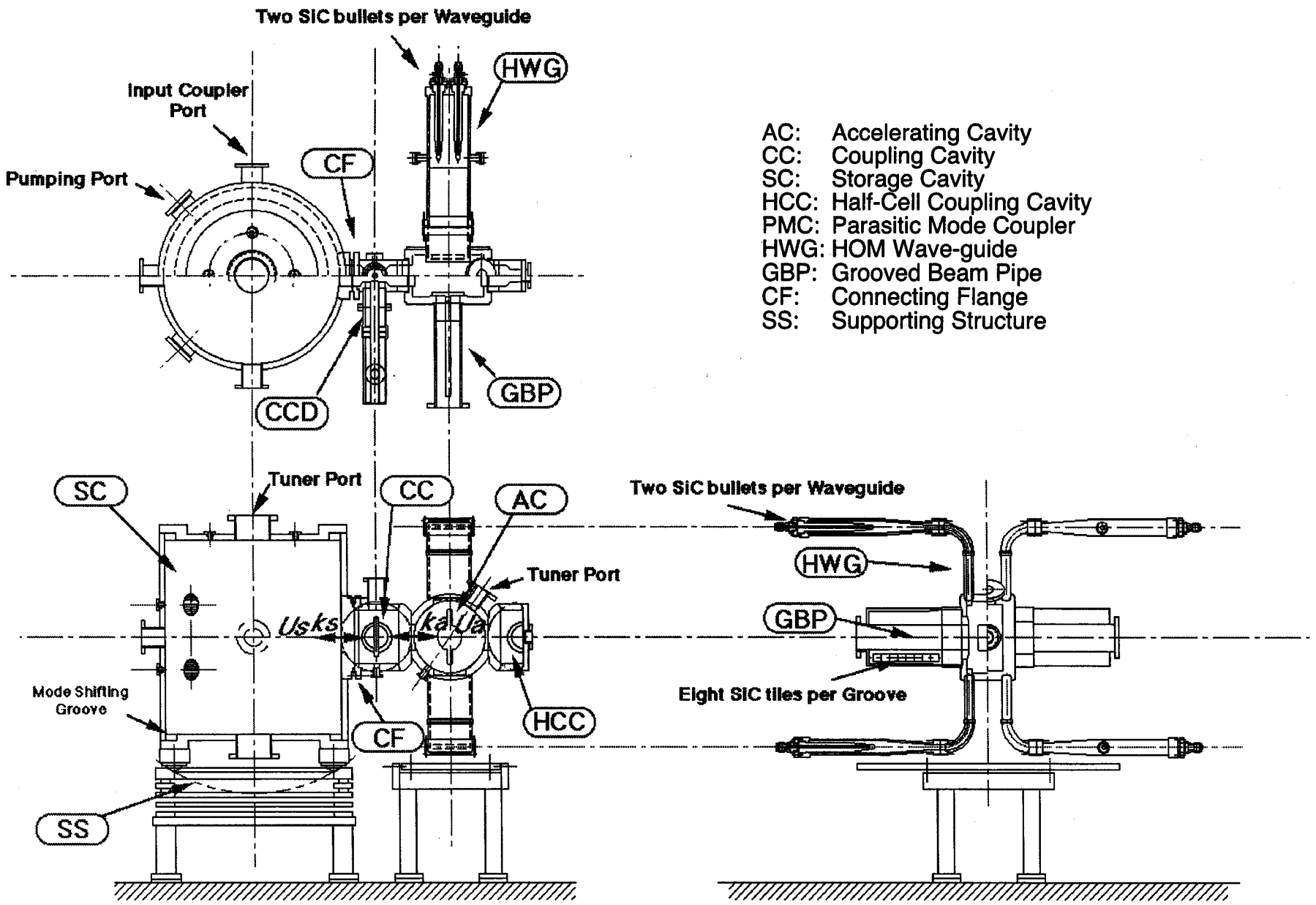

Fig. 3.3. ARES96 with Grooved Beam Pipes

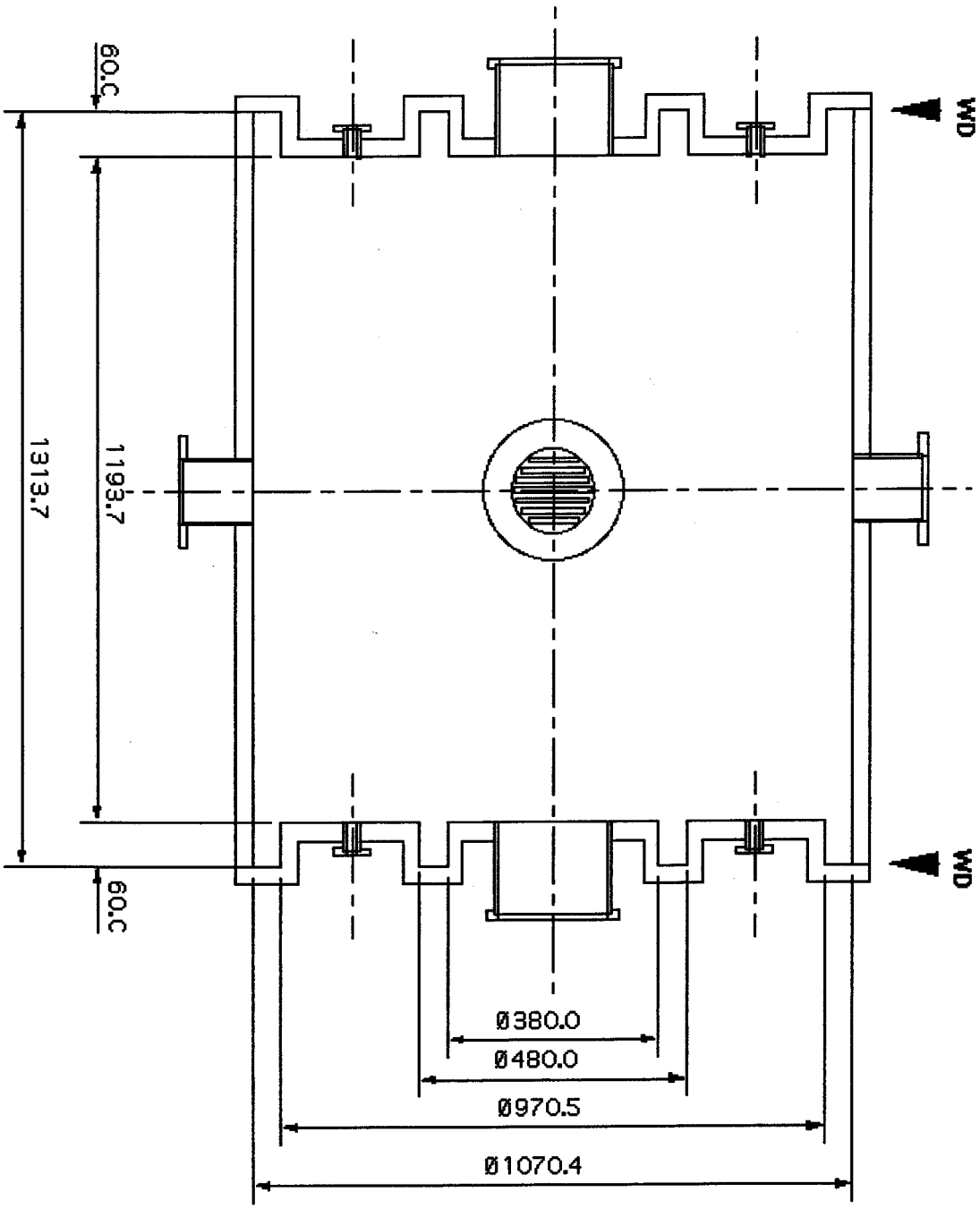

Fig. 3.4. Storage Cavity for Low-Power and Vacuum Tests.

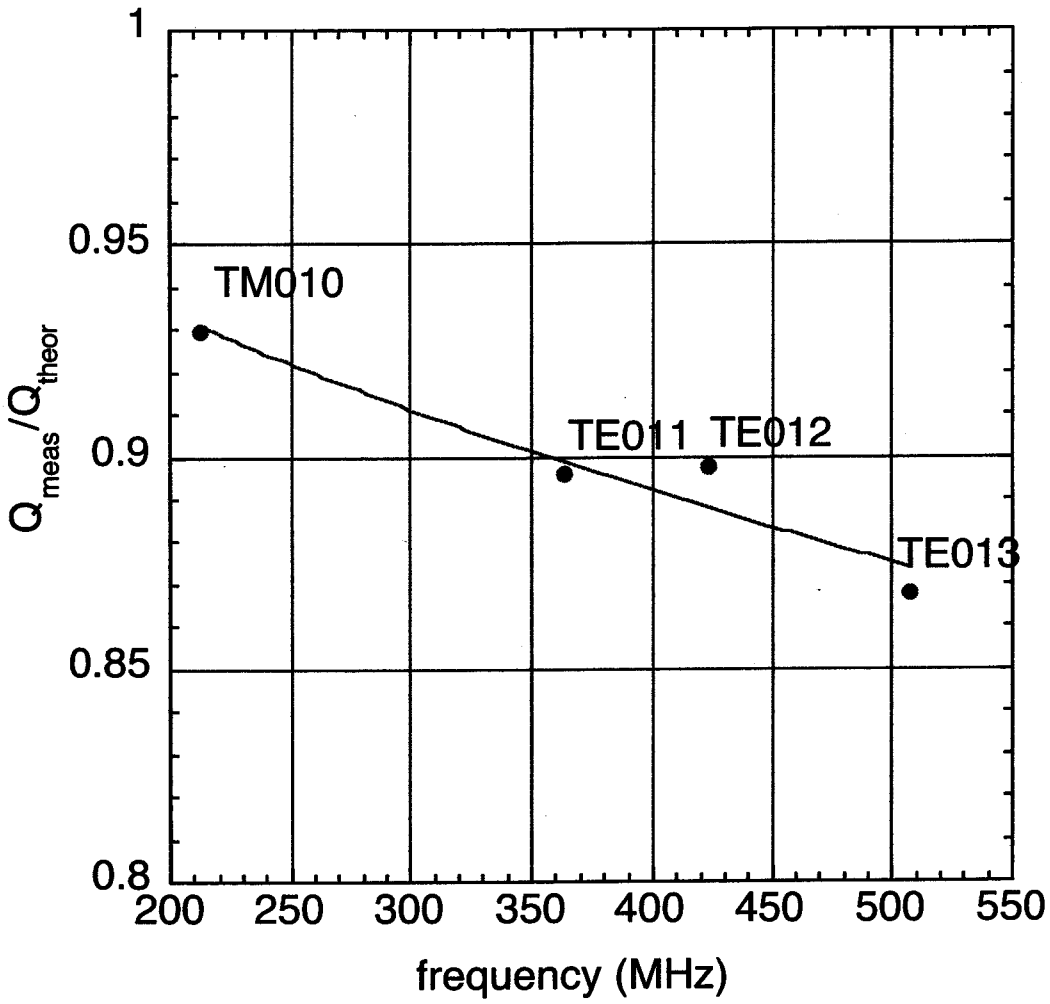

Fig. 3.5. The ratio of the measured and theoretical Q values are plotted as a function of frequency for major modes in the low-power storage cavity.

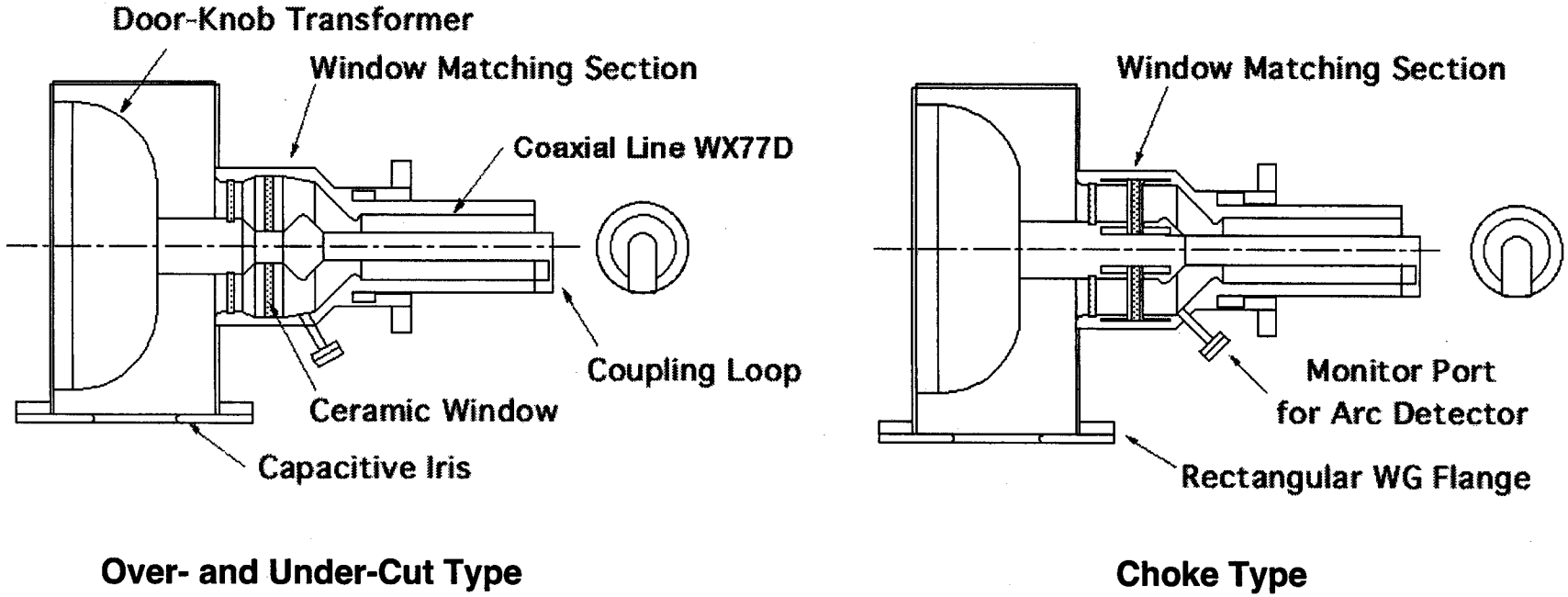

Fig. 3.6. Two types of input couplers with different window matching structures.

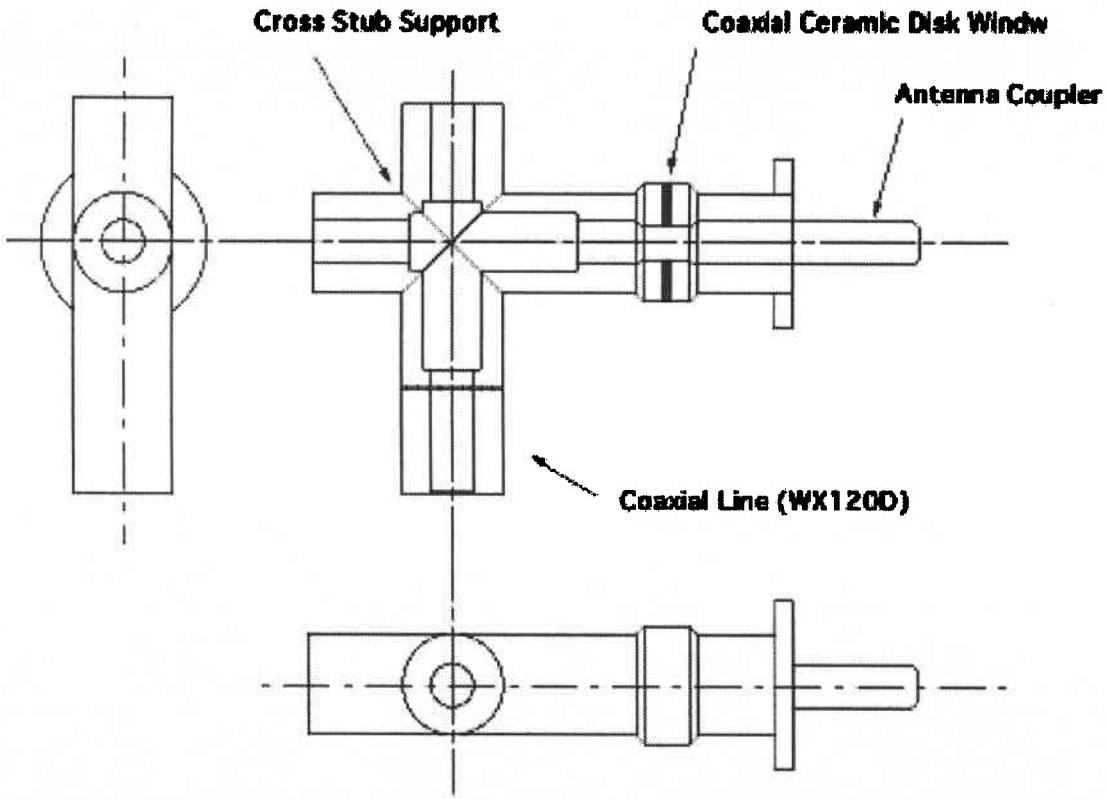

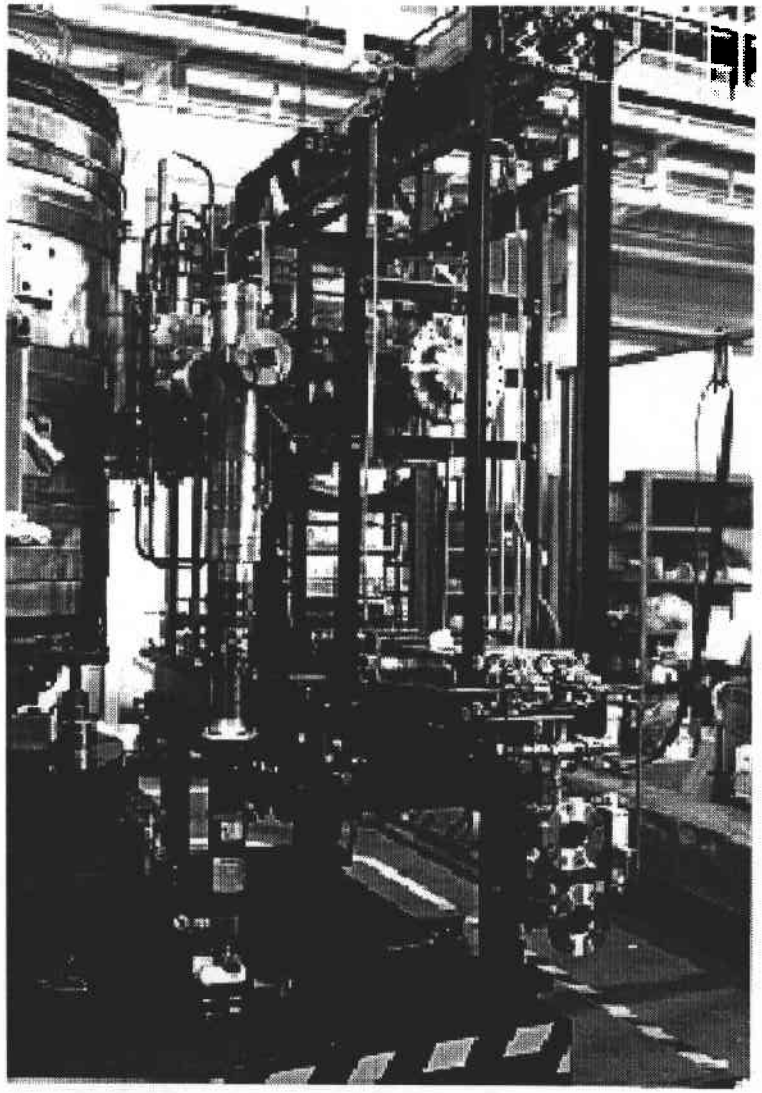

Fig. 3.7. Parasitic Mode Coupler

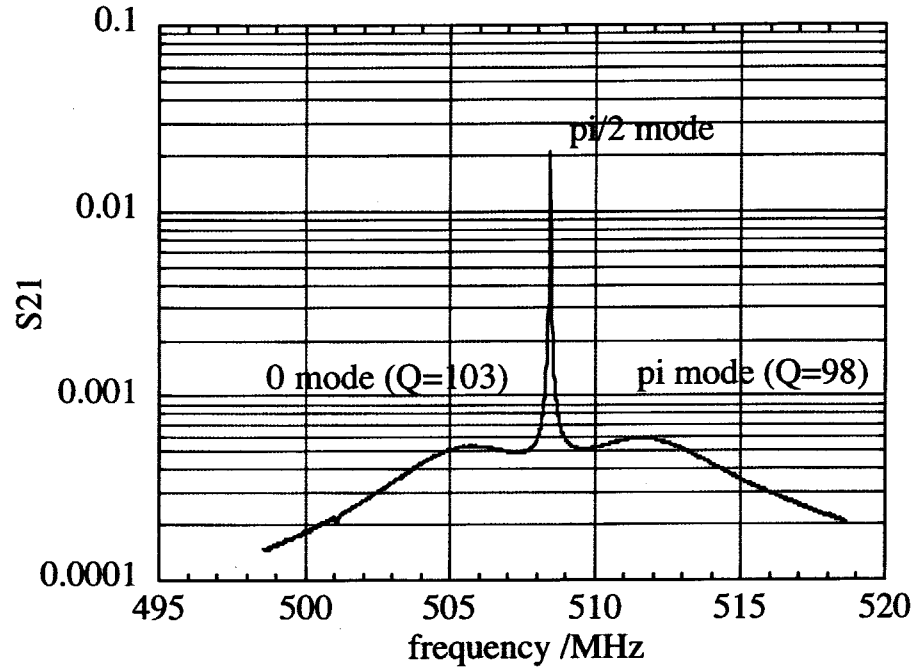

Fig. 3.8. The π/2 accelerating mode and the damped parasitic 0 and π modes when $Q_c \sim 55$.

Chapter 4.
HOM-DAMPED STRUCTURE FOR ARES CAVITY SYSTEM

4.1. Design Criteria

In the ARES cavity system, the accelerating cavity itself needs to be a HOM-damped structure in order to suppress the coupled-bunch instabilities due to HOMs. Furthermore, the adopted HOM-damped structure needs to be structurally compatible with the ARES cavity system. That is a boundary condition, i.e. two rectangular coupling apertures at both sides of the accelerating cavity: one to the coupling cavity, and the other to the half-cell coupling cavity for the $\pi/2$-mode termination keeping the accelerating field symmetrical with respect to the mid plane. This boundary condition already breaks the rotational degeneracy for dipole modes. In other words, the degenerated frequencies of the horizontal and vertical polarizations splits into two levels due to the presence of the coupling apertures at both sides, where "horizontal" and "vertical" mean deflecting the beam in the horizontal direction and in the vertical direction, respectively. Moreover, the exact counterbalancing by the half-cell coupling cavity is no longer valid for HOMs. This mirror asymmetry could mix monopole HOMs with a dipole component deflecting the beam in the horizontal direction. This problem becomes more serious at higher frequencies.

Thus, the HOM-damped structure needs to be carefully designed compatible with the boundary condition inherent in the ARES cavity system, without sacrificing its HOM damping performance. The design criteria for the HOM-damped structure for ARES96 are as follows:

- The structure for HOM damping needs to be invariant under mirror inversion with respect to each of the horizontal and vertical mid plane including the beam axis, so as to be naturally embedded into the ARES cavity system.

- Moreover, the structure with mirror symmetry with respect to the beam direction is

preferable. That is because both beam pipes can be equally used for HOM damping above the beam-pipe cutoff.

- Additionally, the inside diameter of the beam pipe needs to be increased as large as possible to lower the cutoff frequency of the TM01 mode, to ease the mirror-asymmetry problem related to the half-cell coupling cavity stated above.

4.2. Design Overview

Accelerating Cell Structure

The accelerating cell was designed as simple as possible from the viewpoint of thermal deformation in high-power operation so as to be structurally stable even with two rectangular apertures at both sides for the $\pi/2$-mode coupling. To optimize the cell shape in order to increase the R/Q values of the accelerating mode is no longer a matter of great significance for cavities operated under heavy beam loading conditions, especially for the accelerating cavity of the ARES cavity system. The final cell shape is like a pillbox cavity, as shown in Fig. 4.1, with 10-mm-high nosecones around the beam bores enlarged to an inside diameter of 150 mm. In order to compensate for thermal detuning, a movable tuning plunger, with a diameter of 70 mm and a travel of 60 mm, is inserted from the upper right port. This tuner configuration slightly breaks the mirror symmetry of the fundamental mode, which will be investigated later in relation with design of the groove beam pipe.

Rectangular HOM Waveguide

Four straight rectangular waveguides are directly brazed to the upper and lower sides of the accelerating cavity, as shown in Fig. 4.1, in order to damp the monopole HOMs, and also the dipole HOMs deflecting the beam in the vertical direction (abbreviated to V-dipole HOMs). The waveguide width was set to 240 mm, giving a cutoff frequency of 625 MHz for the dominant TE10 wave. At the entrance to the cavity, the waveguide width is reduced to 200 mm with an inductive iris. This allows sufficient coupling to the HOMs while minimizing the reduction in Q of the fundamental mode.

The HOM power extracted from the cavity is guided through each straight waveguide in the upward or downward direction, and through an E-bend waveguide where the direction changed in the horizontal direction, finally dissipated in two bullet-shape SiC ceramic absorbers inserted from the waveguide end. Each SiC absorber, with a diameter of 55 mm and a total length of 400 mm including a 100-mm nosecone, is directly cooled by water flowing through a circular bore inside, as shown in Fig. 4.2. The power capability was tested up to 3.3 kW per absorber at a dedicated test stand with a L-band CW klystron. The HOM absorbers developed for ARES96 were reported in Ref. [37].

Twofold Grooved Beam Pipe

In order to damp the dipole HOMs deflecting the beam in the horizontal direction (abbreviated to H-dipole HOMs), each of the beam pipes attached to both ends is longitudinally grooved at the upper and lower sides, as shown in Fig. 4.1, to lower the cutoff frequency of the TE11 wave for the original circular pipe with an inside diameter of 150 mm. That is a twofold grooved beam pipe. As described in the previous chapter, the grooved beam pipe method allows sufficient damping of the dipole HOMs while the reduction in the Q value of the fundamental mode is negligibly small. Moreover, the twofold grooved beam pipe for damping the H-dipole HOMs has almost no coupling to the other polarization i.e. the V-dipole HOMs. Therefore, we can optimize the damping performance with these twofold grooved beam pipes almost independently from the constraints of the four rectangular HOM waveguide.

The groove dimensions are 30 mm in width and 95 mm in depth, lowering the cutoff frequency of the TE11 wave down to 580 MHz. At the entrance to the accelerating cell, the groove depth is reduced to 55 mm with an inductive iris, so as to avoid the reduction in Q of the fundamental mode due to dipole-mode mixing caused by insertion of the tuning-plunger from the upper-right port. As described later in detail, the inductive iris functions as a mode shifter to keep the lowest TE112-like mode in the grooved beam pipe away from the fundamental mode, rather than to adjust the coupling.

In each groove, there are eight SiC tiles arranged in a line, where the extracted HOM power is dissipated. Each SiC tile is brazed to a water-cooled copper plate with a

copper compliant layer between, as shown in Fig. 4.3. The HOM load with eight SiC tiles per groove was tested up to 0.5 kW at the test stand with the L-band CW klystron mentioned above.

4.3. HOM-Damping Properties

The HOM damping properties of the accelerating structure for ARES96 was investigated by a time-domain simulation technique [38] with use of MAFIA-T3 code. Figure 4.4 shows the geometry implemented to the simulation where the z-axis is chosen in the beam direction, the x-axis in the horizontal direction to the coupling cavity, and the y-axis in the vertical direction. This is a half part of the accelerating cavity with two half-cell coupling cavities at both sides. Each half-cell coupling cavity is terminated with an electrically shorting plane to simulate the $\pi/2$-mode boundary condition. Mirror symmetry with respect to the vertical mid plane was necessarily assumed to save the number of mesh points, which was limited by the memory storage available for us. However, this approximation is probably justified for HOMs below the beam-pipe cutoff, by the fact that the circular beam aperture is enlarged to a diameter of 150 mm and comparable to the rectangular aperture (120 mm by 160 mm) to the coupling cavity. The boundary conditions at the exits of the rectangular waveguides are assumed so that a waveguide with the same cross section is to be infinitely extended beyond each boundary, as well as the beam pipes.

The simulation was carried out in the following steps:

1) The cavity structure is excited by passing a bunch with total charge of q at the speed of light c in the following different configurations:

- For the monopole modes: on the beam axis under the boundary conditions with magnetically short at the z-x and y-z planes,

- For the H-dipole modes: off the beam axis by a distance of Δx in the horizontal

direction under the boundary conditions with magnetically short at the z-x plane and electrically short at the y-z plane (equivalent to the excitation by a dipole moment of $2q\Delta x$),

- For the V-dipole modes: off the beam axis by a distance of Δy in the vertical direction under the boundary conditions with electrically short at the z-x plane and magnetically short at the y-z plane (equivalent to the excitation by a dipole moment of $2q\Delta y$).

2) In each case, the wake field is calculated and recorded in a long range behind the bunch. Here, the wake field is defined as the Lorentz force acting on a test particle with unit charge following the leading bunch in a distance s at the same velocity c. That is expressed as:

$$\mathbf{F}(s,t) = \mathbf{E}(z = ct - s, t) + c\mathbf{e}_z \times \mathbf{B}(z = ct - s, t), \tag{3.4}$$

where the test particle is assumed running on the beam axis. Then, the longitudinal wake potential is defined as:

$$W_z(s) = \frac{1}{q}\int_{-\infty}^{\infty} dz\, F_z(z,\, t = \frac{z+s}{c}), \tag{3.5}$$

and the transverse wake potential is defined as:

$$W_x(s) = \frac{1}{2q\Delta x}\int_{-\infty}^{\infty} dz\, F_x(z,\, t = \frac{z+s}{c}) \tag{3.6}$$

$$W_y(s) = \frac{1}{2q\Delta y}\int_{-\infty}^{\infty} dz\, F_y(z,\, t = \frac{z+s}{c}) \tag{3.7}$$

in the horizontal and vertical directions, respectively.

3) In each case, the coupling impedance is finally obtained by the Fourier transform of the wake potential as:

$$Z_{//}(\omega) = \int_{-\infty}^{\infty} \frac{ds}{c} W_z(s)\exp(i\frac{\omega}{c}s) \tag{3.8}$$

for the monopole modes,

$$Z_x(\omega) = \frac{1}{i}\int_{-\infty}^{\infty} \frac{ds}{c} W_x(s)\exp(i\frac{\omega}{c}s) \tag{3.9}$$

$$Z_y(\omega) \equiv \frac{1}{i}\int_{-\infty}^{\infty} \frac{ds}{c} W_y(s)\exp(i\frac{\omega}{c}s) \tag{3.10}$$

for the H- and V-dipole modes, respectively.

In this simulation technique, the frequency resolution is determined by the trace distance s behind the leading bunch. However, the trace distance is actually limited by the CPU time available within a project timetable, and sometimes technically limited by the instability problem due to a pileup of numerical noises over a long time period. Practically, the trace distance should be increased stepwise as checking carefully the growth of each peak in the impedance spectrum.

Figure 4.5 shows the traces of the longitudinal wake potential, calculated for the geometry shown in Fig. 4.4, in time ranges of $0 < s/c < 60$, 480, and 1920 ns, where the trace distance s is divided by the speed of light c. The dominance of the accelerating mode trapped in the cavity is clearly seen by the end of trace. Figure 4.6 shows the longitudinal impedance spectra up to 2 GHz, obtained from the Fourier transforms of the wake potentials up to trace distances s = 144 m, 288 m, and 576 m. The solid curve is the threshold impedance determined by the radiation damping time (τ = 23 ms) in the KEKB LER with wiggler magnets. The beam pipe cutoff for the TM01 mode is 1.53

GHz. As seen from these three spectra, all the broad peaks remain stationary far below the threshold. However, besides the accelerating mode, two peaks at 810 and 1390 MHz, indicated by C1 and C2, grow sharply as the trace distance is increased, showing the possibility of exceeding the threshold. Actually, these two sharp peaks were first observed in beam-based measurements in AR in 1996. Then, the trace distance was increased up to 576 m to improve the frequency resolution. According to other frequency-domain simulations with MAFIA, it was found that these modes are trapped modes in the coupling cavity. For each mode, greater part of the field energy is stored in the coupling cavity, where the mode C1 has a TM110-like field pattern and the mode C2 has a TE111-like pattern. Generally, this kind of trapped mode is difficult to damp heavily, but fortunately it has a very small R/Q value because the beam traverses the accelerating cavity only. Therefore, the trapped modes C1 and C2 are expected to have coupling impedances not so high in comparison with other broad peaks in Fig. 4.6, although both have very high Q values. Actually, the longitudinal coupling impedance of the mode C1 was estimated at 420 Ω, from R/Q = 0.2 Ω obtained by computation with MAFIA and Q_L = 4200 by low-power measurement.

Figure 4.7 shows the traces of the transverse wake potential $W_y(s)$ deflecting the beam in the vertical direction, computed in short and long time ranges of $0 < s/c < 60$, and $0 < s/c <$ 1920 ns. The range of the wake potential $W_y(s)$ behind the leading bunch is successfully reduced on the order of 10 m by damping the V-dipole HOMs with the four rectangular waveguides. Figure 4.8 shows the transverse coupling impedance spectra for the V-dipole HOMs, obtained from the Fourier transforms of the wake potentials $W_y(s)$ computed up to trace distances of s = 148 m and 576 m. The threshold impedance is 2.75 kΩ/m for the radiation damping (τ = 46 ms), and eased up to 12.7 kΩ/m for the damping rate > 100 s^{-1} of the transverse multi-bunch feedback system for the KEKB LER.

Figure 4.9 shows the traces of the transverse wake potential $W_x(s)$ deflecting the beam in the horizontal direction, computed in time ranges of $0 < s/c < 60$, and $0 < s/c <$ 1920 ns. Also in the case of H-dipole HOMs, the range of the wake potential $W_x(s)$ is successfully reduced on the order of 10 m by extracting the HOM power form the

accelerating cavity through the twofold grooved beam pipes at both ends. Figure 4.10 shows the transverse coupling impedance spectra for the H-dipole HOMs, obtained from the Fourier transforms of the wake potentials $W_x(s)$ computed up to trace distances of s = 144 m and 576 m.

The results of the time-domain simulations to investigate the overall performance of the HOM-damped structure for ARES96 are summarized as follows:

- It has been shown that almost all the monopole and V-dipole HOMs can be successfully damped with use of the four rectangular waveguides attached to the accelerating cavity at its upper and lower sides. In the longitudinal impedance spectrum, the two sharp peaks C1 and C2 grow in height as the trace distance is increased, but are not likely to exceed the threshold impedance. That is because both are trapped modes in the coupling cavity and have very small R/Q values, which cancel out their high Q values.

- It has been shown that the H-dipole HOMs can be successfully damped with use of the twofold grooved beam pipes attached to the accelerating cavity at both ends, although the geometry was simplified with infinitely long grooved beam pipes.

4.4. Grooved Beam Pipe loaded with HOM Absorbing Material

As described in the previous section, the geometry simplified with infinitely long grooved beam pipes was used in the time-domain simulation studies on the overall performance of the HOM-damped structure for ARES96. However, the actual grooved beam pipe has a finite length of about 570 mm and a circular beam pipe with an inside diameter of 150 mm is attached to the end. Moreover, eight SiC ceramic tiles are loaded in each groove for absorbing the HOM power. Thus, the actual structure is significantly different from the simplified geometry without SiC absorbers loaded in each groove. Therefore, it is necessary to investigate the HOM-damping performance, especially for

the H-dipole HOMs, with a more realistic geometry reflecting the actual grooved beam pipe structure.

Further time-domain simulation studies were carried out with new geometry shown in Fig. 4.11, focusing on the H-dipole HOMs to be damped with the twofold grooved beam pipes loaded with SiC absorbers. In each groove, eight SiC ceramic tiles arranged in a line is simulated with a lossy dielectric slab of 50 × 400 × 20 mm^3, to which dielectric constants of $\varepsilon_r = 22$ and $tan\delta = 1$ are assigned. A circular beam pipe with an inside diameter of 150 mm is attached to the end of each grooved beam pipe. The total axial length of the geometry is 1600 mm. From necessity for saving the total mesh points, the coupling cavity and the rectangular HOM waveguides are not included in the new geometry to reduce the transverse dimensions. Presumably, this omission has little effect on the HOM damping properties of the grooved beam pipe. That is because the twofold grooved beam pipe for damping the H-dipole HOMs has no coupling, i.e. orthogonal to the monopole HOMs or the V-dipole HOMs, as mentioned before.

The transverse coupling impedance spectrum for the H-dipole modes was computed in the same way as described in the previous section. The cavity structure is excited by passing a bunch off the beam axis in the horizontal direction under the boundary conditions of magnetically short at the z-x plane and electrically short at the y-z plane. Figure 4.12 shows the wake potential $W_x(s)$ computed up to the trace distance $s = 72$ m. The range of the wake potential is slightly longer than that in Fig. 4.9 for the simplified case with the infinitely long grooved beam pipes. Additionally, a beat modulation is observed along the envelope. Figure 4.13 shows the transverse coupling impedance spectrum obtained from the Fourier transform of the wake potential in Fig. 4.12. The number of HOMs below 1 GHz is approximately doubled in comparison with Fig. 4.10 for the simplified case. That is probably because the truncated grooved beam pipe functions as a resonator coupled to the accelerating cavity like the waveguide-loaded cavity system in Slater's tuning curve theory. The maximum impedance is about 7 kΩ/m at 630 MHz, higher by 40% compared with the maximum of about 5 kΩ/m for the simplified case, but fortunately still below the threshold impedance of 12.7 kΩ/m when the transverse multi-bunch feedback system for the LER in service.

Below the circular beam pipe cutoff of 1.17 GHz for the TE11 mode, the geometry in Fig. 4.11 can be viewed as the accelerating cavity coupled to low-Q resonators loaded with RF absorbers. From this viewpoint, frequency-domain simulation studies were also performed with use of the MAFIA eigenmode solver, to estimate the transverse impedances for the H-dipole HOMs independently from the time-domain simulation technique. Figure 4.14 shows the geometry implemented to the frequency-domain simulation, which is a half part of the geometry in Fig. 4.11, split at the mid plane of the accelerating cavity.

The frequency-domain simulation was carried out in the following steps:

- First, the resonant modes are computed for the loss-free case, where dielectric constants $\varepsilon_r = 22$ and $tan\delta = 0$ are assigned to the dielectric slab in the groove.

- Next, the Q values due to wall losses and transverse impedances are calculated from the computed mode fields.

- Finally, the Q values due to the dielectric loss in the slab are also calculated from the computed mode fields, where $tan\delta = 1$ is assigned to the dielectric slab.

The transverse impedances obtained from the frequency-domain simulation are listed in Table 4.1 together with the Q values, and also graphically shown by bars in Fig. 4.13. The HOM field patterns are shown in Fig. 4.15. The first and second HOMs at 545 MHz and 547 MHz are TE111-like and TE112-like modes, respectively. These resonant frequencies are lower than the grooved beam pipe cutoff of 580 MHz for the TE11 mode. That is due to the dielectric slab ($\varepsilon_r = 22$) loaded in the groove. As described later, the second mode needs to be kept away from the fundamental mode as far as possible so as to avoid the reduction in the Q value of the faundamental mode due to the mode mixing. The third HOM at 632 MHz is a TE113-like mode, with greater part of the field energy in the accelerating cavity, and gives the highest transverse impedance. The

impedance spectrum curve and bar graph are in fair agreement with each other. The frequency-domain simulation gives a lower transverse impedance for every HOM in Fig. 4.13 than the time-domain simulation. That is probably because the loss tangent $tan\delta$ = 1 is too large as perturbation to calculate the dielectric loss in the slab from the mode fields obtained for the loss-free case.

Table 4.1.

f (MHz)	R_T/Q (Ω/m)	Q_L (=$Q_{dielectric}$)	R_T (kΩ/m)
545	19.4	14	0.28
547	8.6	14	0.12
632	200	46	9.2
660	63.4	18	1.1
691	14.3	17	0.25
744	210	25	5.4
805	153	19	2.9
837	127	17	2.2
895	332	13	4.2
931	60.5	11	0.66
996	216	11	2.4

4.5. Effect on the Fundamental Mode under Mirror Symmetry Breakdown

As stated before, the tuning plunger inserted from the upper-right port of the accelerating cavity as shown in Fig. 4.1 breaks the mirror symmetry and mixes the fundamental mode with a H-dipole mode. If this dipole mode has a low Q value, breakdown in the mirror symmetry will reduce the Q value of the fundamental mode and cause the fundamental-mode heating of the SiC tiles. According to the field patterns of the H-dipole modes in Fig. 4.15, the TE112-like mode at 547 MHz is the nearest

dipole mode to be mixed into the fundamental mode, and unfortunately the Q value is only 14. Therefore, the TE112-like mode needs to be kept away from the fundamental mode as far as possible.

First, the inductive iris at the entrance to the accelerating cell, where the grooved depth is reduced from 95 mm to 55 mm, plays the most significant role to raise the TE112-like mode, rather than to adjust the coupling. Without this iris, the TE112-like mode would be lowered below the fundamental mode. Secondly, it is clear that the presence of the SiC tiles in the grooves lowers the frequency of the TE112-like mode below the grooved beam pipe cutoff of 580 MHz for the TE11 mode. In order to compensate for this effect, the grooved beam pipe structure was optimized as shown in Fig. 4.16, where the groove depth is tapered down from 95 mm to 85 mm. With this optimization, the resonant frequency of the TE112-like mode could be raised up to 575 MHz. The performance of HOM damping with this tapered groove structure was also investigated with the frequency-domain simulation technique. Figure 4.17 shows the transverse impedance spectrum for the tapered groove structure. Compared with the spectrum in Fig. 4.13, the HOM-damping performance of the tapered groove structure is almost the same as that of the straight groove structure.

For the case of tapered groove structure, the reduction in the Q value of the fundamental mode due to the dipole-mode mixing caused by insertion of a tuning plunger was studied with use of MAFIA. Figure 4.18 shows the model geometry implemented to MAFIA, where a tuning plunger with a diameter of 70 mm is inserted into the cavity cell in the horizontal direction. This is the worst configuration to break the mirror symmetry with respect to the vertical mid plane including the beam axis. The reduction in the Q value can be expressed as:

$$\frac{1}{Q_{eff}} = \frac{1}{Q_{wall}} + \frac{1}{Q_{SiC}}, \qquad (3.11)$$

where Q_{eff} is the effective Q value of the fundamental mode, Q_{wall} due to the wall losses, and Q_{SiC} due to the dielectric losses in the SiC tiles. In this simulation study, the electric

conductivity of copper $\sigma = 5.8 \times 10^7$ $(\Omega \cdot m)^{-1}$ was assumed for all the metal surfaces, and the dielectric constants $\varepsilon_r = 22$ and $tan\delta = 1$ for the SiC tiles.

The simulation results are listed in Table 4.2. In the worst model case with a tuner insertion of 50 mm in the horizontal direction, the reduction in the Q value is about 1%. However, the reduction by 1% means that the total dissipated power in the SiC tiles would amount to ~600 W in high-power operation to generate the design voltage of 0.5 MV. The power dissipation of ~150 W per groove is not so small, compared with the design power capability of 500 W per groove. In the actual case, fortunately the tuner insertion is to be about 15 mm in high-power operation in KEKB, and more fortunately the axis of the tuner port is 35° with respect to a vertical line. Then, according to Table 4.2, the reduction in the Q value is roughly estimated at $\sim 0.05\% = 0.16\% \times sin^2 35°$, with a power dissipation of ~8 W per groove. This power level is practically acceptable.

Table 4.2.

Tuner Insertion (mm)	Q_{wall}	Q_{SiC}	$(Q_{eff} - Q_{wall})/Q_{wall}$
0	4.24×10^4	3.54×10^{11}	–0.00%
30	4.16×10^4	1.31×10^7	–0.32%
50	4.08×10^4	4.15×10^6	–0.97%

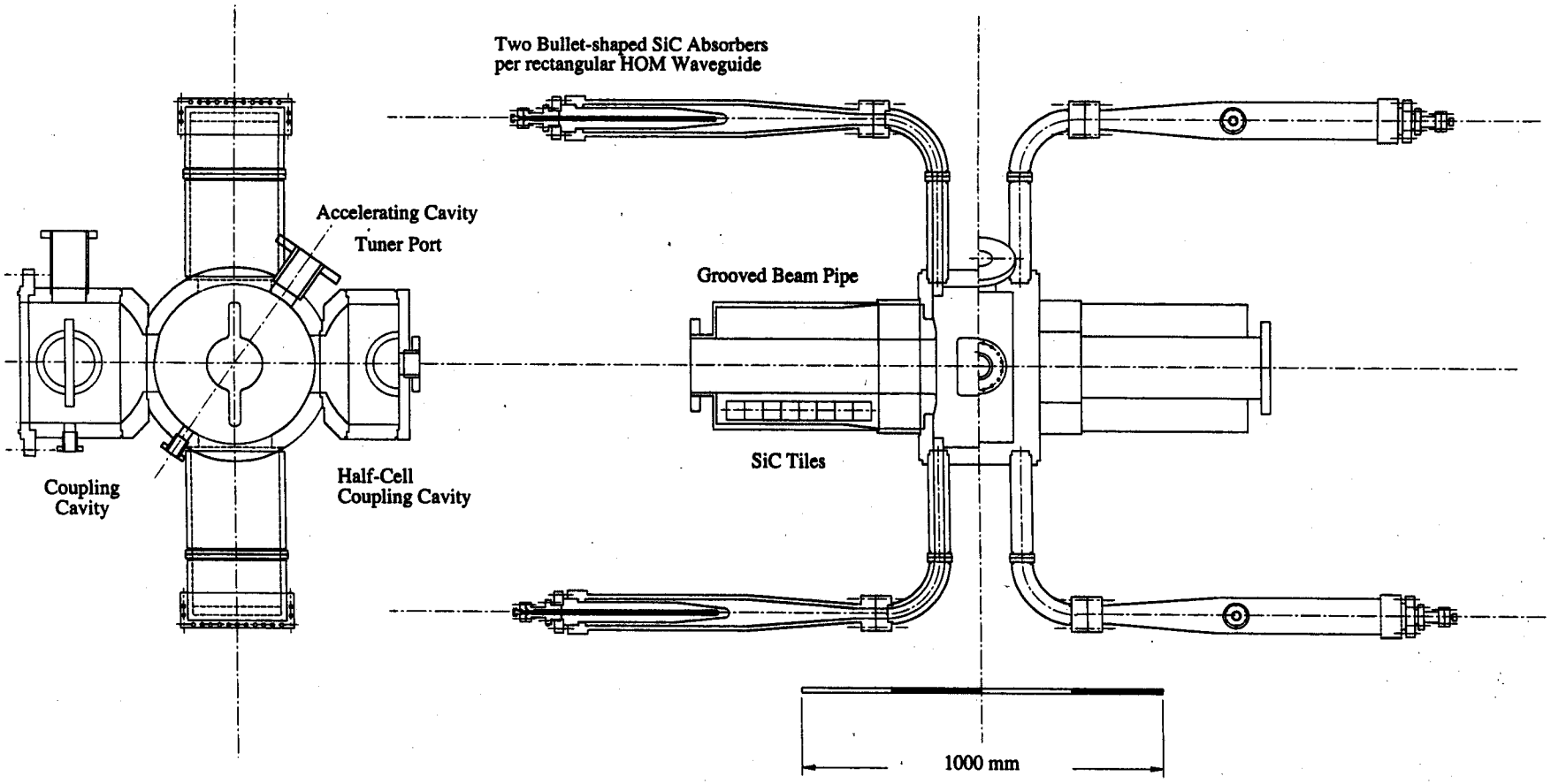

Fig. 4.1. HOM-damped structure for ARES96

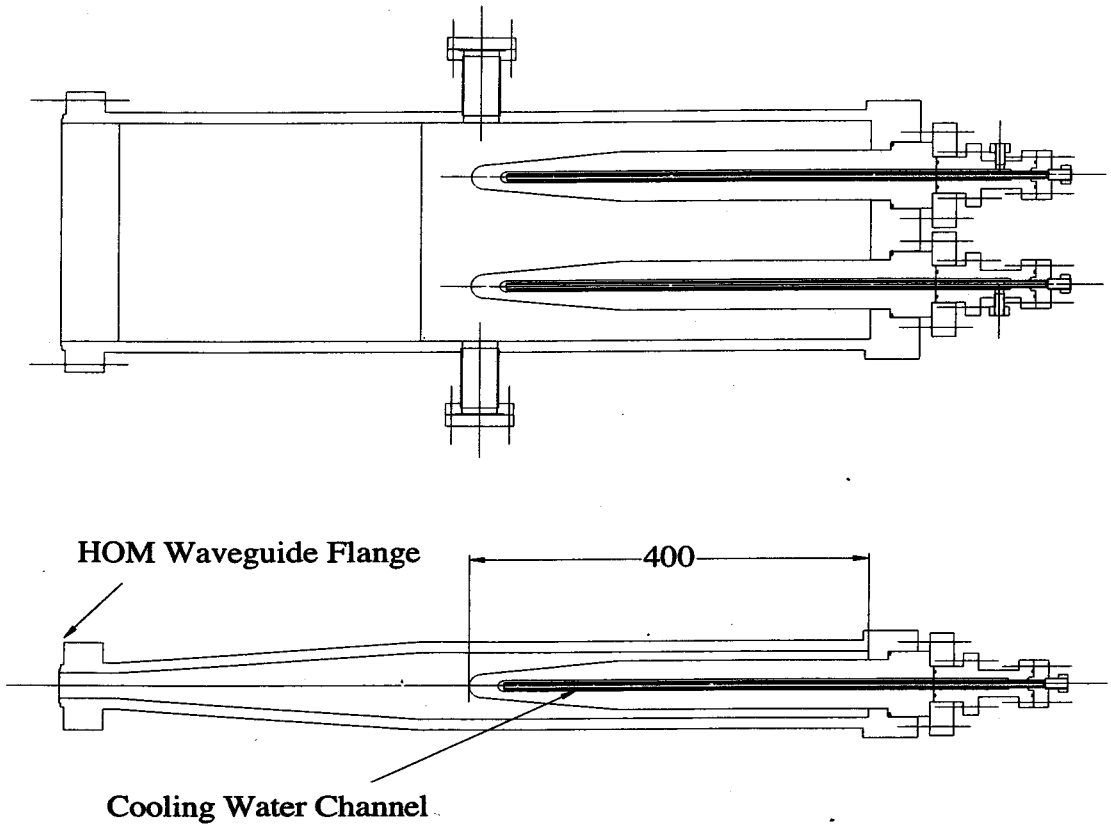

Fig. 4.2. Two bullet-shape sintered SiC ceramic absorbers inserted at the end of the HOM waveguide.

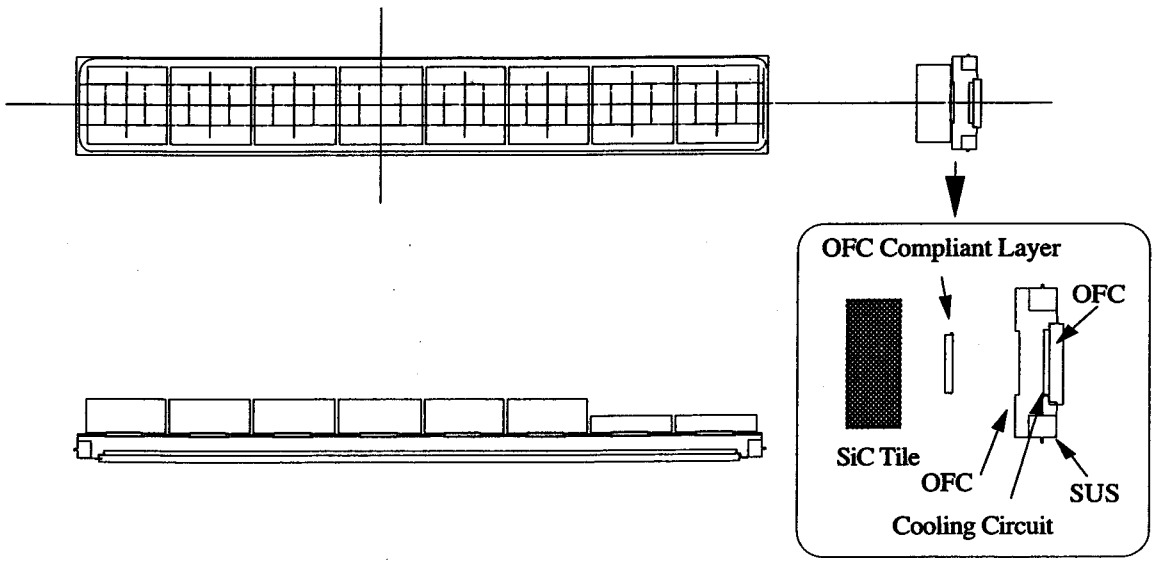

Fig. 4.3. HOM load for the grooved beam pipe.
SiC ceramic tiles brazed to the water-cooled copper plate.

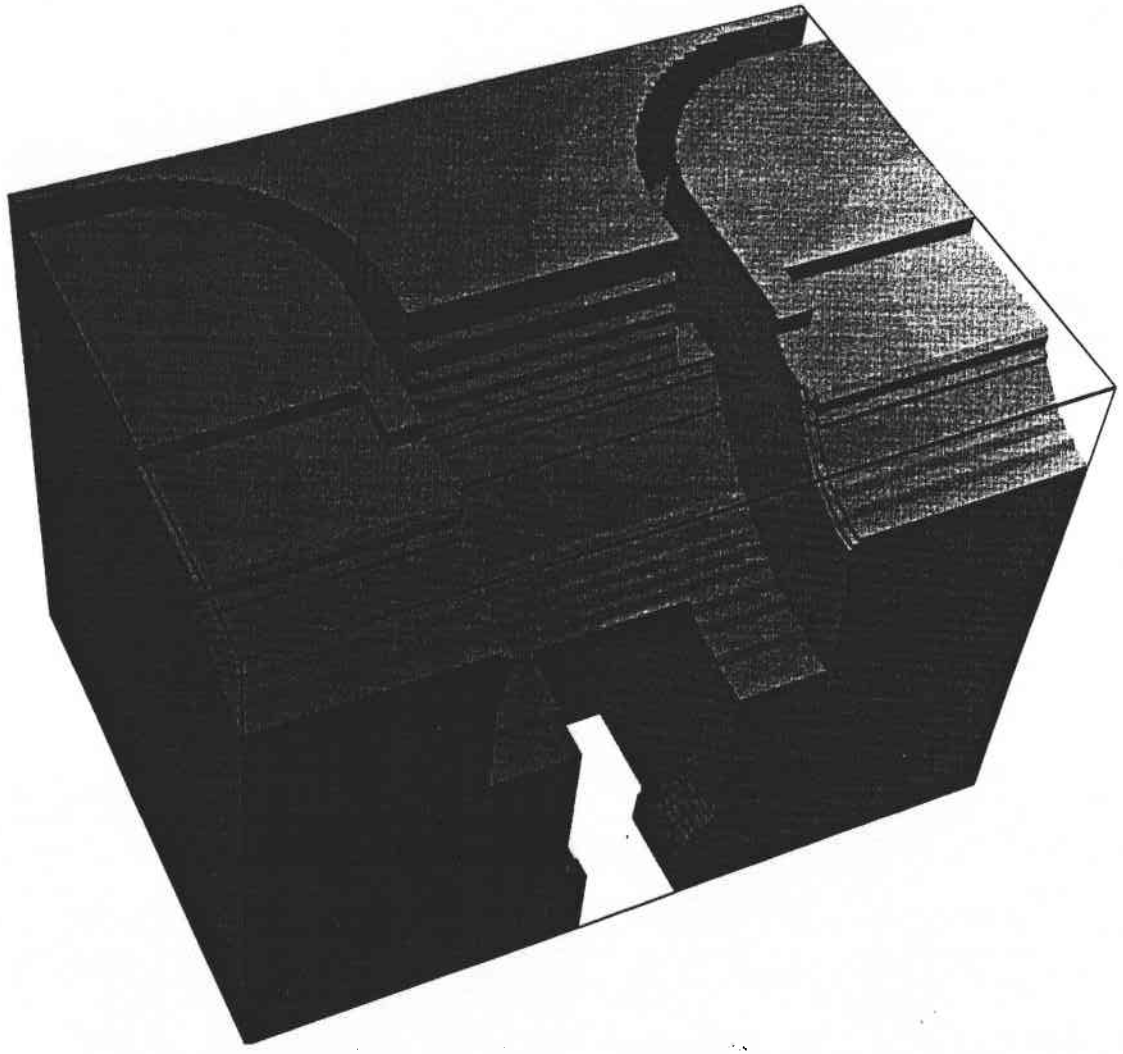

Fig. 4.4. The 3D geometry used to investigate the HOM damping properties with MAFIA-T3. The accelerating cavity is coupled with the half-cell coupling cavity. The beam-induced HOM fields propagate away through the HOM waveguides and grooved beam pipes.

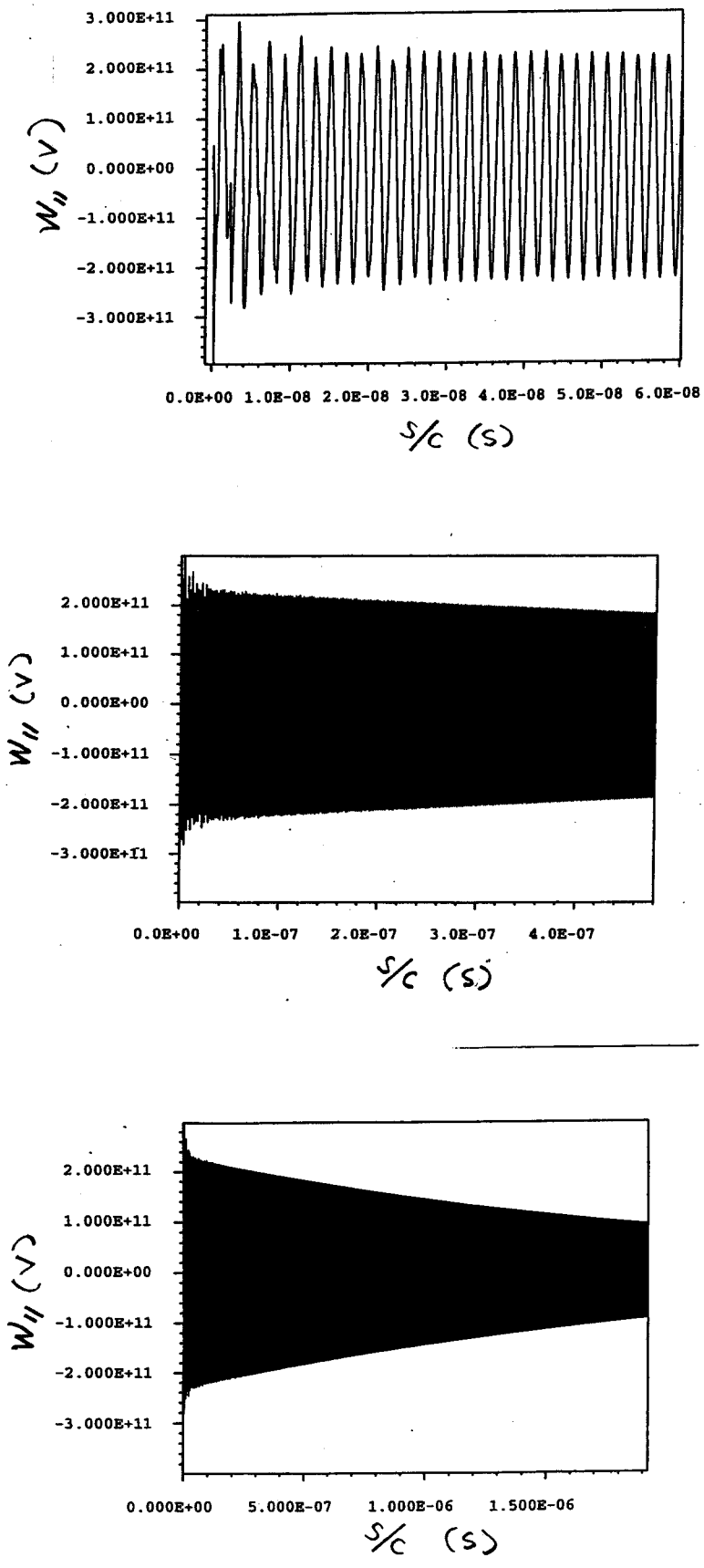

Fig. 4.5. Longitudinal wake potential traces computed with MAFIA T-3 up to the distances of 144, 288 and 576 m behind the bunch. The trace distance is divided by the speed of light and expressed in units of time.

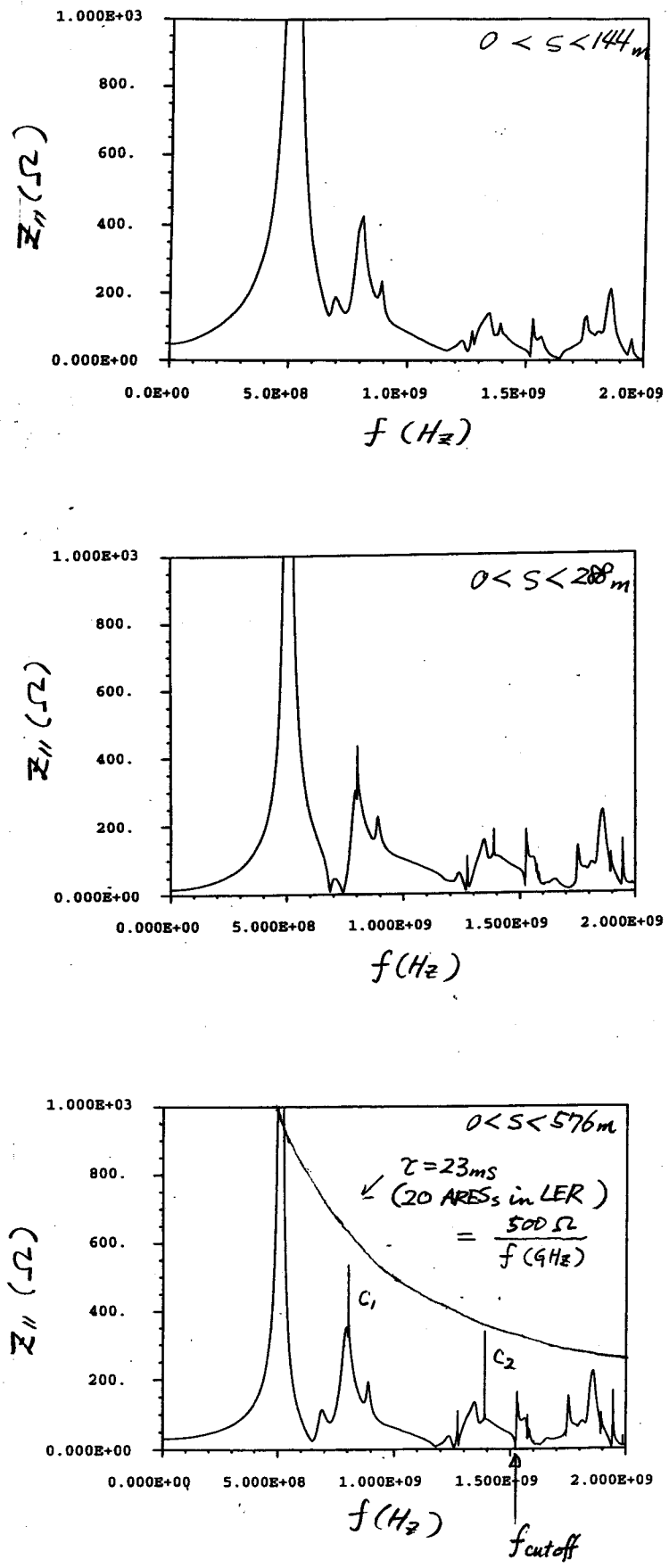

Fig. 4.6. Longitudinal coupling impedance spectra calculated from Fourier transforming the wake potential traces in Fig. 4.5, together with the threshold impedance per cavity for the KEKB LER operated with 20 ARES cavities.

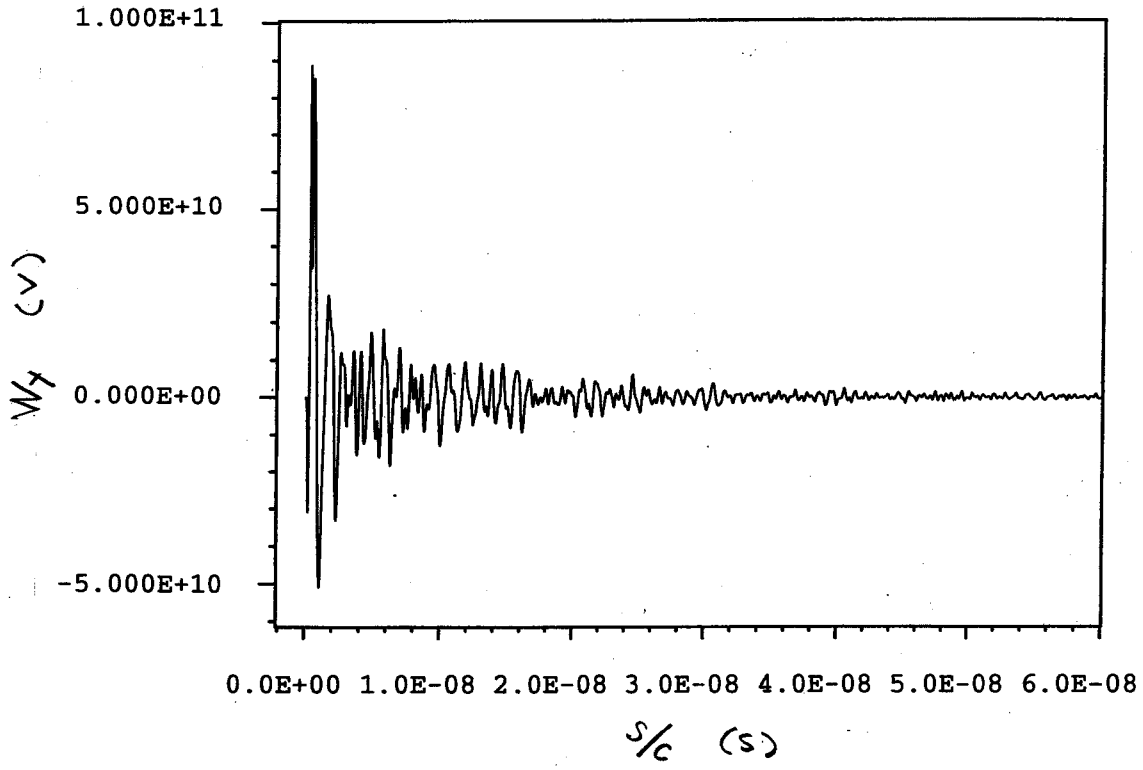

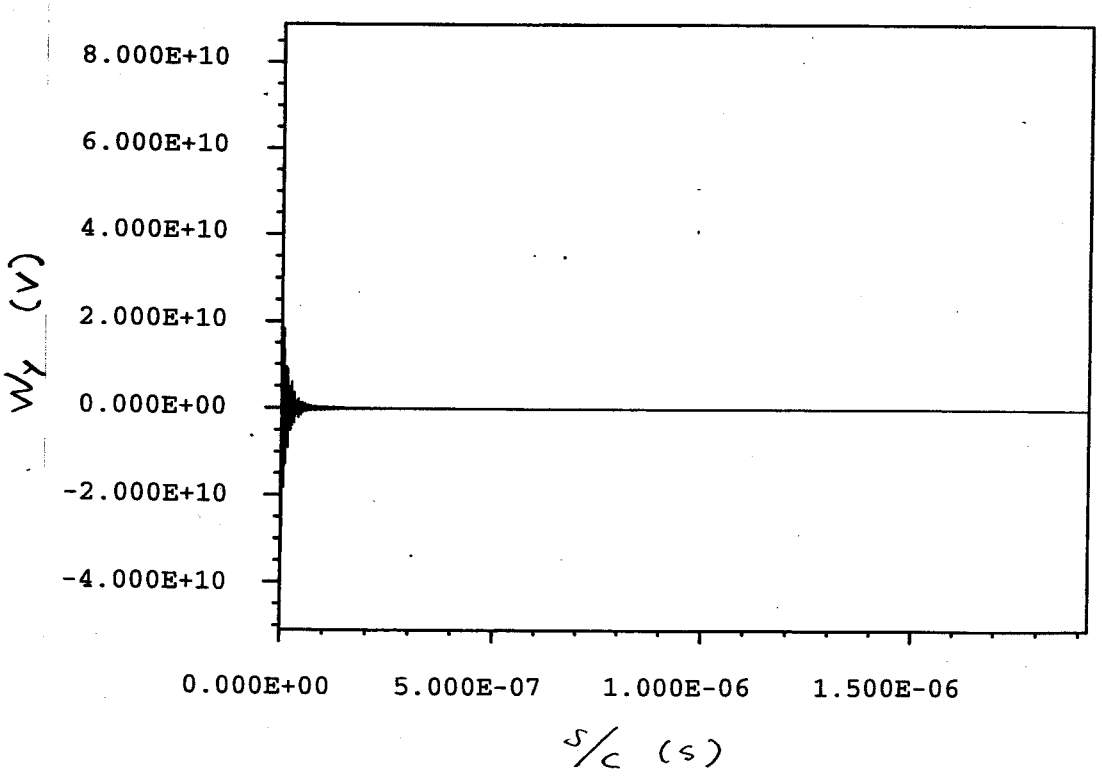

Fig. 4.7. Vertically transverse wake potential traces computed with MAFIA-T3 up to the distances of 144 and 576 m behind the bunch.

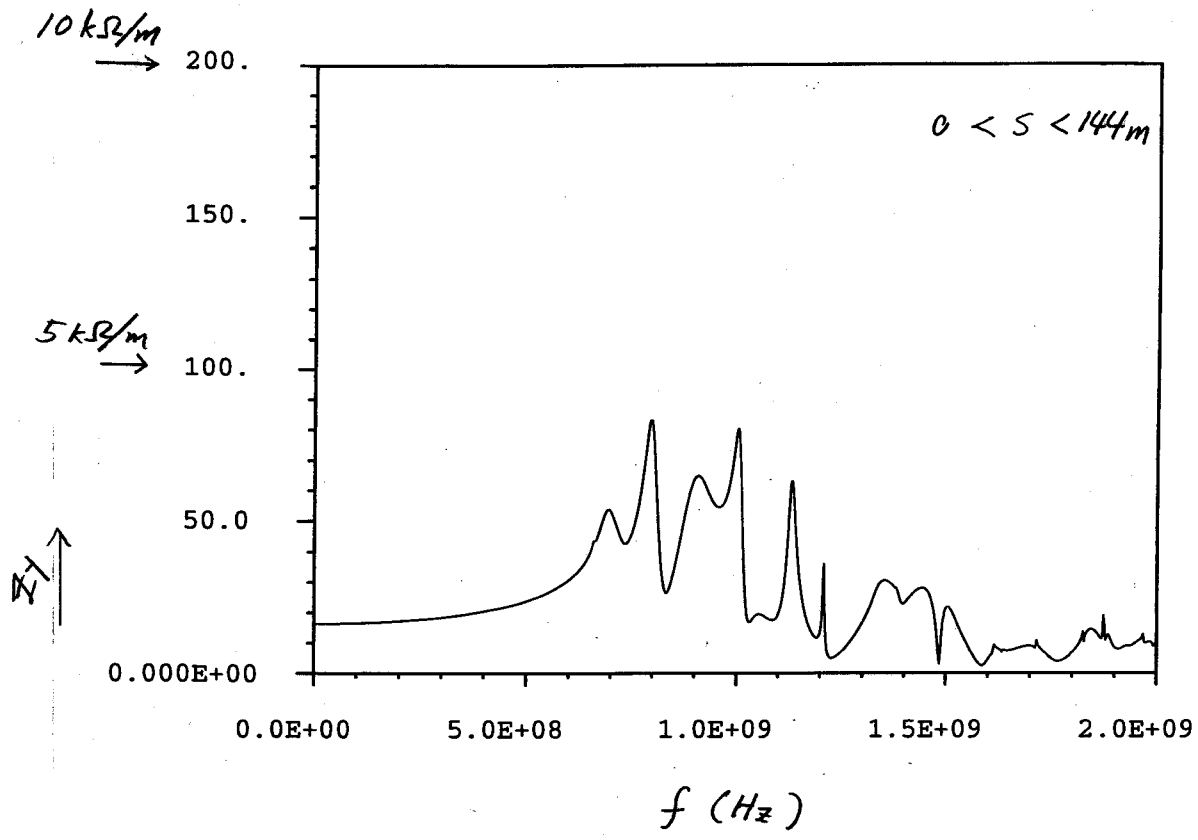

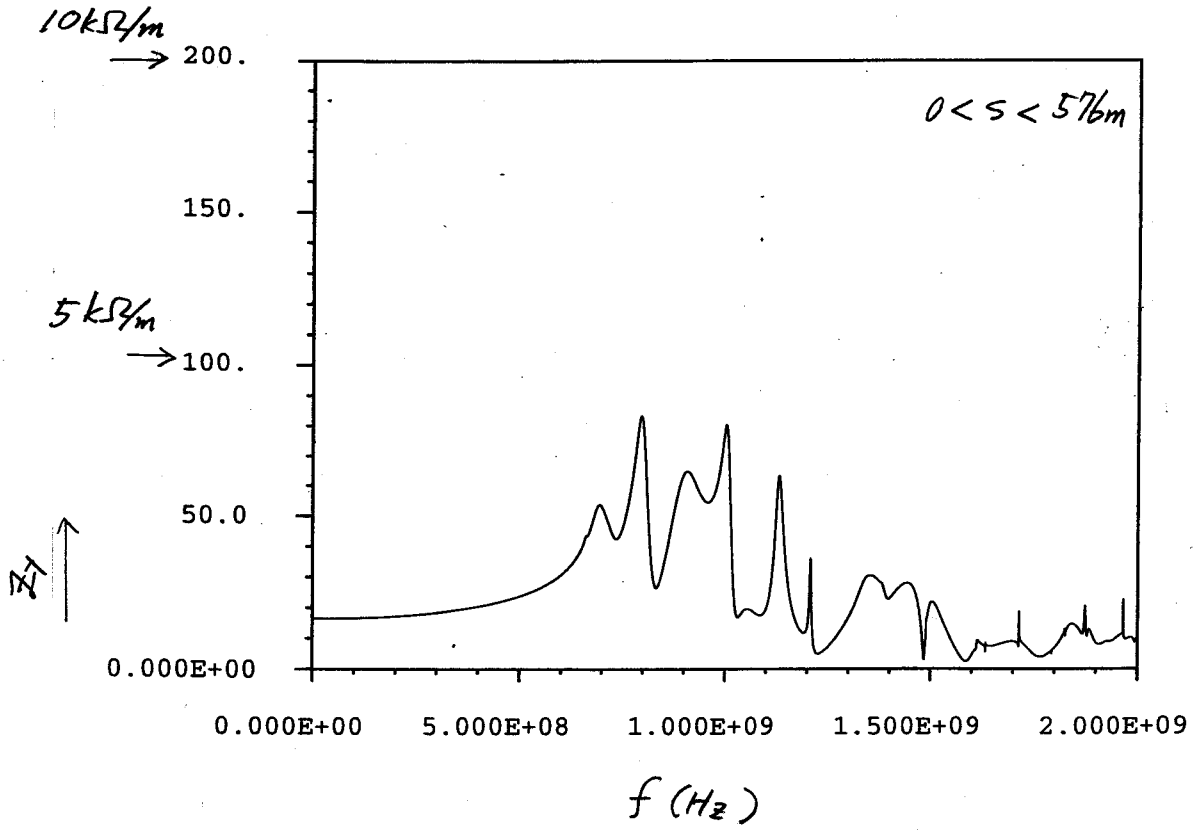

Fig. 4.8. Vertically transverse coupling impedance spectra calculated from Fourier transforming the wake potential traces in Fig. 4.7.

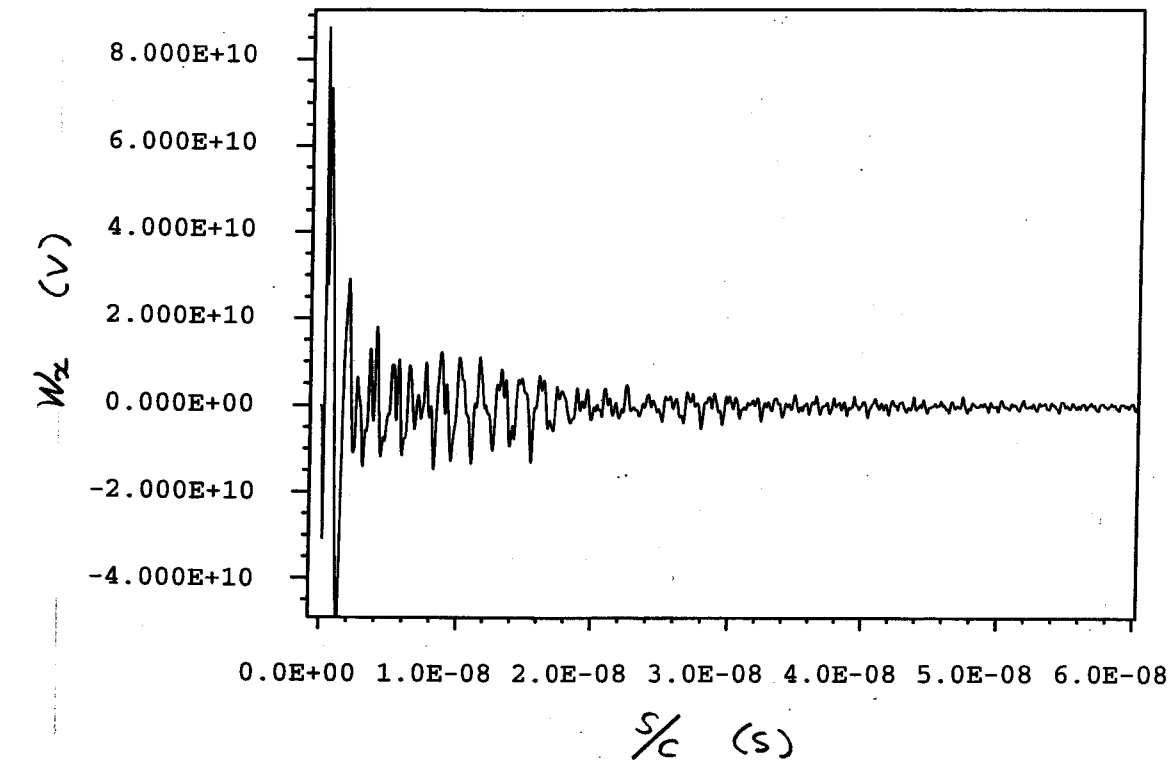

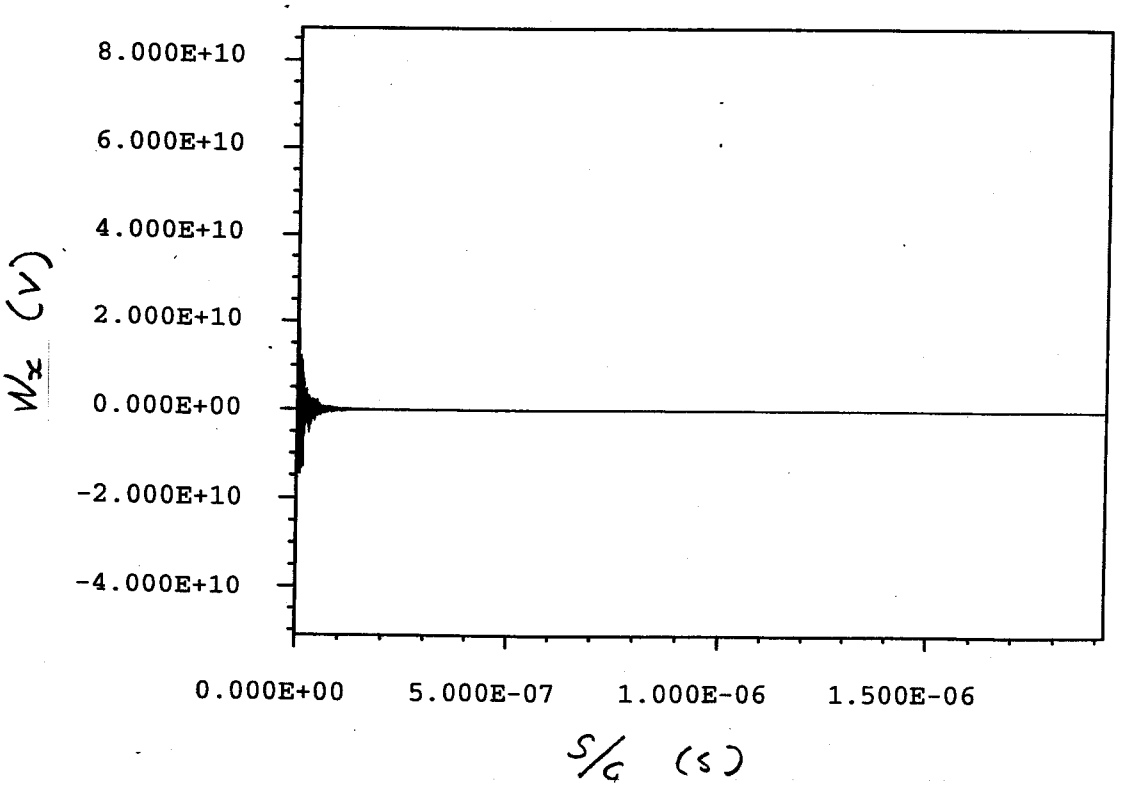

Fig. 4.9. Horizontally transverse wake potential traces computed with MAFIA-T3 up to the distances of 144 and 576 m behind the bunch.

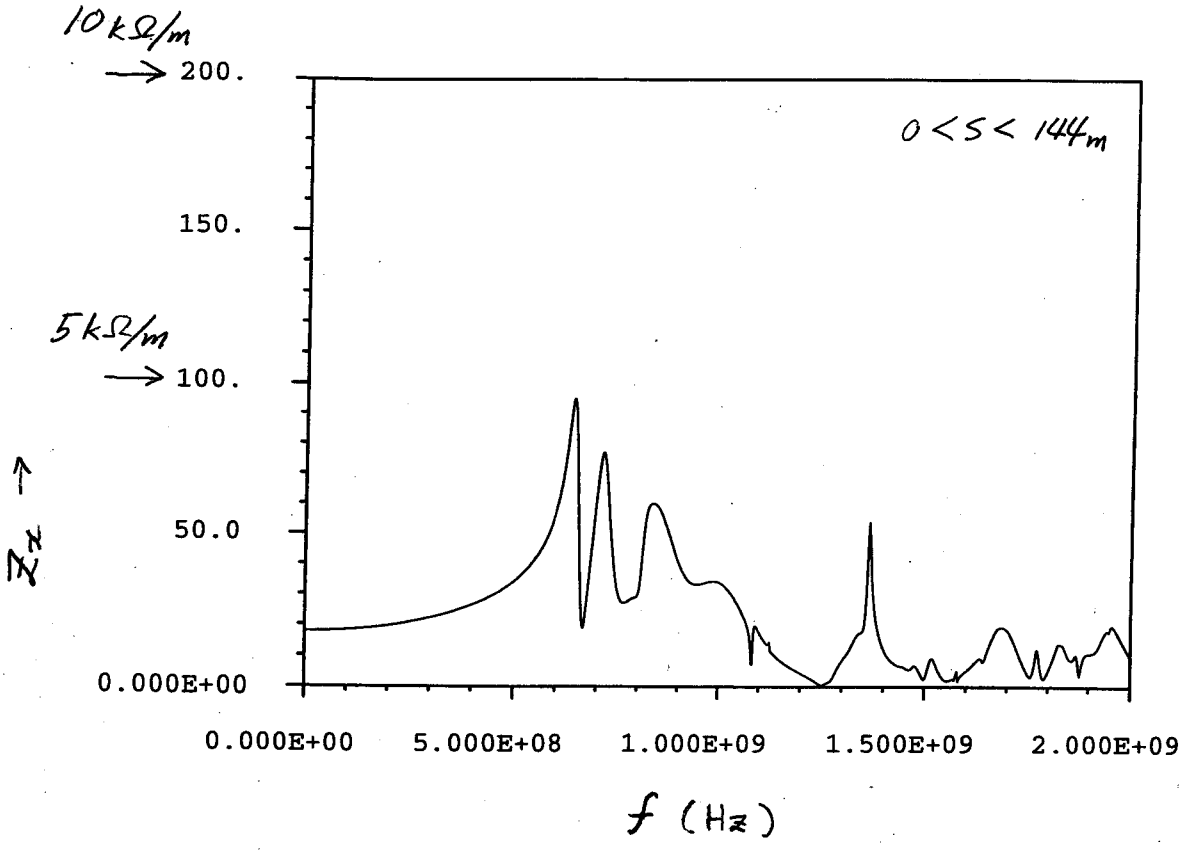

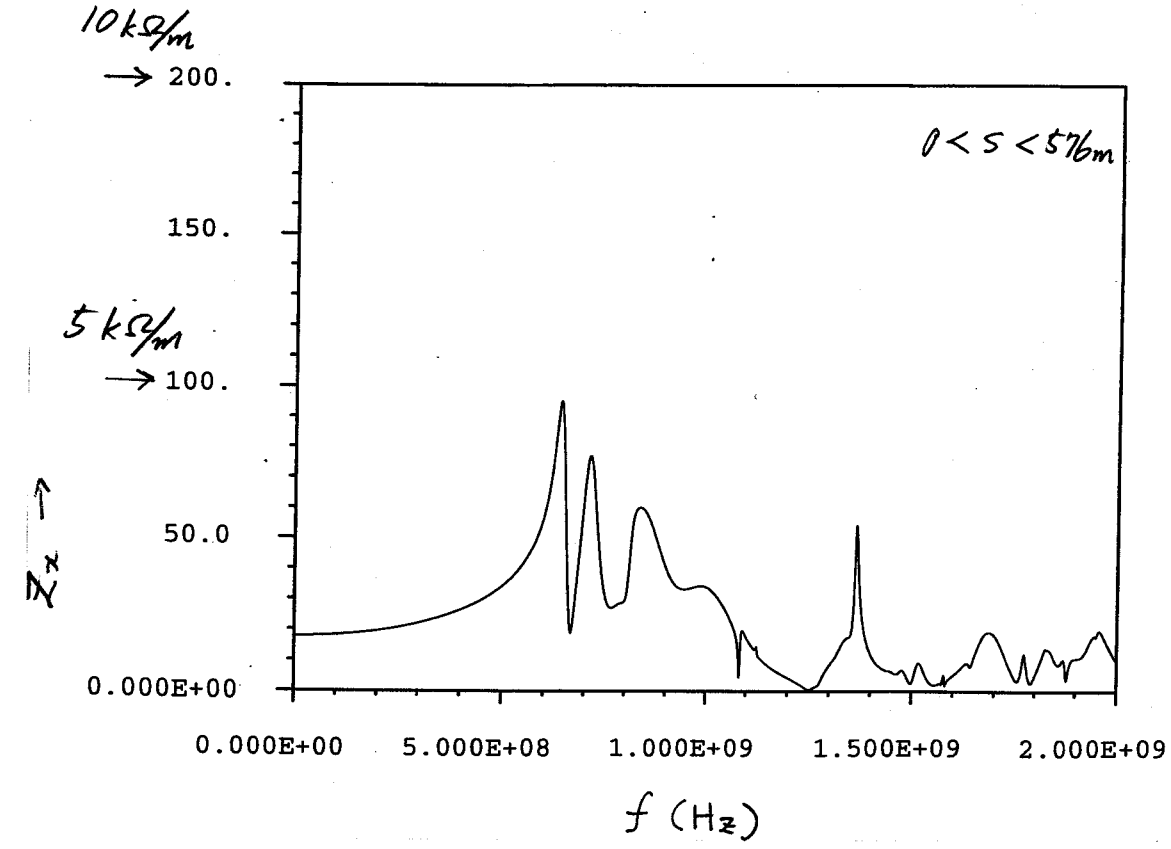

Fig. 4.10. Horizontally transverse coupling impedance spectra calculated from Fourier transforming the wake potential traces in Fig. 4.9.

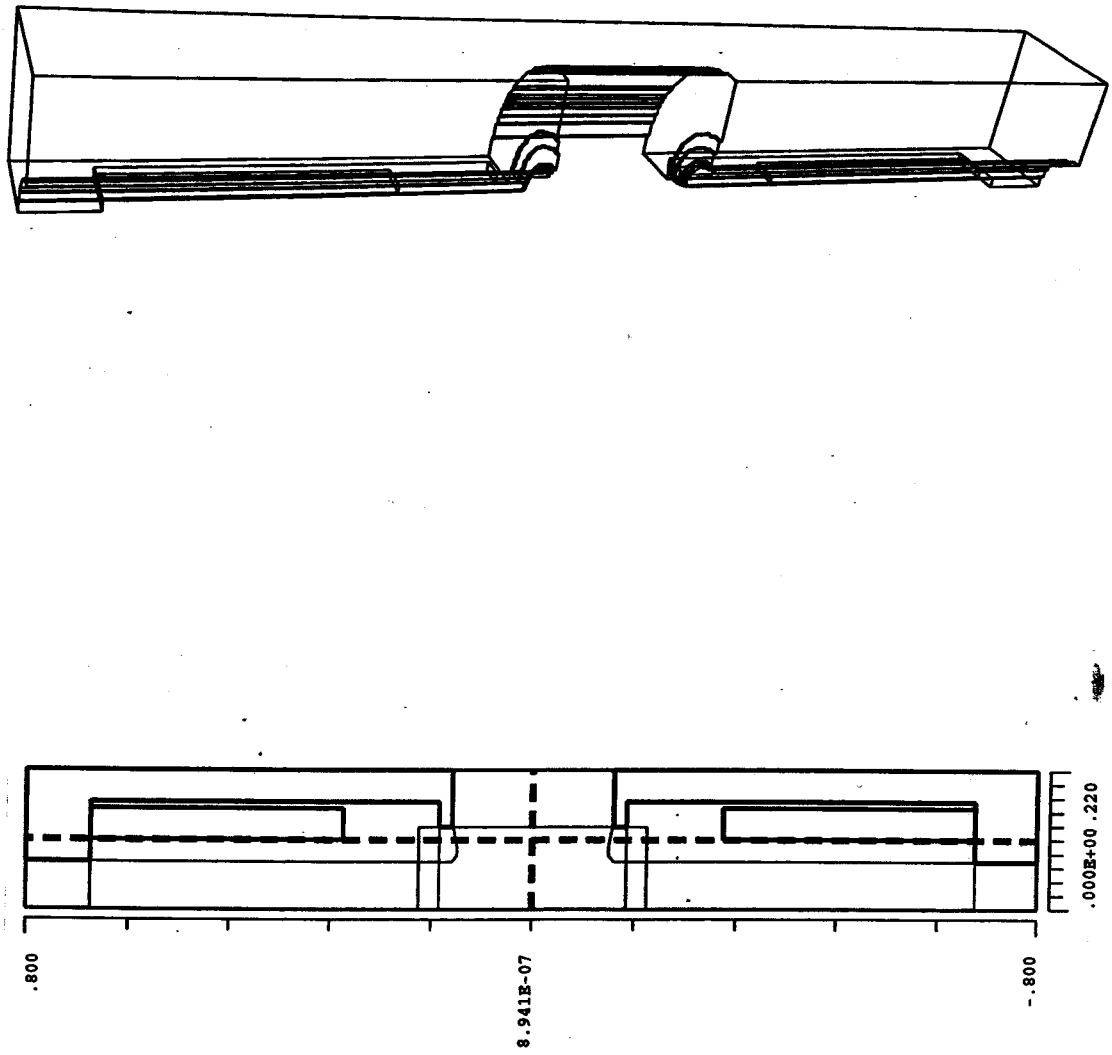

Fig. 4.11. The 3D geometry reflecting more realistically the actual grooved beam pipe structure with a finite length and loaded with SiC tiles in every groove.

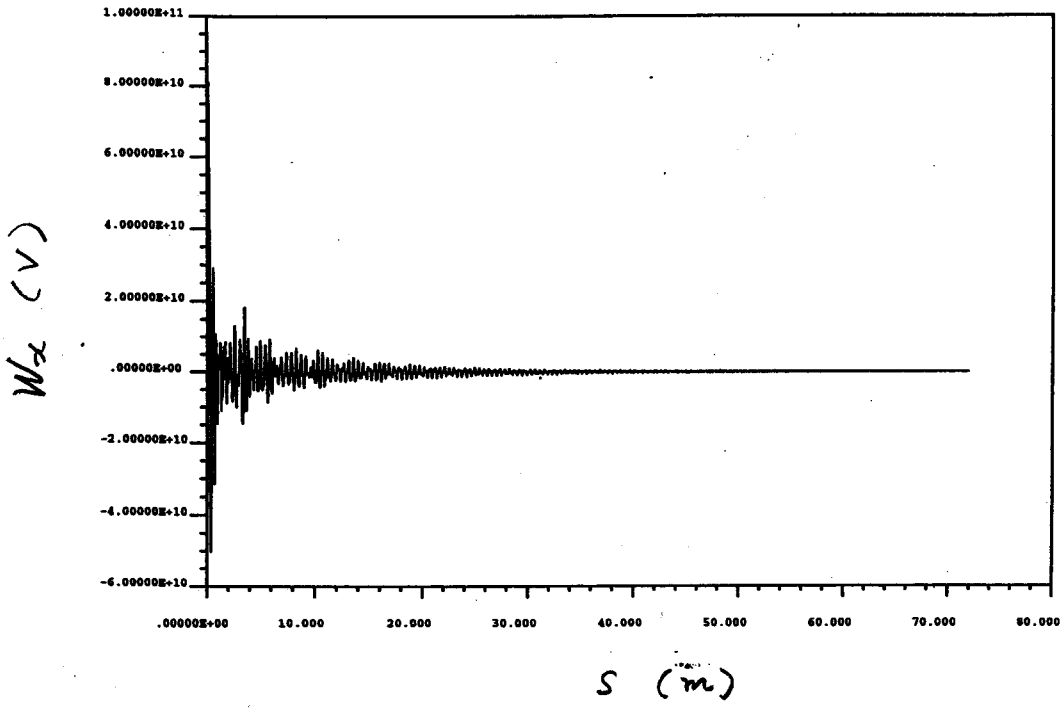

Fig. 4.12. A horizontally transverse wake potential trace computed with MAFIA-T3 up to the distance of 72 m behind the bunch

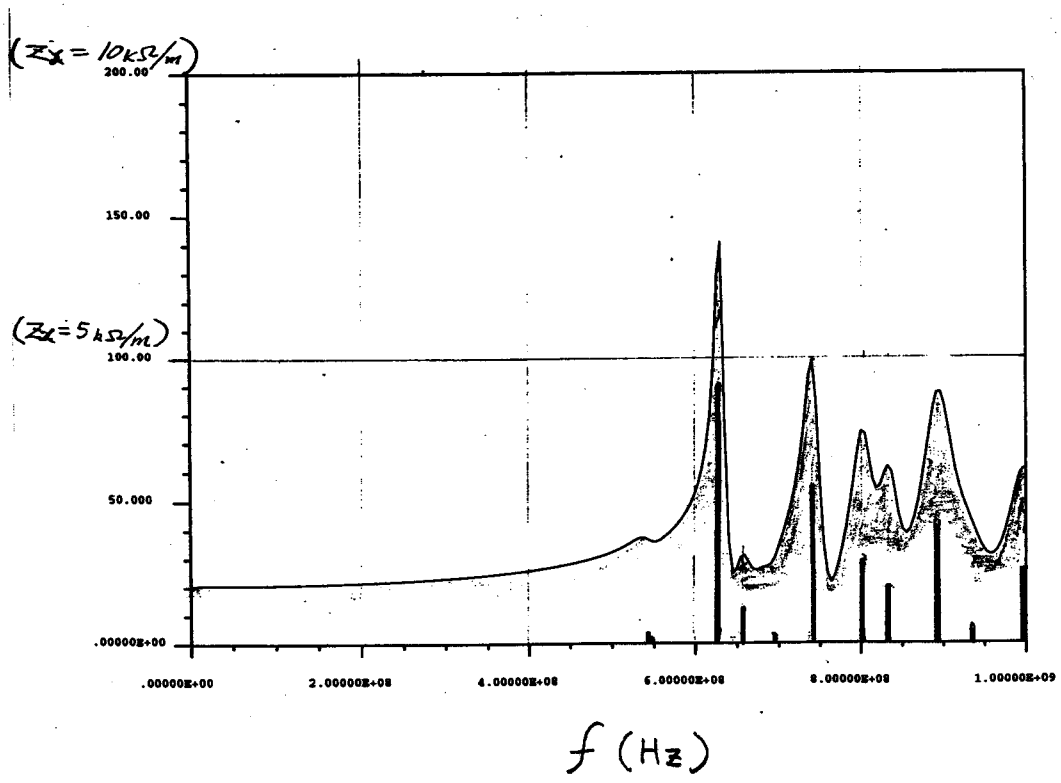

Fig. 4.13. A horizontally transverse coupling impedance spectrum calculated from Fourier transforming the wake potential trace in Fig. 4.12. The spectrum is compared with the results of the frequency-domain simulation with MAFIA indicated by bars.

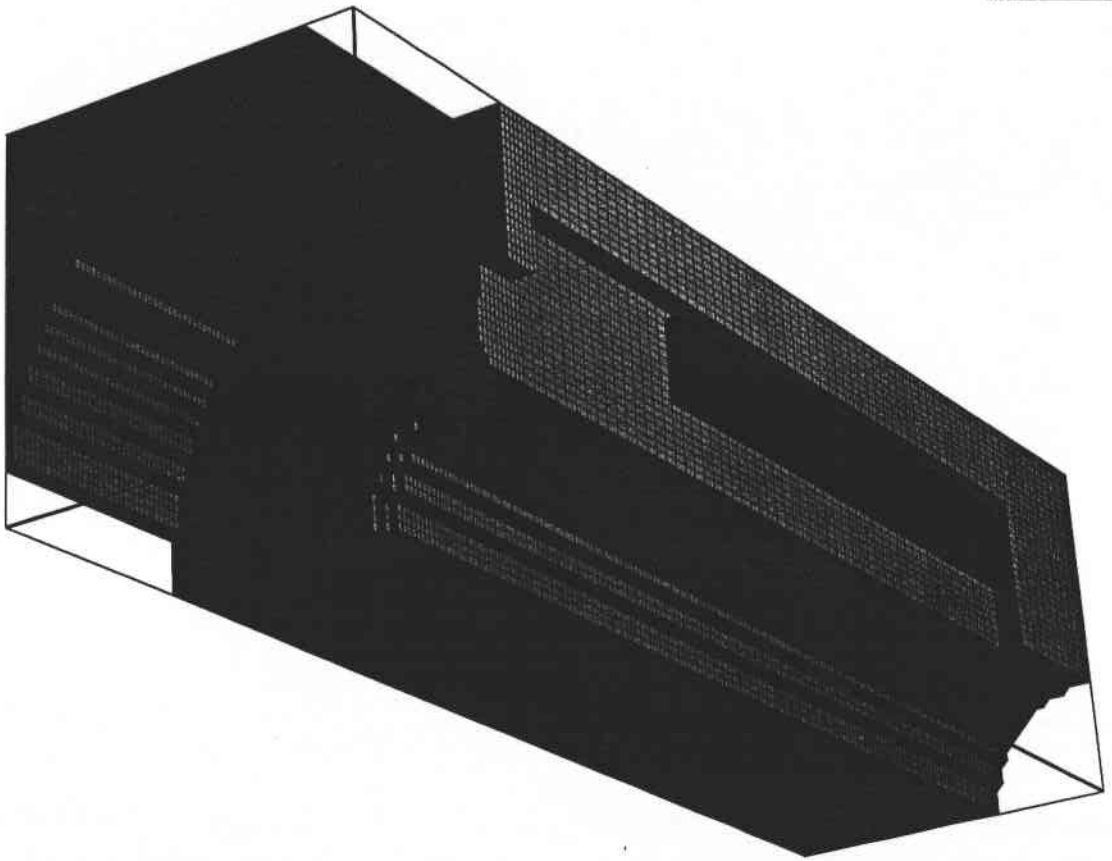

Figure 4.14. The 3D geometry implemented to the frequency-domain simulation with MAFIA.

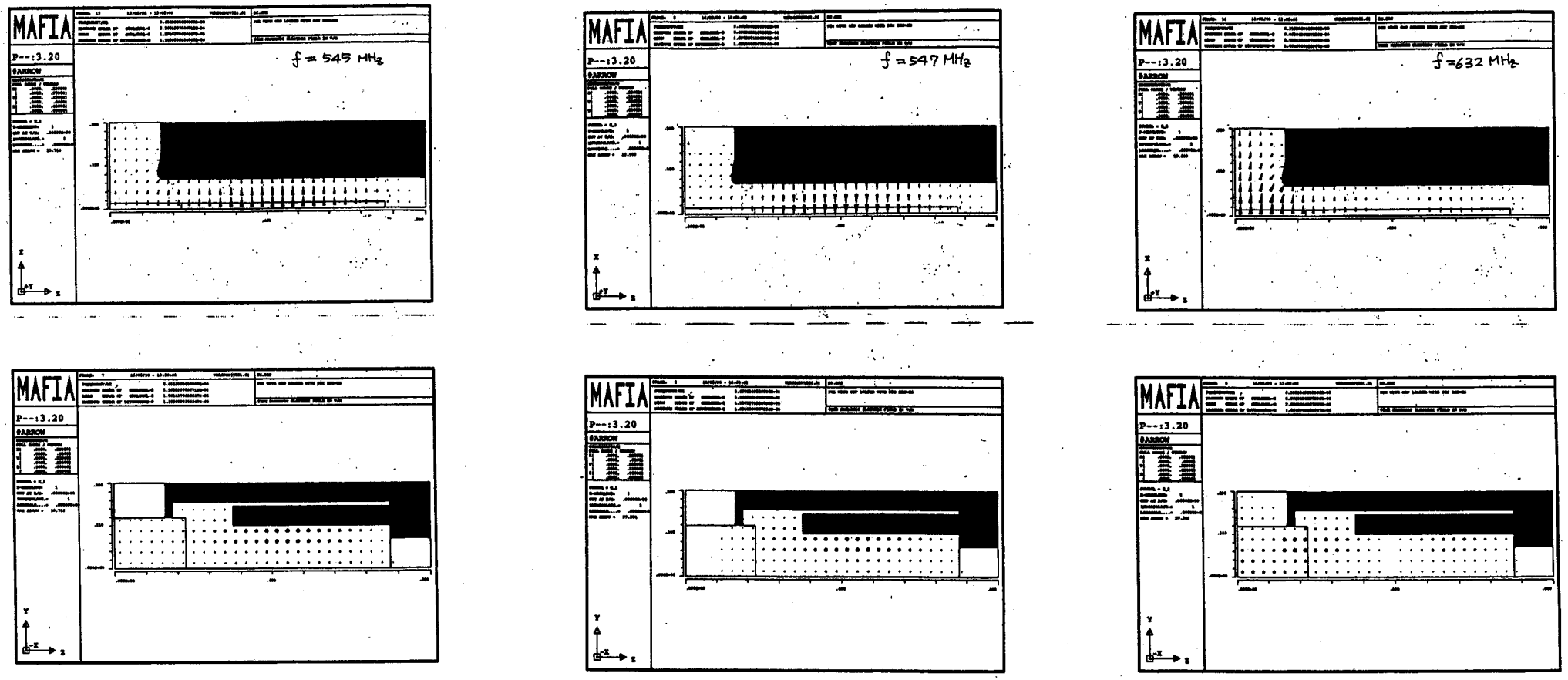

Fig. 4.15 (a). The HOM field patterns of H-dipole modes obtained from the frequency domain simulation with MAFIA.

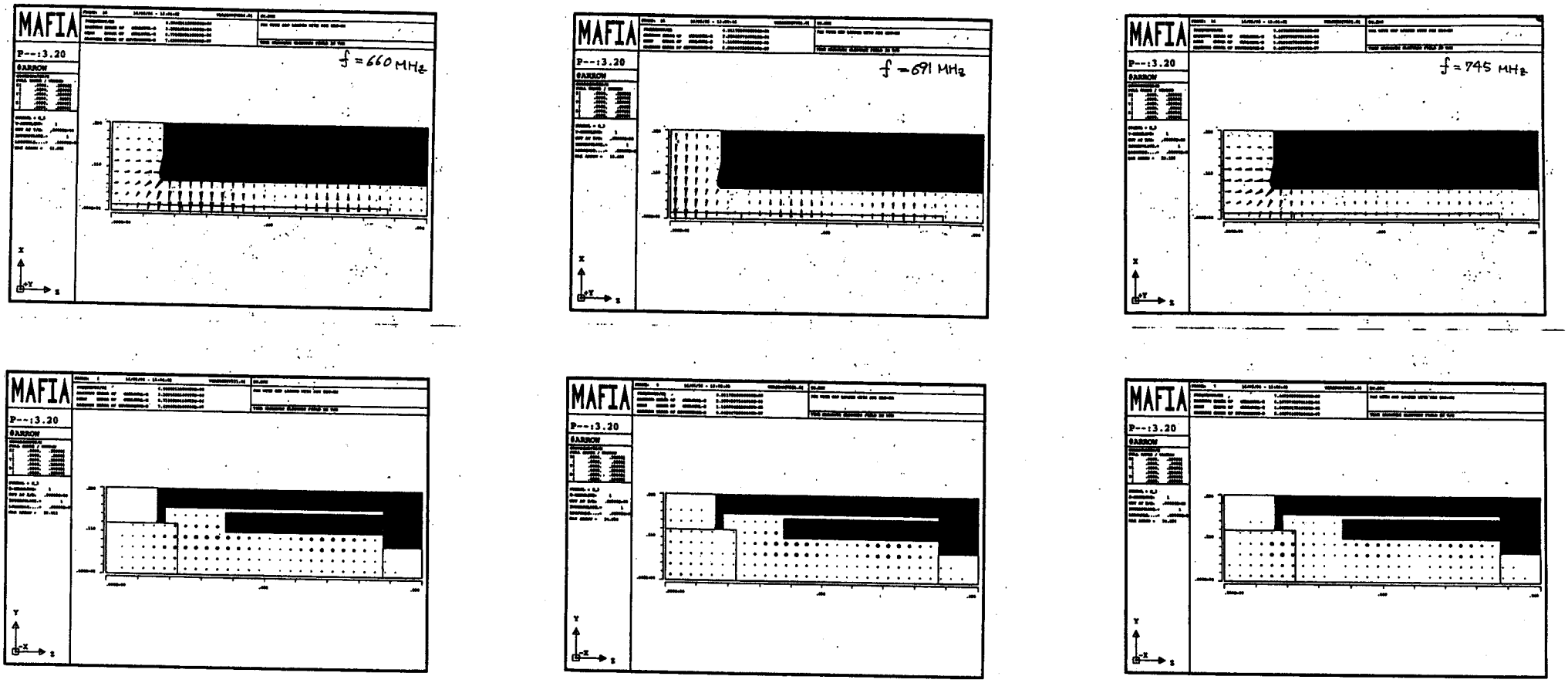

Fig. 4.15 (b). The HOM field patterns of H-dipole modes obtained from the frequency domain simulation with MAFIA.

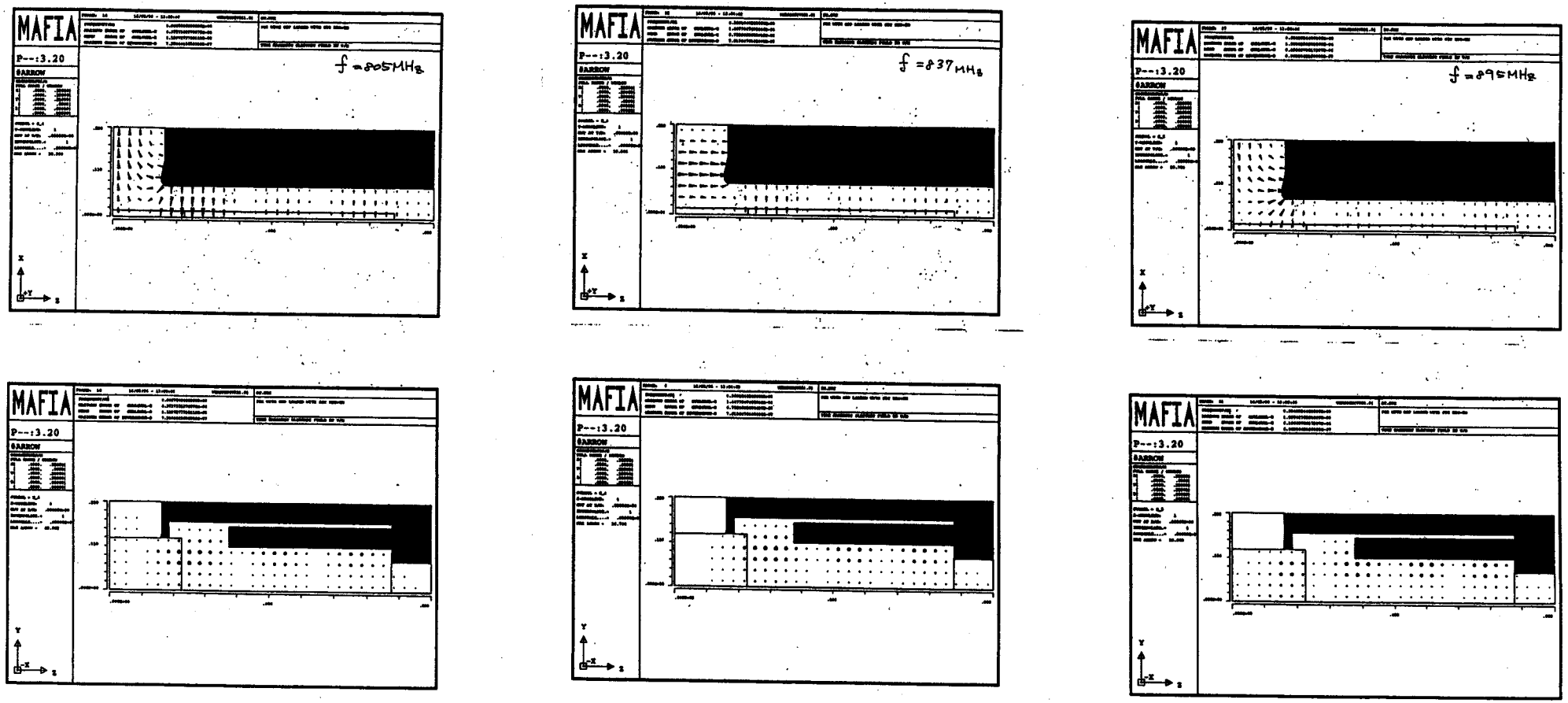

Fig. 4.15 (c). The HOM field patterns of H-dipole modes obtained from the frequency domain simulation with MAFIA.

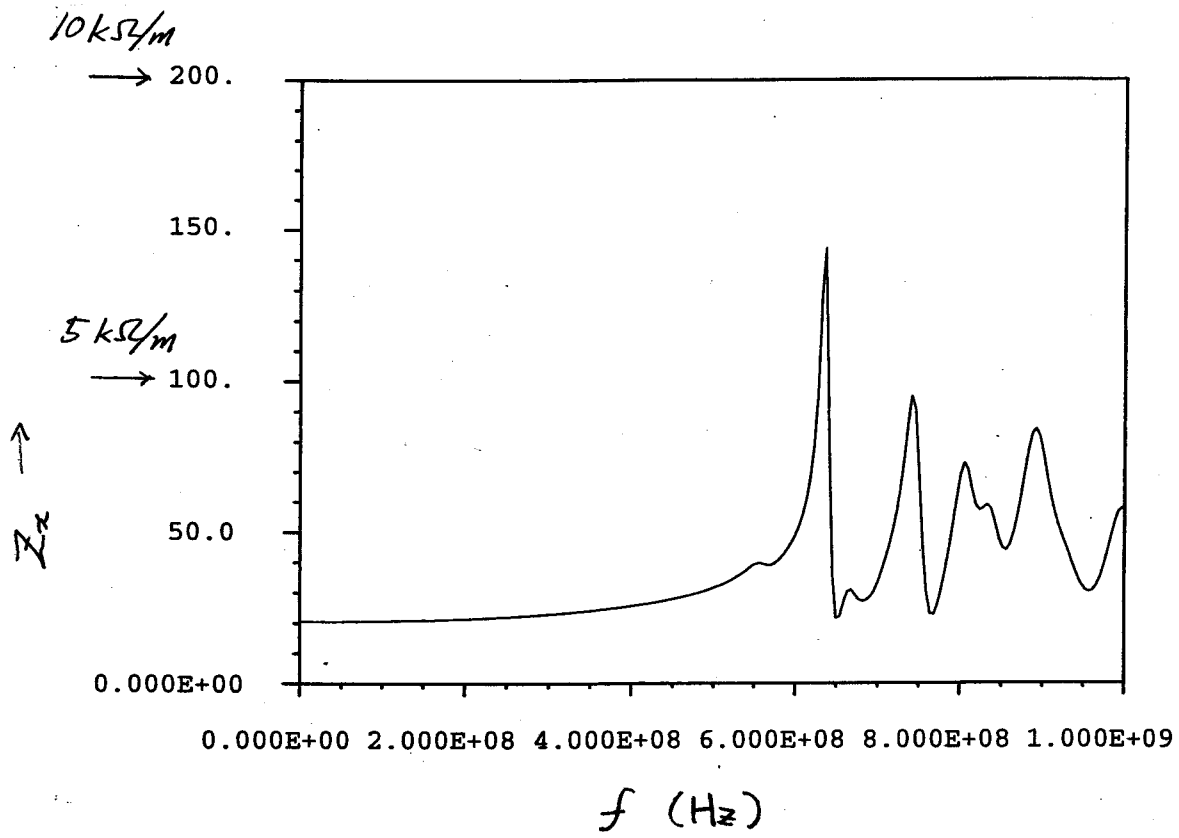

Fig. 4.17. A horizontally transverse coupling impedance spectrum computed with MAFIA T3 for the accelerating cavity with tapered groove beam pipes at both ends.

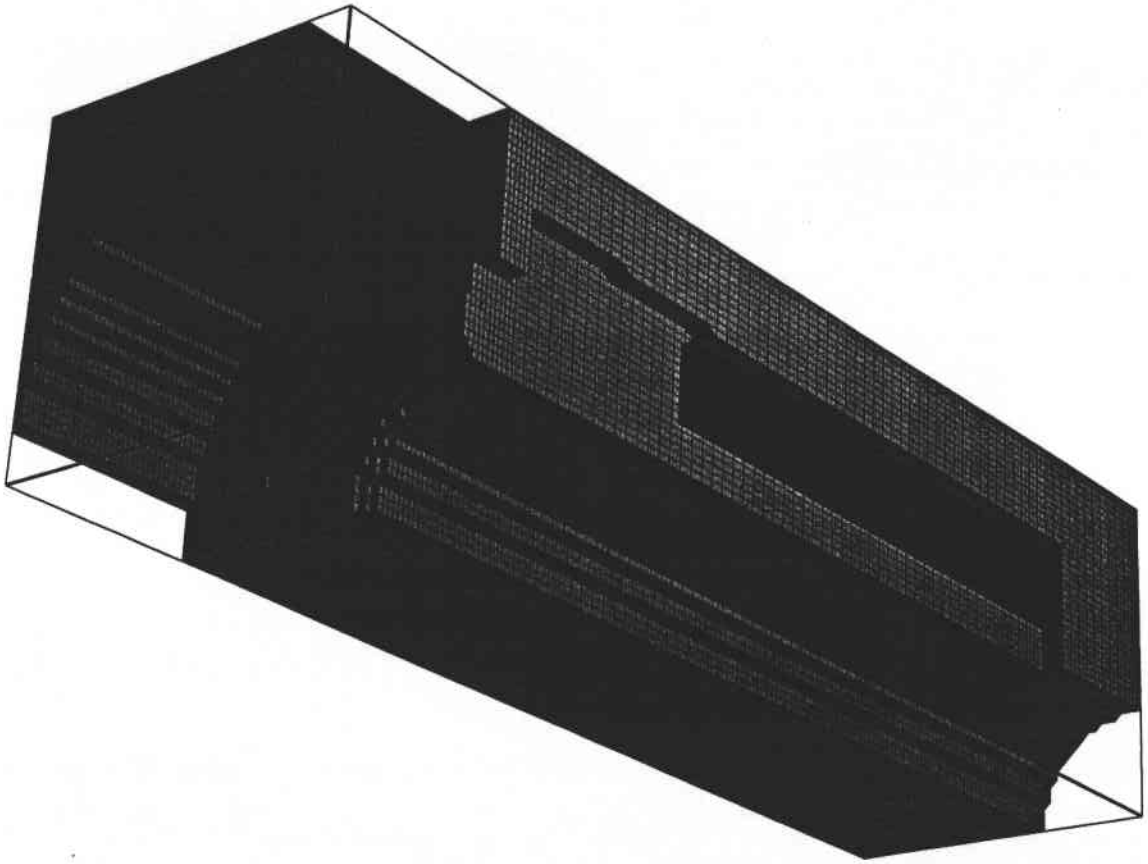

Fig. 4.16. The 3D geometry of the tapered groove beam pipe so as to the TE112-like mode away from the accelerating mode.

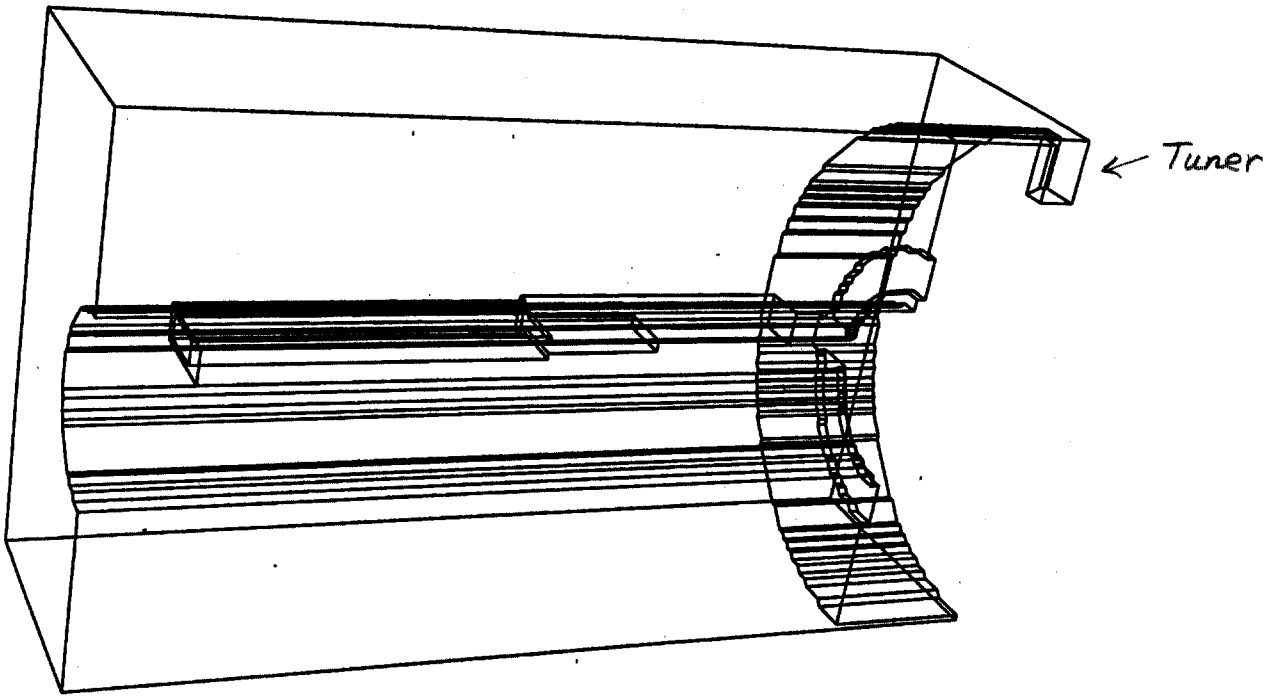

Fig. 4.18. The 3D model geometry implemented to MAFIA to compute the reduction in the Q value of the fundamental mode due to the dipole-mode mixing caused by insertion of a tuning plunger.

Chapter 5.
BEAM EXPERIMENTS

5.1. Overview

In this chapter, two beam-based experiments on the HOM-damped structure of the ARES cavity system are described. One is HOM spectrum measurement of the conceptual demonstrator ARES96, which was carried out in the TRISTAN AR before the cavity production for KEKB project. The other is HOM power measurement of some ARES cavities actually operated for the LER of KEKB to support the high-current beam over 1000 mA.

Figure 5.1 shows a photo of the conceptual demonstrator ARES96 installed in the TRISTAN AR tunnel, equipped with an input coupler at the storage cavity (left) and with a parasitic mode damper at the coupling cavity (center). Major objectives of the beam experiment in the TRISTAN AR are summarized as follows:

- To demonstrate the fundamental RF characteristics of the ARES cavity system including the parasitic mode damper under heavy beam loading conditions.
- To check out other accessory devices such as the movable tuners, the input coupler, and the HOM loads.
- HOM spectrum measurement with use of a single-bunch beam.

As mentioned in the chapter 3, ARES96 had been successfully demonstrated as a production prototype for KEKB. Some experimental results on the first objective item were reported in Ref. [33].

From 1997 to 1999, 36 ARES cavities (20 for LER and 12 for HER) were produced in total including 4 spare cavities. Every production cavity was RF-conditioned and tested up to 120% of the design input power of 150 kW [39]. The assembly line and high-power test stand for the production cavities are shown in Fig. 5.2 and Fig. 5.3, respectively.

Figure 5.4 is a photo of ARES cavities installed in the RF section D7 for the LER. KEKB was commissioned stepwise as follows. The HER was first commissioned in

December 1998 with a combination of 6 ARES cavities in the RF section D5 and 4 superconducting cavities in the RF section D11, followed by the commissioning of the LER with 12 ARES cavities (6 in D7 and 6 in D8). In the summer of 1999, the number of ARES cavities for the LER was increased from 12 to 16 (10 in D7 and 6 in D8), and for the HER from 6 to 10 (4 in D4 and 6 in D5). The high luminosity operation was started in the fall of 1999. In the suumer of 2000, the number of superconducting cavities was doubled (4 in D10 and 4 in D11). The beam currents of both rings were increased stepwise, overcoming many difficulties and improving the machine performance [40]. As a whole, the ARES cavities have performed well to support the beam currents up to 1570 mA in the LER and up to 940 mA in the HER.

5.2. HOM Spectrum Measurements

The conceptual demonstrator ARES96 shown in Fig. 5.1 was directly installed in the TRISTAN AR tunnel after the fabrication completed, and high-power tested there before the beam experiment. The accelerating cavity is fully equipped with the HOM loads described in the previous chapter. A cylindrical SiC duct [41] with an inside diameter of 150 mm is attached to the end of each GBP in order to damp HOMs above the beam pipe cutoff. Beyond the SiC duct, the inside diameter is tapered down to 100 mm so as to match the regular size of the beam chamber for the AR. Major machine parameters of the AR are summarized in Table 5.1.

Table 5.1: Machine parameters of the TRISTAN Accumulation Ring (AR).

RF Frequency	508.5808 MHz
Harmonic Number	640
Revolution Frequency	794.6575 kHz
Beam Energy	2.5 GeV
RF Voltage	0.4~2.0 MV
Bunch Length	> 15 mm

HOM spectra excited by a single-bunch beam of about 100 mA passing through the accelerating cavity were measured changing the tuner positions for the accelerating and storage cavities. Figure 5.5 shows a typical HOM spectrum excited by a bunch traveling on the cavity axis. This was observed with a probe antenna at the endplate of the accelerating cavity. The probe antenna was positioned so as to monitor both polarizations for the dipole HOMs in addition to the monopole modes. A simulation using the MAFIA-T3 code reproduced this observed spectrum as shown in Fig. 5.6, including two sharp peaks indicated by C1 and C2. This computed spectrum was obtained by the Fourier transformation of the time trace of the beam-induced electric field at the position of the probe antenna. Further simulation studies, actually carried out after observation of the modes C1 and C2, has shown that both are trapped modes in the coupling cavity as mentioned in the previous chapter. As shown in Fig. 5.7, the mode C1 has a TM_{110}- like field pattern in the coupling cavity and the mode C2 has a TE_{111}-like one. The coupling impedances of these modes are expected manageable below the threshold as shown in Fig 4.6 in spite of their high Q values because they have almost no electromagnetic fields in the accelerating cavity.

In this series of beam-based measurements, the spectrum for the H-dipole modes to be damped with the grooved beam pipes could not be clearly observed with the probe antenna at the endplate of the accelerating cavity, even with use of an off-axis beam by 5 mm in the horizontal direction. Figure 5.8 is a spectrum obtained from low-power measurement with a network analyzer for the H-dipole modes, carried out after the beam experiment. The accelerating cavity was excited through one grooved beam pipe with a probe antenna, as shown in Fig. 5.9. The transmission signal was observed with another probe antenna at the other grooved beam pipe. The storage cavity was separated from the coupling cavity and the aperture was short-circuited with an aluminum plate attached to the rectangular flange. As seen from Fig. 5.8, all the H-dipole modes are well damped. However, the number of modes increases compared with the computed spectrum in Fig. 4.13. This is probably due to the presence of the coupling and half-cell coupling cavities at both sides of the accelerating cavity. The $\pi/2$-mode termination with a short-circuiting plane cannot forbid horizontally polarized dipole modes in the half-

cell coupling cavity. Therefore, the number of H-dipole modes may increase in the side-coupled three-cell structures as shown in Fig. 5.9, compared with the case for the accelerating cavity only as shown in 4.11.

The conceptual demonstrator ARES96 was successfully operated in the TRISTAN AR to support the beam (4 4-bunch trains) up to 460 mA without beam instabilities due to the cavity HOMs. However, this beam experiment brought a slight change in the design of the production cavity to avoid risks. That is a spare rectangular port of 240 mm by 28 mm attached to the coupling cavity as shown in Fig. 5.9 so as to damp the modes C1 and C2 with the dipole fields trapped in the coupling cavity if necessary.

5.3. HOM Power Measurements

Currently the RF section D7 has 10 out of 16 ARES cavities for the LER. The beam chambers for the RF section have the same inside diameter of 150 mm as the circular part of the GBP. Each end of the RF section is equipped with a cylindrical SiC duct with an inside diameter of 150 mm and a length of 240 mm, and with a tapered beam chamber so as to match the regular inside diameter of 94 mm for the LER.

For every ARES cavity in the RF section D7, the HOM power dissipated in the four bullet-shape SiC absorbers of the two HOM waveguides at the downstream side with respect to the beam direction was obtained from the temperature rise of the cooling water flowing through the four absorbers in series and the flow rate adjusted in advance. The errors in the calorimetric measurement were as follows: 3% coming from the temperature measurement estimated from the ratio of the temperature resolution of 0.1 degrees over a typical temperature rise of about 4 degrees, and 10% from the water flow measurement according to the supplier of the flow meters. Figure 5.10 shows the data obtained for every cavity, plotted as a function of the LER beam current in a range from 800 mA to 1300 mA. The bunch pattern was a single train of 1224 bunches with 4-bucket spacing followed by a gap of about 230 successive vacant buckets. The mirror symmetry of the cavity structure with respect to the beam direction assures that twice the power in Fig. 5.10 is equal to the total HOM power dissipated in the four rectangular waveguides (WG HOM power dissipation) of each cavity, which amounts to

about 3.2 kW at 1300 mA. The data of each cavity was fitted assuming a quadratic dependence of the HOM power on the beam current. Figure 5.11 is a bar graph of the coefficients of the quadratic term obtained from fitting, showing the variation of the HOM-waveguide power dissipation from cavity to cavity along the RF section D7 with respect to the beam direction. It can be said that the HOM-waveguide power dissipation is almost independent of the cavity position in the RF section, considering the measurement errors stated above.

Also, the HOM power dissipation at the SiC tiles in the grooved beam pipe at the downstream side of each cavity was obtained in a similar way stated above. The errors in the calorimetric measurement for the grooved beam pipe were 8% from the temperature measurement estimated from the ratio of the temperature resolution of 0.1 degrees over a typical temperature rise of about 1.3 degrees, and 10% from the water flow measurement. Figure 5.12 shows the data obtained for every cavity, plotted as a function of the LER beam current. Again, twice the power in Fig. 5.12 is equal to the HOM power dissipated in both grooved beam pipes (GBP HOM power dissipation) because of the cavity symmetry. Figure 5.13 is a bar graph of the coefficients of the quadratic term obtained from data fitting in Fig. 5.12. Considering the errors in the calorimetric measurement, the power dissipation in the grooved beam pipe is also almost independent of the cavity position along the RF section.

For the ARES cavity C2 in the RF section D7, the WG HOM power dissipation and the GBP HOM power dissiation are plotted in Fig. 5.14 as a function of the beam current, together with the sum of these two power dissipations, that is, the total HOM power dissipation per cavity. The WG and GBP HOM power dissipations are obtained by simply doubling the data in Fig. 5.10 and Fig. 5.12, respectively. Further, the total HOM power dissipation and the GBP HOM power dissipation are compared with theoretical predictions shown by the solid and dashed curves, respectively. The prediction for the total HOM power dissipation was calculated from the loss factor computed with MAFIA-T3 for the accelerating cavity structure with the grooved beam pipes. The loss factor k is defined by the following relation:

$$\Delta U = kq^2, \tag{5.1}$$

where ΔU is the total energy loss of the bunch when traversing a cavity structure and q is the total charge of the bunch. Generally, the loss factor depends on the bunch length. It should be noted that the contribution of the accelerating mode (the fundamental loss) should be subtracted to predict the total power dissipation in the HOM loads. The prediction for the GBP HOM power dissipation was calculated from the loss factor computed for the grooved beam pipe structure only. The loss factors computed with MAFIA-T3 are collected in Table 5.1 and plotted in Fig. 5.15 as a function of the bunch length, together with those computed with ABCI [42] for a cylindrically symmetric cavity structure having circular beam pipes with an inside diameter of 150 mm. As seen from the Fig. 5.14, the theoretical prediction (solid curve) for the bunch length of 7 mm shows good agreement with the total HOM power dissipation data (closed circles), which is also consistent with the result of bunch length measurements [43].

Table 5.2: Loss factors computed with MAFIA-T3 and ABCI.

AC: the accelerating cavity. GBP: grooved beam pipe. CBP: circular beam pipe.

Bunch Length (mm)	MAFIA-T3 k (AC+2×GBP) (V/pC)	MAFIA-T3 k (2×GBP) (V/pC)	ABCI k (AC+2×CBP) (V/pC)
3			0.604
4		0.026	0.514
5			0.455
6			0.413
7	0.392	0.011	0.381
8			0.355
9			0.334
10	0.320	0.004	0.317

The results of the HOM power measurements for the 10 ARES cavities in the RF section D7 are summarized as follows:

- A significant cavity-to-cavity variation of the total HOM power dissipation was not observed.
- Almost all the HOM power induced in the accelerating cavity is dissipated in its WG and GBP HOM loads.
- The fraction of the beam-induced HOM power propagating through the circular beam pipe to the next cavity is small.

Focusing on the HOM-damped structure alone, the ARES cavities have functioned well without any troubles to stably support the high current electron and positron beams up to 940 mA in the HER and 1570 mA in the LER, respectively. No sign of coupled-bunch instabilities driven by HOMs of the ARES cavities has been observed so far.

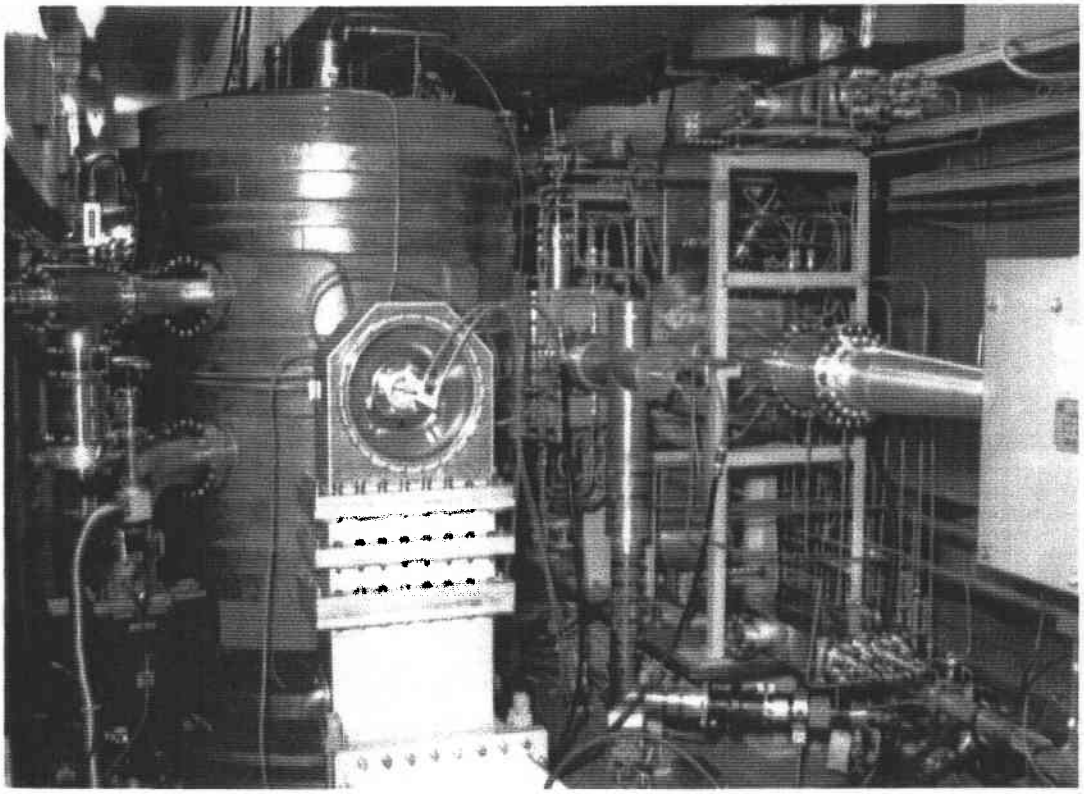

Figure 5.1. Conceptual Demonstrator ARES96 installed
in the TRISTAN Accumulation Ring (AR).

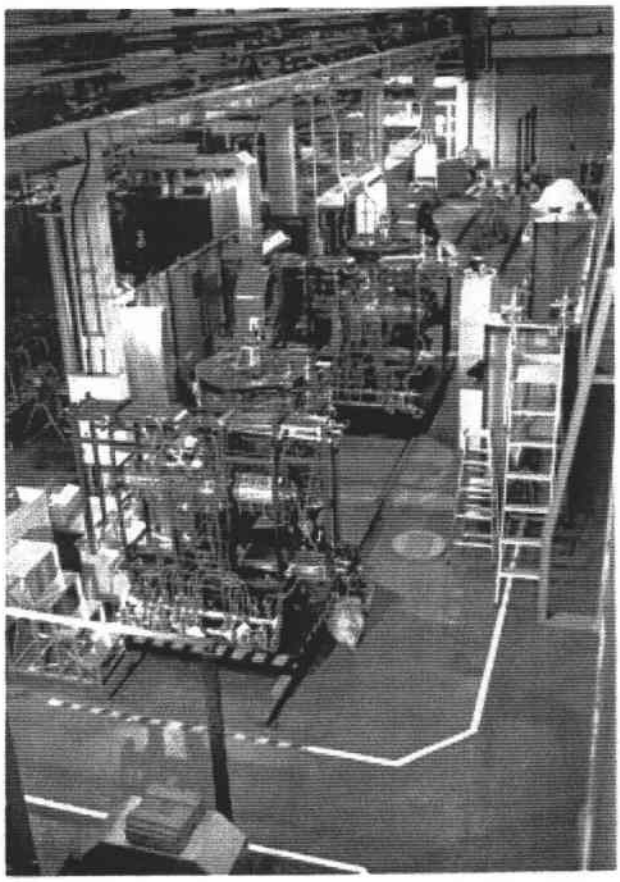

Figure 5.2. The assembly line for production cavities.

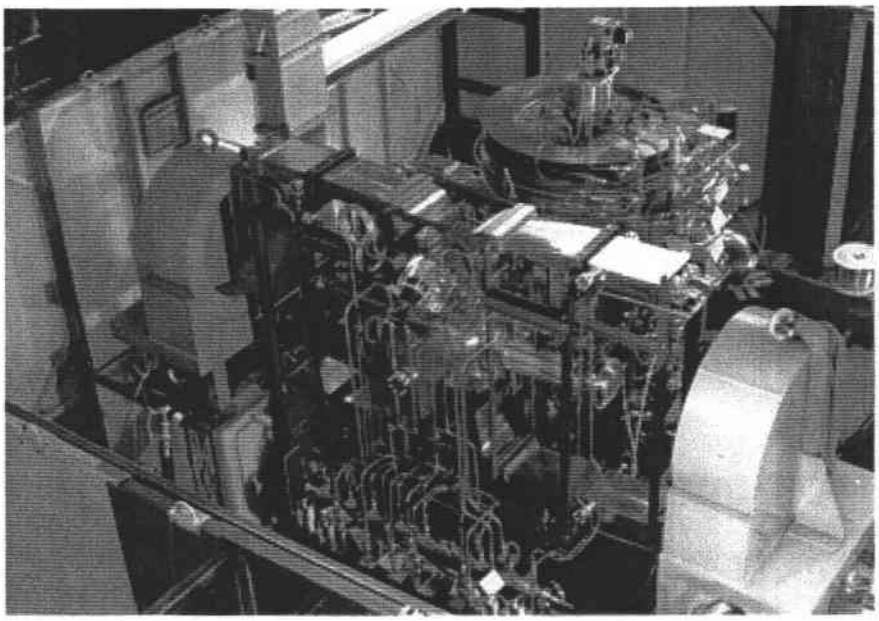

Figure 5.3. A close-up view of cavity teststand.

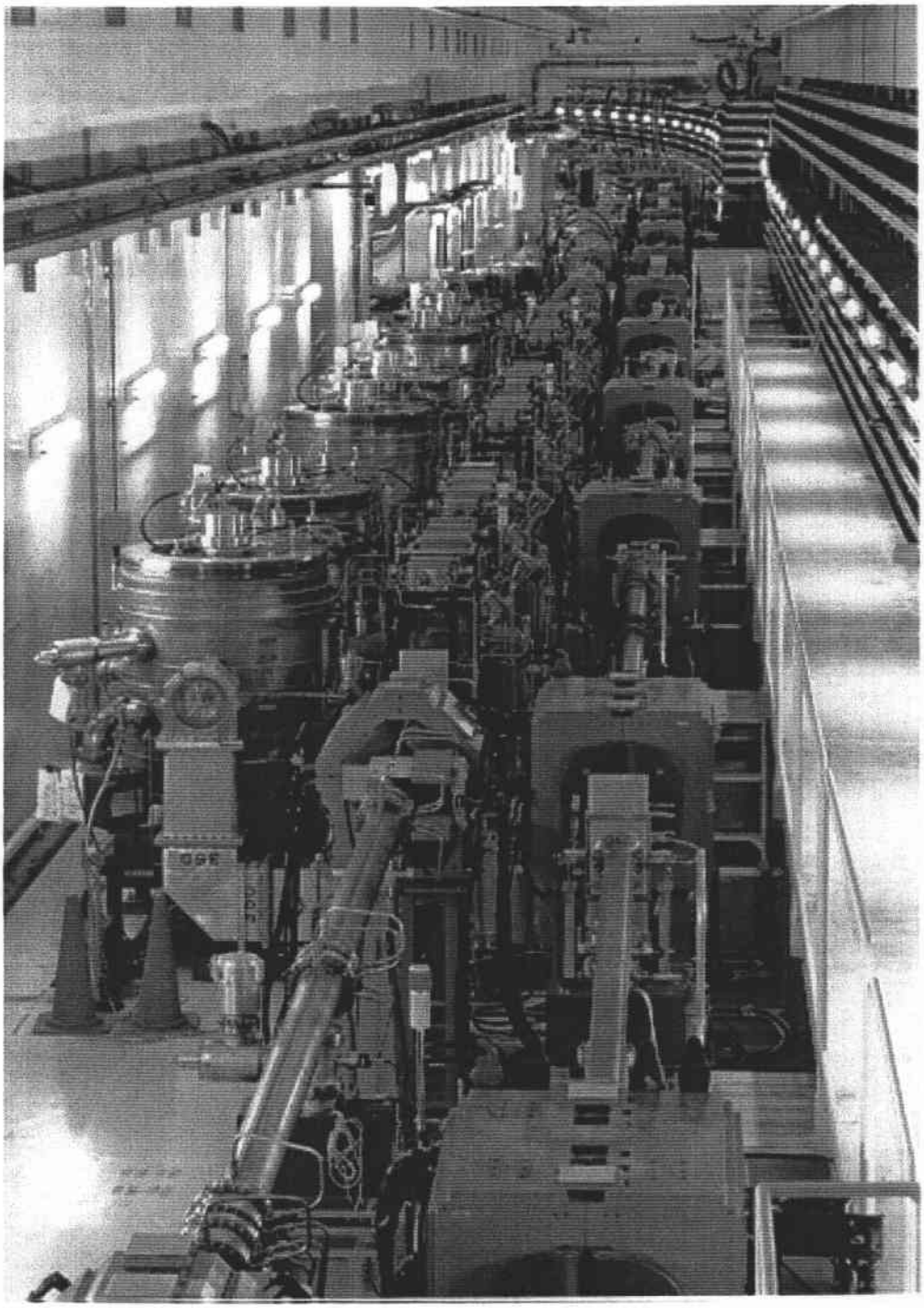

Figure 5.4. ARES cavities in the LER RF section D7.

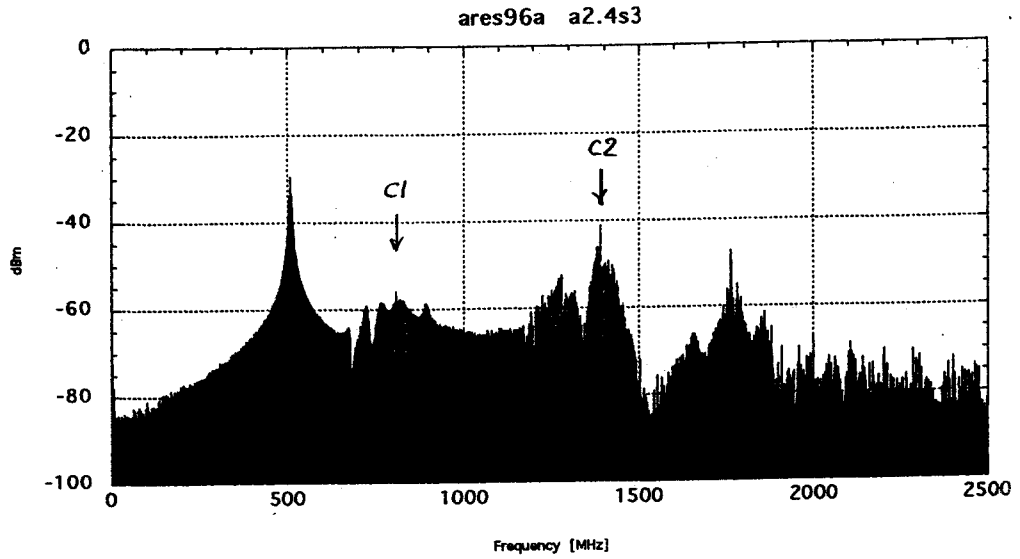

Figure 5.5. HOM spectrum excited by a single-bunch beam in the TRISTAN AR (AR), which was observed with a probe antenna at the accelerating cavity.

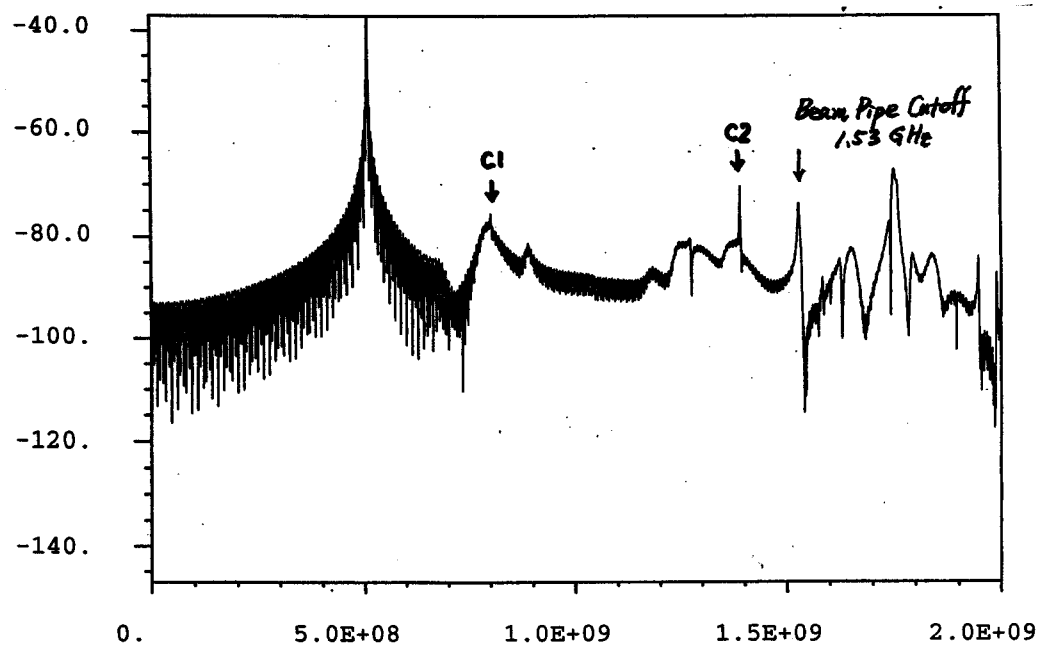

Figure 5.6. HOM spectrum computed with MAFIA-T3.

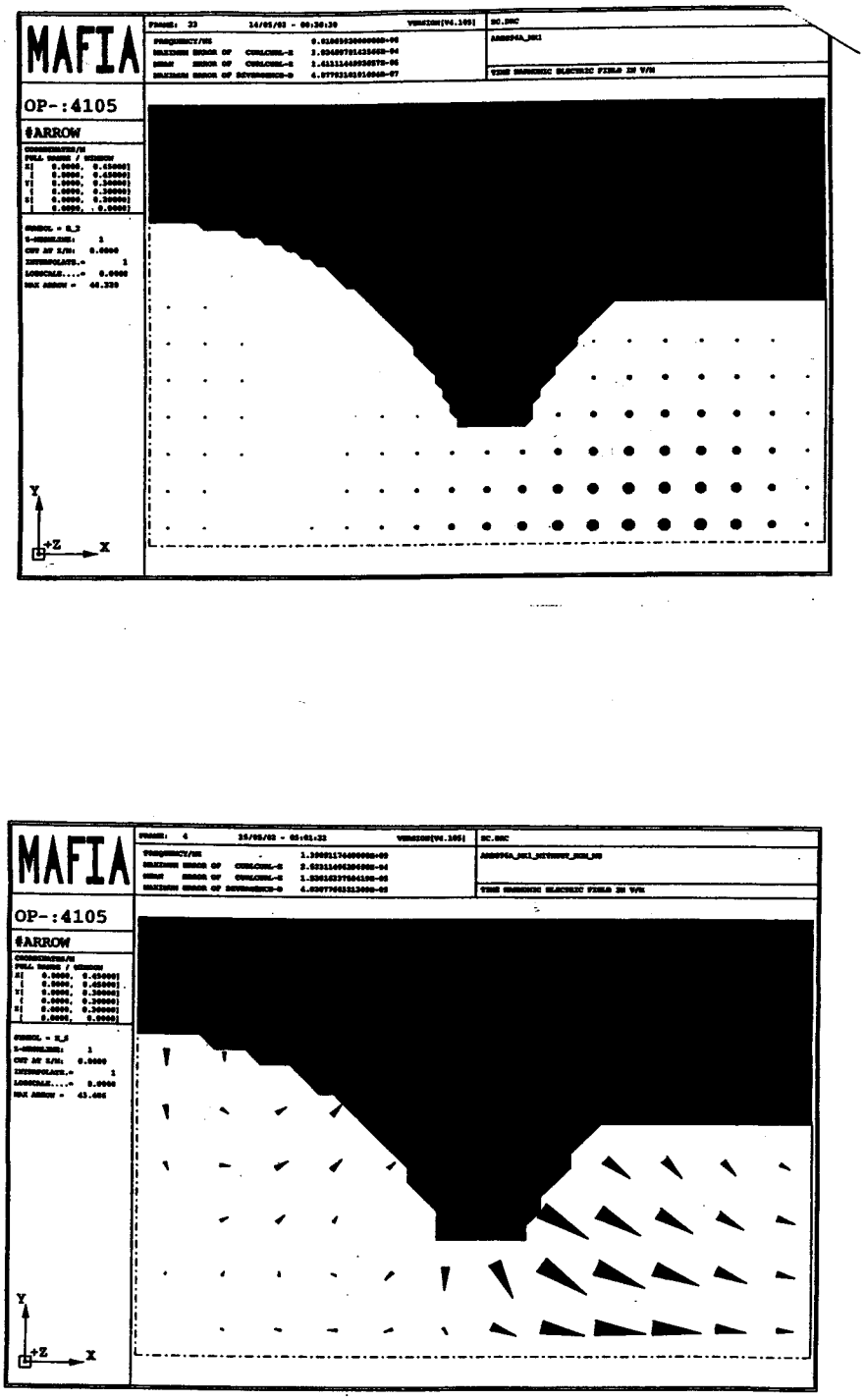

Figure 5.7. Electric field patterns computed with MAFIA for mode C1 (top) and mode C2 (bottom) trapped in the coupling cavity.

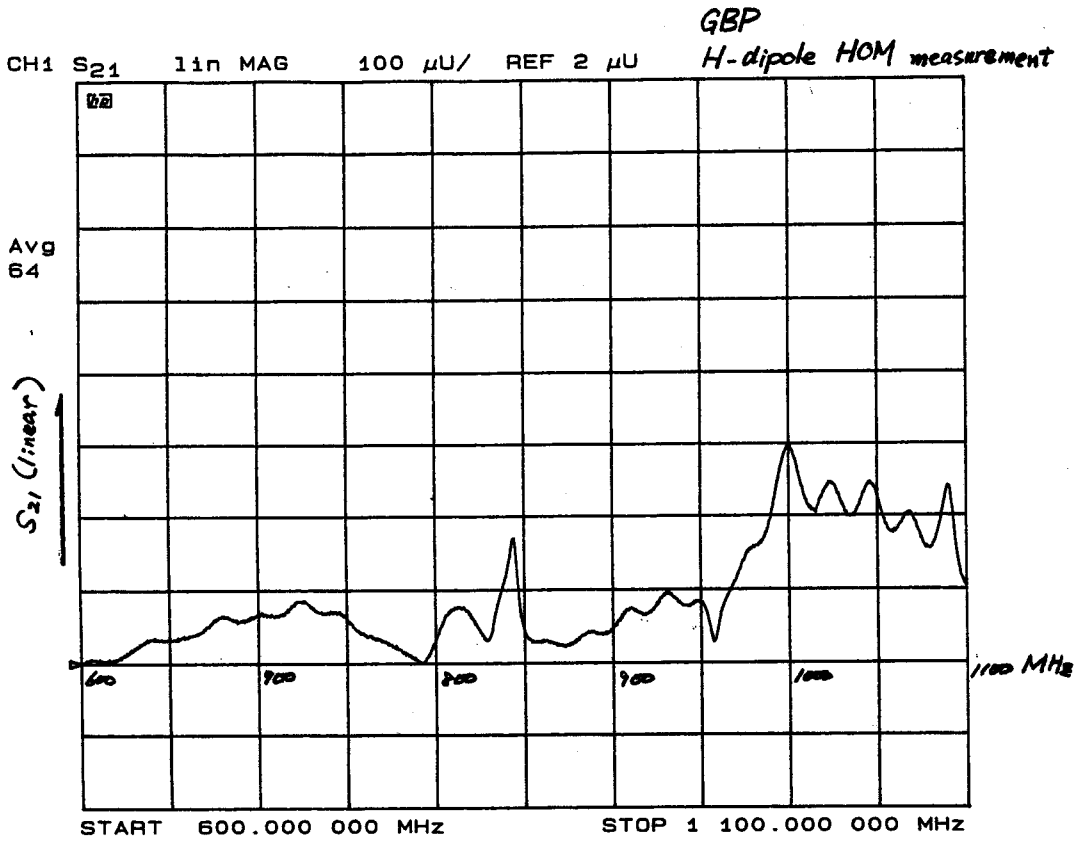

Figure 5.8. Spectrum obtained from low-power measurement of the H-dipole modes.

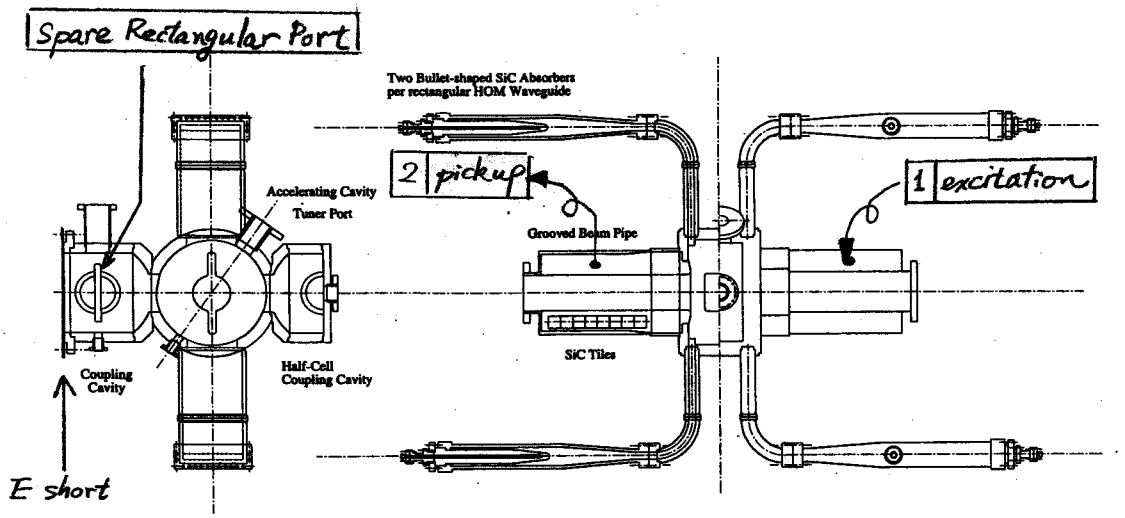

Figure 5.9. Set-up for low-power measurement of the H-dipole modes.

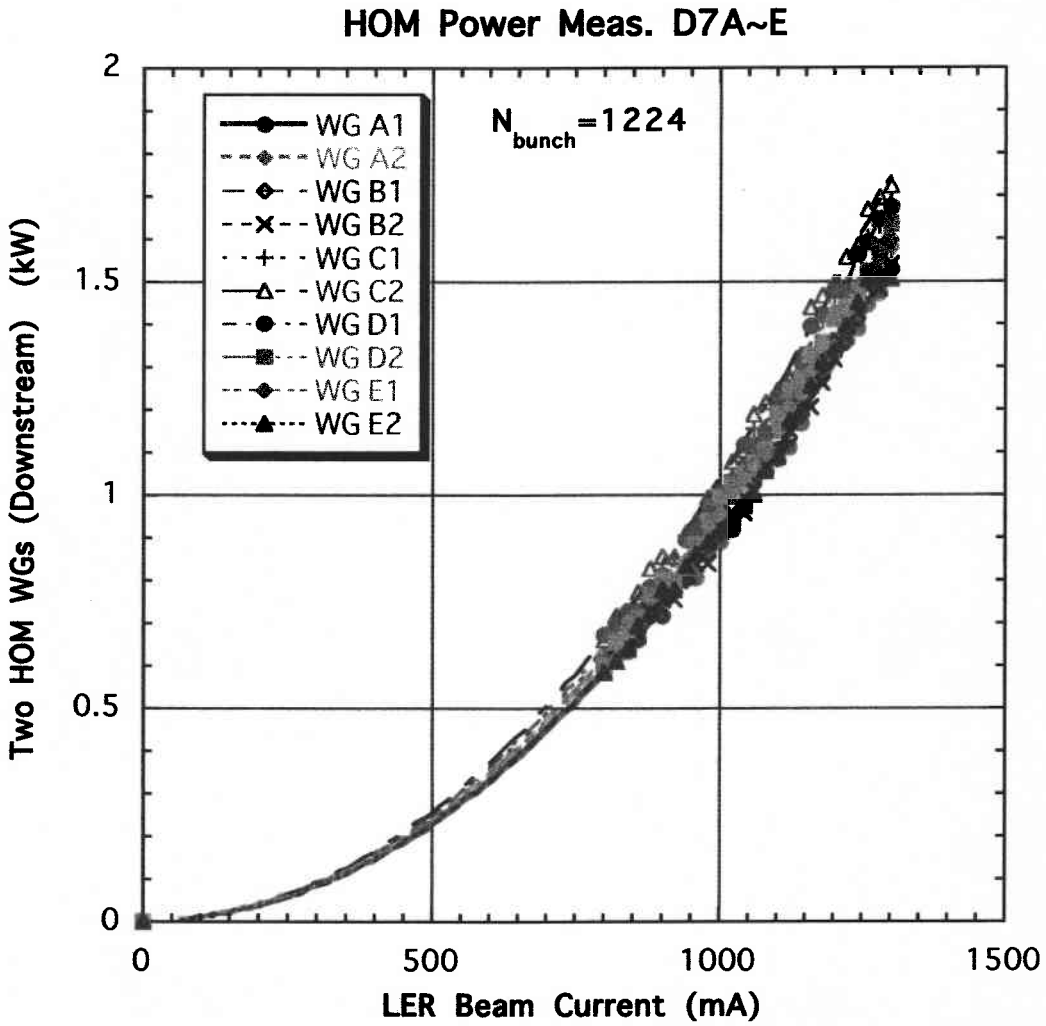

Figure 5.10. For every ARES cavity at the LER RF section D7, the HOM power dissipated in the four bullet-shape SiC absorbers of the two HOM waveguies at the downstream side is plotted as a function of the beam current.

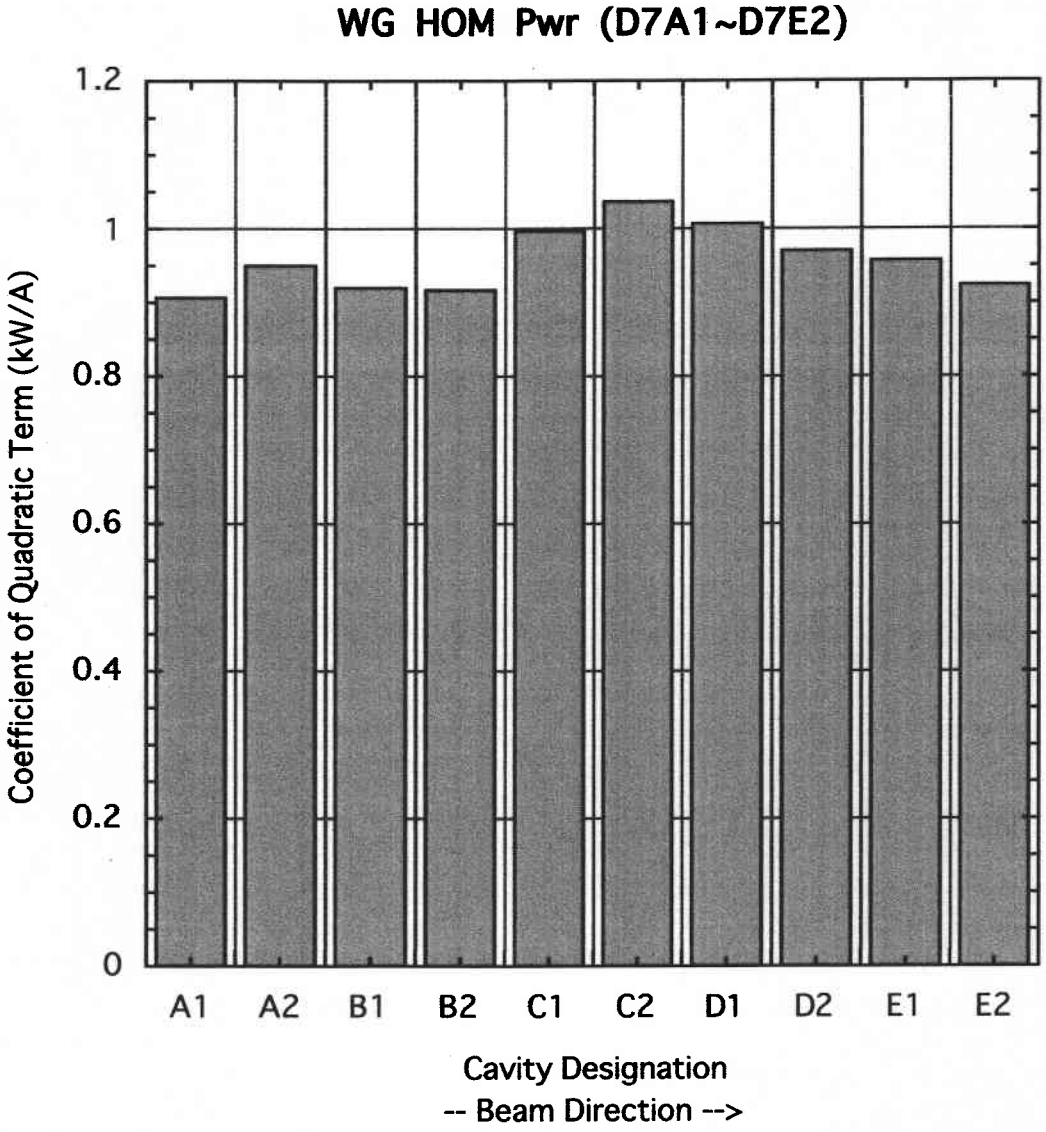

Figure 5.11. A bar graph showing the coefficient of the quadratic term of the beam current obtained from fitting the HOM power data for every cavity in Fig. 5.10.

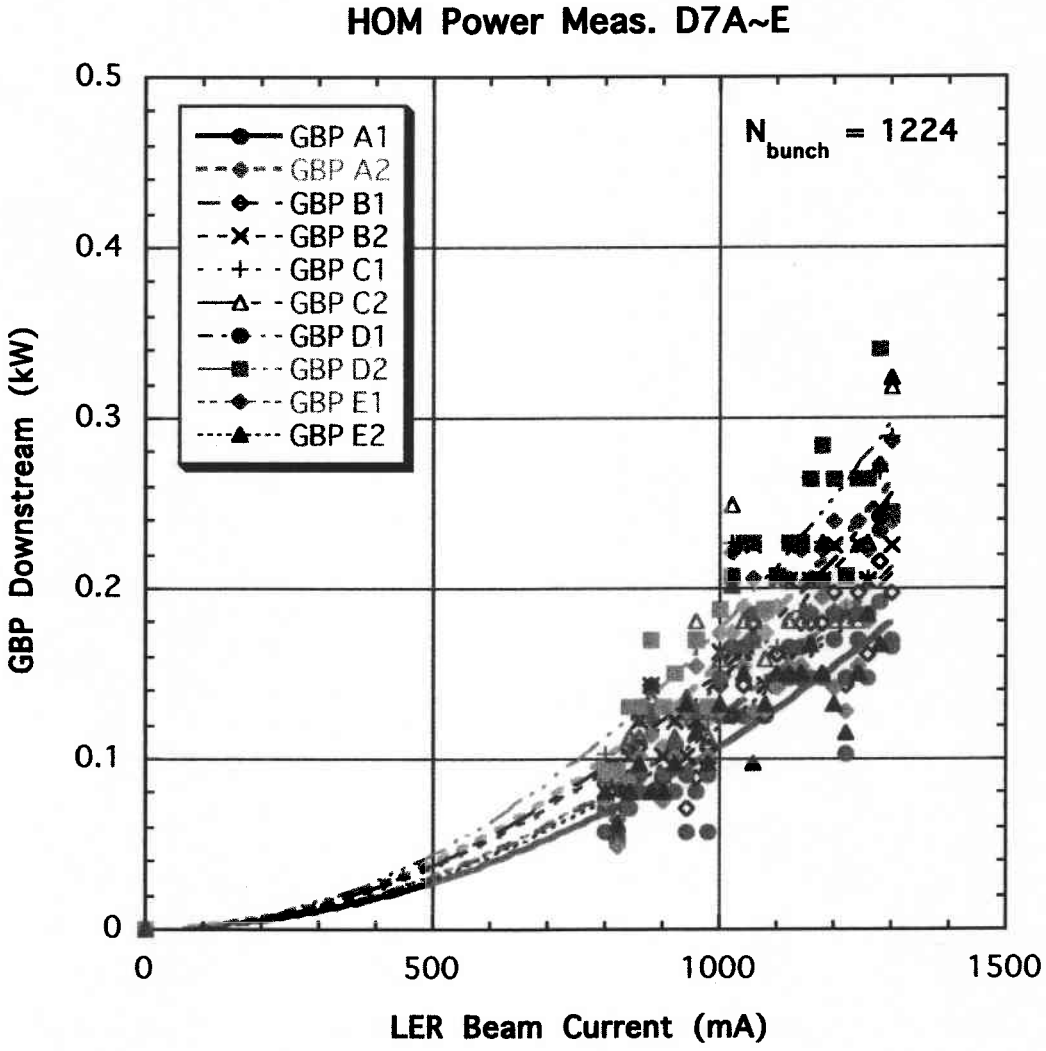

Figure 5.12. For every ARES cavity at the LER RF section D7, the HOM power dissipated at the SiC tiles in the grooved beam pipe at the downstream side is plotted as a function of the beam current.

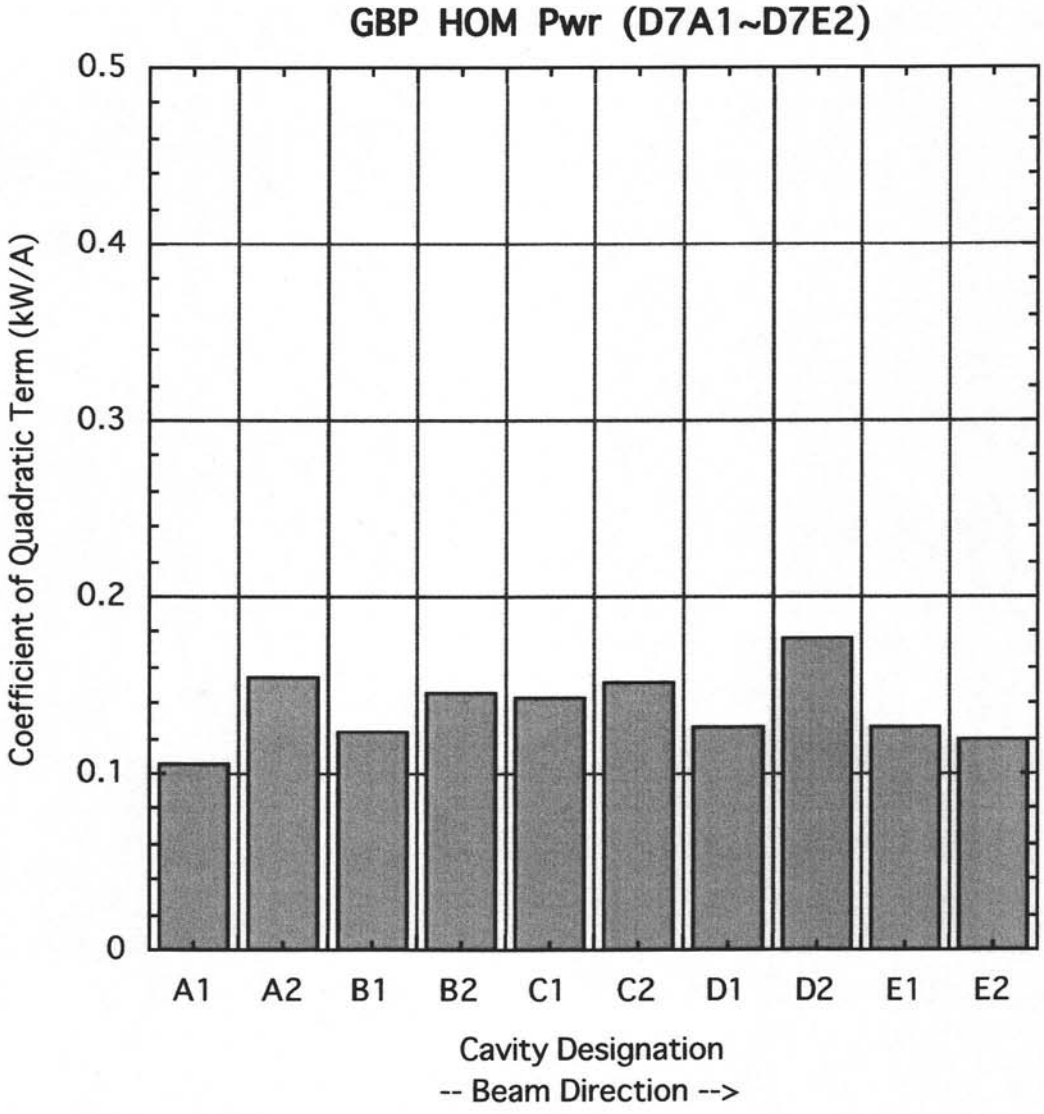

Figure 5.13. A bar graph showing the coefficient of the quadratic term of the beam current obtained from fitting the HOM power data for every cavity in Fig. 5.12.

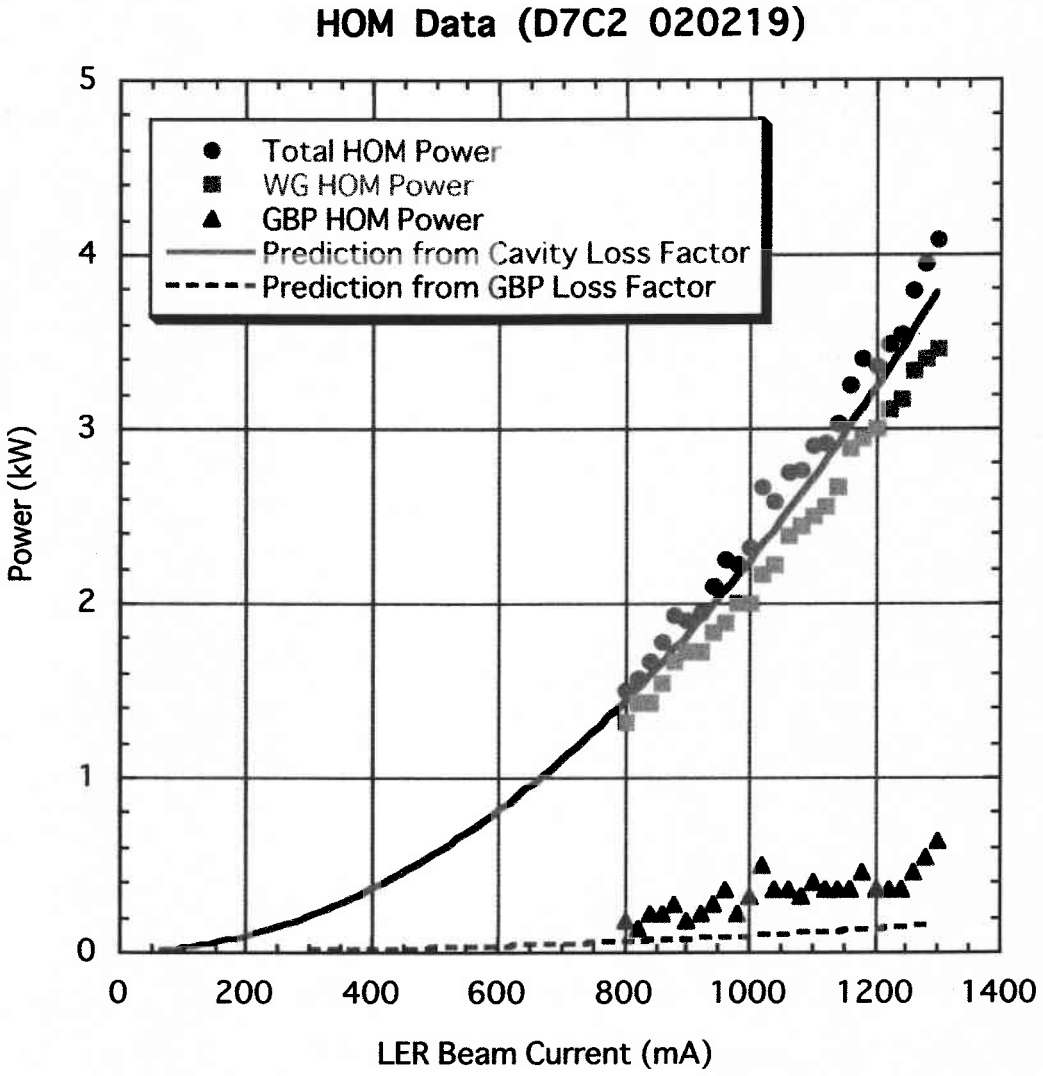

Figure 5.14. The WG and GBP HOM power dissipations for the AREC cavity C2 in the LER RF section D7 are plotted as a function of the beam current, together with the sum of these, that is, the total HOM power dissipation. The total HOM power dissipation and the GBP HOM power dissipation are compared with theoretical predictions shown by the solid and dashed curves, respectively.

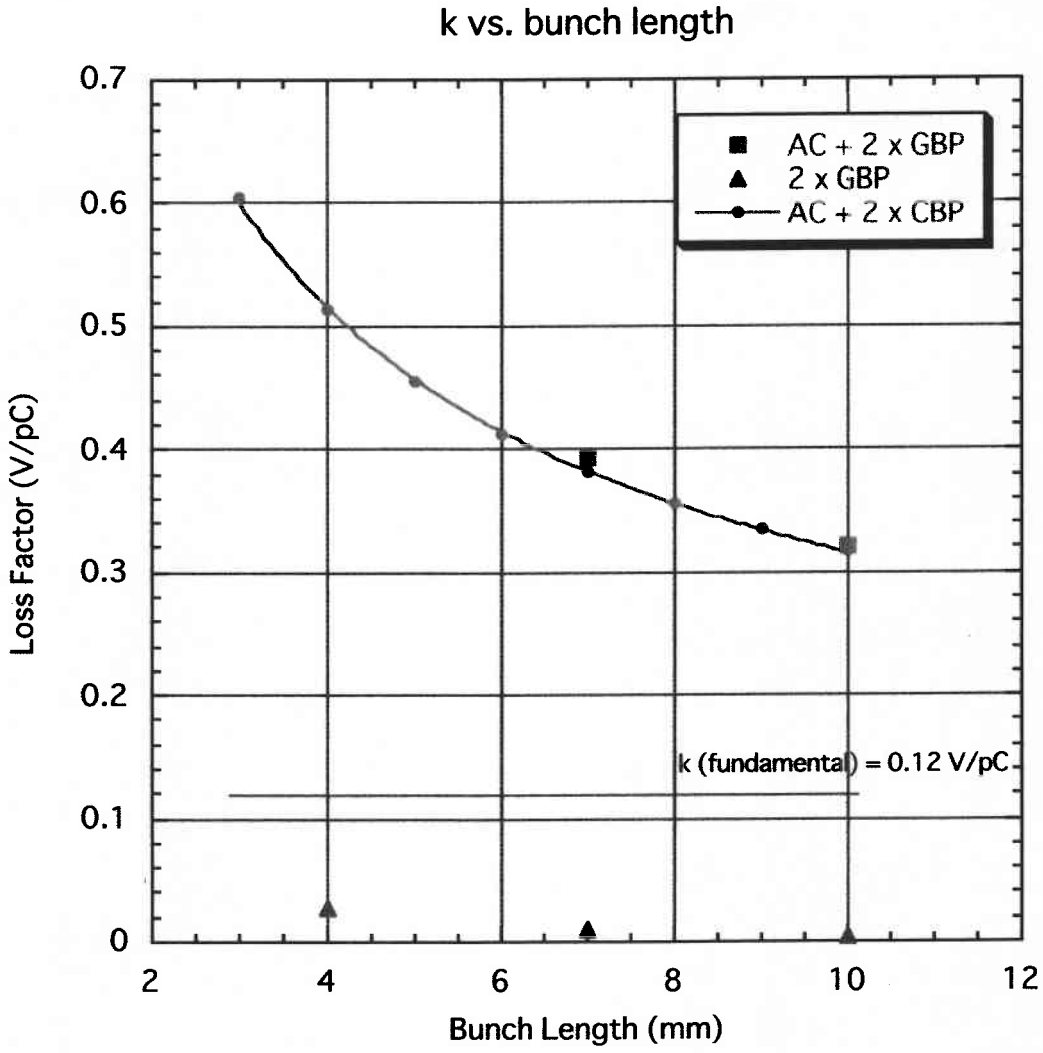

Figure 5.15. Loss factors computed with MAFIA-T3 and ABCI, are plotted as a function of bunch length.

AC + 2xGBP: accelerating cavity with two grooved beam pipes.

2 x GBP : two grooved beam pipes.

AC + 2xCBP: accelerating cavity with two circular beam pipes.

Chapter 6.
CONCLUSIONS

In this thesis, I have described a series of studies on Higher-Order-Mode (HOM) damping with grooved beam pipe structures: from the idea to selectively lower the cutoff frequency of the TE11 mode by grooving the inner wall of a circular beam pipe; through computer simulation studies on a pillbox cavity with grooved beam pipes, and benchmark experiments with a model cavity; finally to the development of the HOM-damped accelerating structure for the ARES cavity system operated in KEKB. The results are summarized as follows:

- In the case of a pillbox cavity with grooved beam pipes of fourfold symmetry, computer simulation studies and experiments with a model cavity have shown that the TM110 dipole mode can be heavily damped while the reduction in the shunt impedance of the accelerating mode is negligibly small.

- Slater's tuning curve theory of waveguide-loaded cavity system was also verified in self-consistent manner with two different set-ups using the same model cavity, one with a movable short-circuiting plunger and the other with an RF absorber.

- A HOM-damped accelerating structure with grooved beam pipe structure of twofold symmetry has been developed and applied to the ARES cavity for KEKB. The HOM damping properties were fully studied with use of time-domain simulation technique, and checked in beam-based and low-power experiments with the conceptual demonstrator ARES96.

- The fundamental-mode heating of the SiC tiles in the grooves, which arises from mixing of a dipole component into the fundamental mode caused by insertion of the tuning plunger into the accelerating cavity, was successfully suppressed by optimizing the grooved beam pipe structure including the inductive iris at the

entrance of the accelerating cavity.

- According to the HOM power measurements for the 10 ARES cavities in the RF section D7 for the LER:

  - A significant cavity-to-cavity variation of the total HOM power dissipation was not observed
  - A theoretical prediction, based on the loss factor computed for the accelerating cavity structure with the groove beam pipes in the case of a bunch length of 7 mm, shows good agreement with the total HOM power dissipation data, This result is also consistent with the result of bunch length measurements.
  - Almost all the HOM power induced in the accelerating cavity is dissipated in its WG and GBP HOM loads. The fraction propagating through the circular beam pipe to the next cavity is small.

Focusing on the HOM-damped structure alone, the ARES cavities have functioned well without any troubles to stably support the high current electron and positron beams up to 940 mA in the HER and 1570 mA in the LER, respectively. No sign of coupled-bunch instabilities driven by HOMs of the ARES cavities has been observed so far. Furthermore, the HOM loads currently have ample margins for high current operation. These facts make us confident of the performance and growth potential of the HOM-damped structure of the ARES cavity system toward the high-luminosity frontier beyond 10^{34} $cm^{-2}s^{-1}$ explored with the KEKB collider or its successor.

References

1. "KEKB B-Factory Design Report", KEK Report 95-7, August (1995).
2. "KEKB Accelerator Papers", compiled for publication in Nuclear Instruments and Methods Series A, KEK Preprint 2001-157, December (2001).
3. "PEP-II Conceptual Design Report", SLAC Report 418, LBL-PUB-5379, June (1993).
4. R. Boni et. al., "High Power Test of the Waveguide Loaded RF Cavity for the Frascati Φ-Factory Main Ring", Proceedings of European Particle Accelerator Conference (1996) p. 1979.
5. R. A. Rimmer et. al., "High-Power RF Cavity R&D for the PEP-II B Factory", Proceedings of European Particle Accelerator Conference (1994) p. 2101.
6. S. Sakanaka et. al., "Design of a HOM Damped Cavity for the ATF Damping Ring", Proceedings of Particle Accelerator Conference (1993) p. 1027.
7. T. Kageyama et. al., "Development of High-Power ARES Cavities", Proceedings of Particle Accelerator Conference (1997) p. 2902.
8. G. Conciauro and P. Arcioni, " A New HOM-Free Accelerating Resonator", Proceedings of European Particle Accelerator Conference (1990) p. 149.
9. K. Akai et. al., Proc. 15th Int. Conf. on High Energy Accel. 757 (1992).
10. T. Shintake, Jpn. J. Appl. Phys., **31** L1567 (1992).
11. T. Kageyama et. al., "Design of a Prototype of RF Cavity for the KEK B-Factory", Proceedings of European Particle Accelerator Conference (1994) p. 2098.
12. N. Akasaka et. al., "Quadrupole Counter Mixing Choke Structure for the KEKB ARES Cavity", Proceedings of European Particle Accelerator Conference (1996) p. 1997.
13. T. Weiland, "Single Mode Cavities", DESY 83-073 (1983).
14. T. Koseki, M. Izawa and Y. Kamiya, "Development of a Damped Cavity with SiC Beam-Duct", Proceedings of Particle Accelerator Conference (1995) p. 1794.
15. T. Furuya et. al., Proc. 7th SC-RF Workshop, CEA-Saclay, France (1995) p. 729.
16. T. Kageyama, "A Design of Beam Duct Cross Section for Damping Dipole Modes in RF Cavities", in Japanese Language, Proceedings of the 15th Linear Accelerator

Meeting in Japan (1990) p. 79, and KEK B-Factory Workshop, October (1990).

17. T. Kageyama, "Grooved Beam Pipe for Damping Dipole Modes in RF Cavities", Proceedings of the 8th Symposium on Accelerator Science and Technology (1991) p. 116.
18. H. Padamsee et. al., "Accelerating Cavity Development for the Cornell B-Factory, CESR-B", Proceedings of Particle Accelerator Conference (1991) p. 786.
19. T. Weiland, DESY 82-015, March (1982).
20. T. Weiland, DESY 83-005, February (1983).
21. The MAFIA Collaboration, CST GmbH, Darmstadt, Germany.
22. J.C. Slater, "Microwave Electronics", Van Nostrand (1950).
23. T. Kageyama, "A Simple Method using MAFIA to Calculate External Q Values of Waveguide-Loaded Cavities", KEK Report 89-4 (1989).
24. N.M. Kroll and D.U.L. Yu, "Computer Determination of the External Q and Resonant Frequency of Waveguide Loaded Cavities", Particle Accelerator, Vol.34, pp. 231-250 (1990).
25. Y. Funakoshi, Proceedings of the Mini-Workshop on KEK B-Factory, July (1991).
26. T. Shintake, "Proposals of RF Cavity coupled with an Energy Storage Cavity for Heavy Loading Accelerators", Particle Accelerators Vol. 44, pp. 131-145 (1994).
27. I. Wilson and H. Henke, "The LEP Main Ring Accelerating Structure", CERN 89-09 (1989).
28. Z.D. Farkas et. Al., " SLED: A Method of Doubling SLAC's Energy", Proceedings of the 9th International Conference on High Energy Accelerators, p. 576 (1976).
29. Y. Yamazaki and T. Kageyama, "A Three-Cavity System Which Suppresses the Coupled-Bunch Instability Associated with the Accelerating Mode", Particle Accelerators, Vol. 44, pp. 107-127 (1994).
30. K. Akai and Y. Yamazaki, "Three Dimensional Analysis of the Three-Cavity System for Heavily Beam-Loaded Accelerators", Particle Accelerators, Vol. 46, p. 197 (1994).
31. N. Akasaka et. al., "RF Characteristics of ARES Cold Models", Proceedings of Particle Accelerator Conference (1995) p. 1738.

32. T. Kageyama et. al., "The ARES Cavity for the KEK B-Factory", Proceedings of European Particle Accelerator Conference (1996) p. 2008.
33. N. Akasaka et. al., "Fundamental Mode Characteristics of ARES Cavity under Beam Environment", Proceedings of Particle Accelerator Conference (1997) p. 2974.
34. T. Kobayashi et. al., "HOM Characteristics of the ARES Cavity", Proceedings of Particle Accelerator Conference (1997) p. 3069.
35. F. Naito et. al., "The Input Coupler for the ARES Cavity", Proceedings of Asian Particle Accelerator Conference (1998) p776.
36. F. Naito et. al., "Coupling Cavity Damper for the ARES Cavity", Proceedings of Particle Accelerator Conference (1997) p. 2977.
37. Y. Takeuchi et. al., "HOM Absorber for the ARES Cavity", Proceedings of Particle Accelerator Conference (1997) p. 2986.
38. T. Weiland and R. Wanzenberg, "Wake Fields and Impedances", DESY M-91-06, May (1991).
39. T. Kageyama et. al. "The ARES Cavity for KEKB", Proceedings of the International Workshop on Performance Improvement of Electron-Positron Collier Particle Factories (1999) p. 49.
40. K. Akai et. al., "Commissioning of KEKB", KEKB Accelerator Papers compiled for publication in Nuclear Instruments and Methods Series A, KEK Preprint 2001-157, December (2001).
41. M. Izawa, T. Koseki, Y. Kamiya, and T. Toyomasu, Rev. Sci. Instrum. **66** p. 1910 (1995).
42. Y. Chin, "User's guide for ABCI Version 8.8", LBL-35258 and CERN SL/94-02 (1994).
43. M. Arinaga et. al., "KEKB Beam Instrumentation Systems", KEKB Accelerator Papers compiled for publication in Nuclear Instruments and Methods Series A, KEK Preprint 2001-157, December (2001).